The Astrophysical Journal, 890:51 (45pp), 2020 February 10 https://doi.org/10.3847/1538-4357/ab6458
© 2020. The American Astronomical Society. All rights reserved.

The Explosion of Helium Stars Evolved with Mass Loss

T. Ertl[1], S. E. Woosley[2], Tuguldur Sukhbold[3,4,5], and H.-T. Janka[1]
[1] Max-Planck-Institut für Astrophysik, Postfach 1317, D-85741 Garching, Germany
[2] Department of Astronomy and Astrophysics, University of California, Santa Cruz, CA 95064, USA
[3] Department of Astronomy, Ohio State University, Columbus, OH 43210, USA
[4] Center for Cosmology and AstroParticle Physics, Ohio State University, Columbus, OH 43210, USA
Received 2019 October 3; revised 2019 December 17; accepted 2019 December 17; published 2020 February 12

Abstract

Light curves, explosion energies, and remnant masses are calculated for a grid of supernovae resulting from massive helium stars that have been evolved including mass loss. These presupernova stars should approximate the results of binary evolution for stars in interacting systems that lose their envelopes close to the time of helium core ignition. Initial helium star masses are in the range 2.5–40 $M_\odot$, which corresponds to main-sequence masses of about 13–90 $M_\odot$. Common SNe Ib and Ic result from stars whose final masses are approximately 2.5–5.6 $M_\odot$. For heavier stars, a large fraction of collapses lead to black holes, though there is an island of explodability for presupernova masses near 10 $M_\odot$. The median neutron star mass in binaries is 1.35–1.38 $M_\odot$, and the median black hole mass is between 9 and 11 $M_\odot$. Even though black holes less massive than 5 $M_\odot$ are rare, they are predicted down to the maximum neutron star mass. There is no empty "gap," only a less populated mass range. For standard assumptions regarding the explosions and nucleosynthesis, the models predict light curves that are fainter than the brighter common SNe Ib and Ic. Even with a very liberal but physically plausible increase in ^{56}Ni production, the highest-energy models are fainter than $10^{42.6}$ erg s^{-1} at peak, and very few approach that limit. The median peak luminosity ranges from $10^{42.0}$ to $10^{42.3}$ erg s^{-1}. Possible alternatives to the standard neutrino-powered and radioactive-illuminated models are explored. Magnetars are a promising alternative. Several other unusual varieties of SNe I at both high and low mass are explored.

Unified Astronomy Thesaurus concepts: Core-collapse supernovae (304); Compact objects (288); Explosive nucleosynthesis (503); Light curves (918)

Supporting material: machine-readable table

1. Introduction

A large fraction, perhaps half or more, of all stars massive enough to experience iron core collapse also interact with a close binary companion at some time during their lives (Sana & Evans 2011; Sana et al. 2012). This interaction alters their evolution and the sorts of supernovae and remnants they produce (Podsiadlowski 1992; Wellstein & Langer 1999; Langer 2012; De Marco & Izzard 2017). The effect on the birth function for compact remnants is particularly important because the most accurate stellar mass determinations come from stars in relatively close binary systems.

A common outcome for strongly interacting binaries is for one or both stars to lose most of their hydrogen envelopes when they first become red supergiants. Continued mass loss by binary interaction and winds then removes any residual hydrogen and a portion of the helium (He) and carbon–oxygen (CO) core as well. As a result, when the star dies, its presupernova mass is smaller than the He core mass would have been had the star evolved in isolation. Its composition also differs, and the braking of the rotation of the exploding core by a low-density hydrogen envelope does not occur. Mixing and fallback are altered, and of course, if all of the hydrogen is lost, the supernova is Type I, not Type II.

Many studies of binary evolution have been and are being carried out, spurred on most recently by the burgeoning field of gravitational wave astronomy. The actual outcome from any given binary depends upon its initial masses, orbital separation, and intricacies of mass loss and transfer, especially if a common envelope forms. Population synthesis and a large number of models are required to explore the broad range of possibilities realistically. Here, however, we continue to adopt a gross simplification to binary evolution (see also Woosley 2019). It is assumed that the consequence of binary interaction is to promptly remove the entire hydrogen envelope of the star at helium ignition. This surely does not happen all the time. Some SNe IIb still have hydrogen despite experiencing a binary interaction, though that hydrogen mass is generally small. Some stars do not become red giants at the beginning of helium burning, but rather later on, and the evolution of the secondary will be different from that of the primary. Changing the metallicity will alter the radii of the stars, the binding energies of their envelopes, and their mass transfer history.

Nevertheless, this assumption allows us to explore some of the major consequences of binary evolution using a simple, minimally parameterized grid of models. The price paid is that the connection between a given helium star mass and its main-sequence mass is imprecise. The mass loss during helium burning may also be distorted, since the core may actually have burned some helium before losing its last hydrogen. On the other hand, mass-loss rates for helium stars are uncertain, and for the time being, that uncertainty dominates the outcome.

Our main purpose is to explore the different sorts of outcomes that might occur in binaries with a large range of masses. What distribution of black hole and neutron star remnant masses do they produce? What are their explosion energies, and how much ^{56}Ni do they make? What do their supernovae look like? These questions were answered for

[5] NASA Hubble Fellow.

nonrotating single stars of solar metallicity by Sukhbold et al. (2016). Here we determine the first-order corrections to that study for the effects of binary membership.

An important related goal is understanding the origin of SNe Ib and Ic. It is thought that most of these are derived from stripped stars in binaries (Langer 2012; Branch & Wheeler 2017). Here the appropriate mass range and energies are determined assuming that the supernovae result exclusively from neutrino heating and the light curves are powered by radioactivity. Perhaps surprisingly, for current observational statistics, this simple prescription can explain only about half of the common events. Inadequate ^{56}Ni is produced to explain the brighter half. This leads us to conclude that some other energy source could be frequently powering, or at least illuminating, these brighter events. The intriguing possibility of heating common SNe Ib and Ic using a newly formed magnetar is explored.

Other mass ranges, both smaller and larger than inferred for common Type Ib and Ic events, give rise to different sorts of events that may or may not have been detected yet. The lighter stars experience radius expansion and have bright initial peaks from envelope recombination or circumstellar interaction. The heavier ones produce faint, red supernovae with broad light-curve peaks that may have escaped discovery. In the magnetar paradigm, these big stars could also occasionally be super-luminous supernovae, broad-line SNe Ic, or even gamma-ray bursters.

In Section 2, the progenitor stars used in the study are discussed. They are taken from the recent survey of Woosley (2019). In Section 3, we discuss the simulation of the explosions using the one-dimensional (1D) neutrino-transport code Prometheus-Hot Bubble (P-HOTB), postprocessed using *KEPLER* to get the details of nucleosynthesis and calculate light curves. This is the same approach used by Sukhbold et al. (2016) to survey the evolution of single stars, but there have been some substantial changes to P-HOTB and the way ^{56}Ni yields are calculated. These revisions are discussed in Section 3 and Appendix A. Section 4 gives our general results and discusses their dependence on the choice of a model for the central engine. Section 5 discusses the nucleosynthesis of iron, oxygen, and magnesium. Observations limit the amount of iron that core-collapse supernovae can eject relative to oxygen and magnesium and that, in turn, limits the radioactive contribution to the light curve. Section 6 summarizes our results for the birth functions for neutron stars and black holes. Sections 7 and 8 give our results for light curves and their dependence on assumed physics, especially the evaluation of the ^{56}Ni yield. As previously mentioned, it proves difficult to obtain the full brightness for some of the SNe Ib and Ic in the literature using just the yields from the neutrino-driven explosion models, and possible alternatives are discussed. In Section 9, we summarize our findings and discuss their consequences.

2. Presupernova Models

All presupernova models were calculated using the *KEPLER* code (Weaver et al. 1978), the physics of which has been extensively discussed in the literature (e.g., Woosley et al. 2002; Woosley & Heger 2007, 2015; Sukhbold & Woosley 2014; Sukhbold et al. 2018). All stars were nonrotating and had solar metallicity ($Z = 0.0145$, with a total mass fraction of iron-group species $X_{\rm Fe} = 1.46 \times 10^{-3}$). Models were defined by their initial mass, $M_{\rm He,i}$, which was composed mostly of helium. In the paper, models that used the standard mass-loss rate will often be referred to by the name "Hexx," where "xx" is $M_{\rm He,i}$. The lower bound to the survey, 2.5 $M_\odot$, was set by the lightest star to experience iron core collapse in the *KEPLER* code (Woosley 2019). The evolution of still lighter stars, 1.6–2.5 $M_\odot$, evolved by Woosley was not studied here because none were successfully evolved to iron core collapse. Most will become CO or neon–oxygen white dwarfs. Some uncertain fraction may evolve to electron-capture supernovae and contribute to the supernova rate and remnant distribution, but they are not included in the analysis or statistics presented here.

Table 1 and Figure 1 summarize the models that were studied. Here $M_{\rm He,i}$ and $M_{\rm preSN}$ are the masses of the initial helium star and the presupernova mass, the difference being mass loss as a Wolf–Rayet (WR) star. The initial composition was taken to be the ashes of hydrogen burning in a massive star of solar metallicity. For details and formulae relating $M_{\rm He,i}$ to the zero-age main-sequence (ZAMS) mass, see Woosley (2019). The mass-loss rate employed was that of Yoon (2017), which specifies different parameters for WNE and WC/WO stars. For comparison, a smaller grid of models was computed that used 1.5 times that mass-loss rate. Results for those models are given at the end of the table. While the focus in this paper is on stars calculated using the "standard" rate, models with enhanced mass loss gave very similar presupernova stars when adjusted to the same final presupernova mass. They may have the advantage of producing a larger fraction of SNe Ic, since the CO core is more frequently uncovered.

Here $M_{\rm CO}$ and $M_{\rm Fe}$ give the CO and iron core masses for the presupernova star. The CO core mass is where the helium mass fraction falls below 0.01 moving inward in the star. The iron core mass is where the mass fraction of iron exceeds 0.5 moving inward in the star. The CO core masses are larger for a given presupernova mass than for single stars due to the removal of helium by WR winds during helium burning. This and the larger carbon mass fraction following helium burning result in the presupernova stars having more compact structures, i.e., smaller compactness parameters, than their single-star counterparts (Woosley 2019).

Also given are the luminosity and effective temperature of the presupernova star. These quantities are evaluated at oxygen ignition to avoid complications introduced by the silicon flash in lower-mass ($M \leqslant 3.2\,M_\odot$) models. Here $Y_{\rm s}$ is the helium mass fraction at the surface of the presupernova star. Values less than 0.9 show the loss of the entire helium shell and may be relevant for making an SN Ic instead of an SN Ib.

Explosions for helium stars smaller than 40 $M_\odot$ were calculated using both *KEPLER* and P-HOTB (Section 3). More massive stars would not have exploded using the present prescription for neutrino-energy deposition following iron core collapse. Their remnant masses are included in the statistics assuming full collapse of the presupernova star, and nucleosynthesis ejected in the winds of these "failures" is also included in computing the averages (Section 5). For the standard mass-loss rate, helium stars above 70 $M_\odot$ produce presupernova stars over 35 $M_\odot$ at oxygen ignition and experience a violent pulsational pair instability that modifies their final mass. The final collapse of the iron core was not modeled here, but it is assumed that no outgoing shock will be launched. The pulsations were also not studied here (though see Woosley 2019). When computing remnant mass averages, it is assumed that no black hole over 46 $M_\odot$ was formed.

Table 1
Properties of Progenitor Models (Subset)

$M_{\rm He,i}$ ($M_\odot$)	$M_{\rm preSN}$ ($M_\odot$)	$M_{\rm ZAMS}$ ($M_\odot$)	$M_{\rm CO}$ ($M_\odot$)	$M_{\rm Fe}$ ($M_\odot$)	log $L_{\rm preSN}$ (erg s^{-1})	log $T_{\rm eff}$ (K)	$Y_{\rm s}$
			Si Flash				
2.5	2.10	13.5	1.37	1.29	4.37	4.73	0.99
3.0	2.45	15.1	1.61	1.32	4.61	3.99	0.99
3.1	2.52	15.5	1.66	1.34	4.63	4.16	0.99
3.2	2.59	15.8	1.70	1.37	4.65	4.34	0.99
			Inflated Envelope				
2.6	2.15	13.9	1.41	1.30	4.37	3.85	0.99
2.7	2.22	14.2	1.46	1.29	4.51	3.87	0.99
2.8	2.30	14.5	1.51	1.31	4.55	3.89	0.99
2.9	2.37	14.8	1.56	1.34	4.59	3.92	0.99
			Standard $\dot{M}$				
3.3	2.67	16.1	1.75	1.33	4.66	4.29	0.99
3.4	2.74	16.4	1.80	1.35	4.68	4.29	0.99
3.5	2.81	16.7	1.85	1.36	4.69	4.55	0.99
3.6	2.88	17.0	1.90	1.34	4.72	4.58	0.99
3.7	2.95	17.3	1.96	1.35	4.74	4.62	0.99
3.8	3.02	17.5	2.01	1.37	4.75	4.65	0.99
3.9	3.09	17.8	2.07	1.37	4.77	4.67	0.99
4.0	3.15	18.1	2.12	1.38	4.78	4.69	0.99
4.1	3.22	18.4	2.17	1.43	4.80	4.70	0.99
4.2	3.29	18.7	2.22	1.39	4.81	4.72	0.99
4.3	3.36	19.0	2.27	1.39	4.83	4.73	0.99
4.4	3.42	19.2	2.33	1.40	4.85	4.74	0.99
4.5	3.49	19.5	2.38	1.47	4.85	4.75	0.99
5.0	3.82	20.8	2.65	1.55	4.91	4.86	0.99
5.5	4.14	22.1	2.90	1.57	4.96	4.92	0.99
6.0	4.45	23.3	3.15	1.52	5.02	4.95	0.99
6.5	4.75	24.5	3.39	1.61	5.06	4.97	0.99
7.0	5.05	25.7	3.63	1.50	5.10	4.99	0.99
7.5	5.35	26.8	3.87	1.48	5.13	5.00	0.99
8.0	5.64	27.9	4.11	1.41	5.17	5.00	0.99
9.0	6.20	29.7	4.59	1.45	5.21	5.01	0.99
10	6.75	31.7	5.07	1.44	5.27	5.02	0.99
11	7.05	33.7	5.45	1.63	5.27	5.24	0.64
12	7.27	35.7	5.55	1.61	5.28	5.22	0.38
14	8.04	39.7	6.11	1.68	5.36	5.24	0.19
16	8.84	43.7	6.79	1.69	5.39	5.25	0.22
18	9.62	47.7	7.42	1.41	5.42	5.25	0.23
20	10.4	51.7	8.01	1.43	5.47	5.30	0.25
24	12.1	59.7	9.40	1.60	5.58	5.34	0.22
28	13.9	67.7	10.9	1.81	5.68	5.36	0.21
32	15.7	75.7	12.4	1.95	5.76	5.37	0.20
36	17.6	83.7	14.0	1.96	5.83	5.39	0.20
40	19.6	91.7	15.7	2.27	5.89	5.40	0.19
			1.5 × $\dot{M}$				
5.0	3.43	20.8	2.37	1.44	4.85	4.89	0.99
6.0	3.96	23.3	2.77	1.61	4.95	4.98	0.99
7.0	4.45	25.7	3.17	1.51	5.03	5.05	0.99
8.0	4.92	27.9	3.56	1.54	5.09	5.09	0.98
10	4.96	31.7	3.73	1.58	5.08	5.06	0.22
12	5.43	35.7	4.04	1.44	5.12	5.07	0.21
14	5.86	39.7	4.40	1.44	5.18	5.15	0.22
16	6.34	43.7	4.79	1.43	5.20	5.15	0.21
18	6.84	47.7	5.19	1.53	5.26	5.16	0.20
20	7.39	51.7	5.62	1.48	5.29	5.17	0.19
24	8.54	59.7	6.55	1.69	5.37	5.18	0.18
28	9.77	67.7	7.50	1.41	5.43	5.19	0.17
32	11.1	75.7	8.55	1.50	5.53	5.18	0.16
36	12.4	83.7	9.60	1.64	5.60	5.18	0.16

Note. The quantities are evaluated at oxygen ignition, and $Y_{\rm s}$ is the helium mass fraction at the surface of the presupernova star.

(This table is available in its entirety in machine-readable form.)

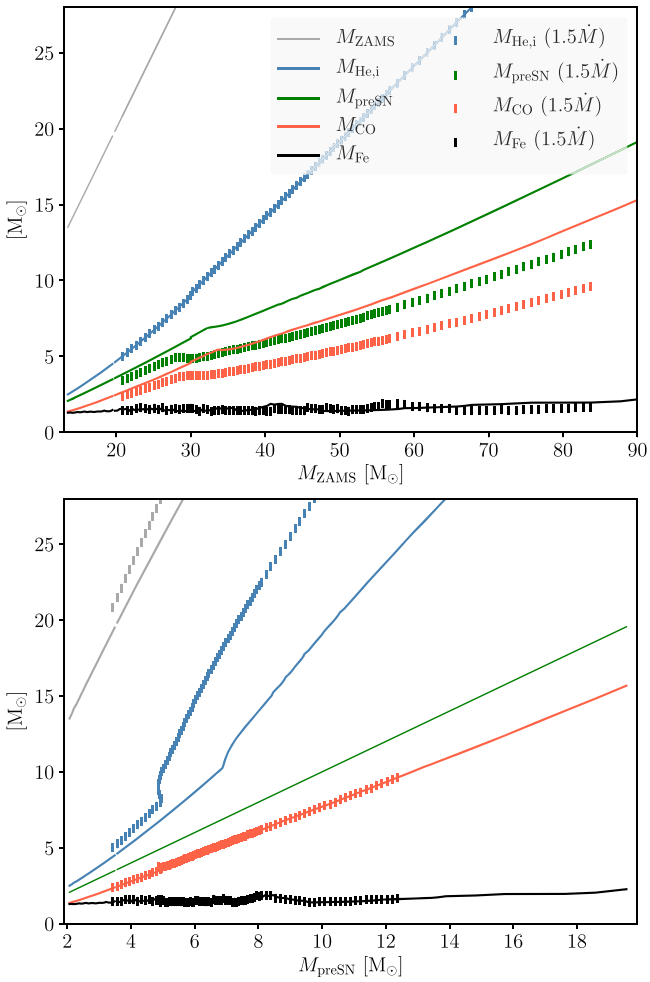

Figure 1. Top: initial helium star mass ($M_{\rm He,i}$), presupernova mass ($M_{\rm preSN}$), CO core mass ($M_{\rm CO}$), and iron core mass ($M_{\rm Fe}$) given as a function of the estimated initial main-sequence mass of the star just before its envelope is lost. Vertical hatching shows models that used 1.5 times the standard mass-loss rate. Bottom: same core masses as a function of the final (presupernova) mass of the star.

3. Explosion Modeling

As in Sukhbold et al. (2016), explosions were calculated using two different 1D hydrodynamics codes, P-HOTB (Janka & Müller 1996; Kifonidis et al. 2003) and *KEPLER* (Weaver et al. 1978; Woosley et al. 2002). There were few changes in the *KEPLER* postprocessing, except for the introduction of an alternate way of evaluating iron-group yields using a deeper mass cut more consistent with P-HOTB. The changes in P-HOTB were extensive and are discussed both here and in Appendix A.

3.1. Modeling with P-HOTB

The code P-HOTB is a 1D, 2D, or 3D neutrino-hydrodynamics code for simulating the explosion of supernovae. The original version was derived from the PROMETHEUS hydrodynamics code (Fryxell et al. 1989, 1991; Müller et al. 1991). It was first developed and employed in 1D and 2D simulations by Janka & Müller (1996) but later upgraded to include more microphysics and a more generalized numerical grid (e.g., Kifonidis et al. 2003; Scheck et al. 2006; Arcones et al. 2007;

Ugliano et al. 2012; Ertl et al. 2016a). Since 2010, P-HOTB has also been applied to 3D supernova simulations by Hammer et al. (2010) and—supplemented for an axis-free Yin-Yang grid—by Wongwathanarat et al. (2010a, 2010b, 2013, 2015, 2017) and Gessner & Janka (2018).

The code P-HOTB is optimized to efficiently simulate neutrino-driven supernovae continuously from the onset of stellar core collapse, through core bounce and the onset of explosion, and onto the late stages of the ejecta expansion. In order to cover this large range of spatial and temporal scales for large sets of models, the treatment of the problem and the relevant microphysics is approximated in many aspects, but efforts are made to preserve the essential physics of the neutrino-driven mechanism.

The chief characteristics of P-HOTB are its use of an approximate, gray treatment of neutrino transport in the outer layers (optical depths below about $\mathcal{O}(1000)$) of the newborn neutron star and the replacement of the central, high-density core of the neutron star by an inner grid boundary that shrinks with time. The movement of the grid boundary mimics the contraction of the cooling and deleptonizing compact remnant. Excising the core of the neutron star allows larger time steps, facilitating the efficient long-time simulation of the explosion including the central neutrino source. It also permits a choice of neutrino luminosities and mean spectral energies as inner boundary conditions that enable neutrino-driven explosions to be calculated with a chosen energy in spherical symmetry or higher dimensions. The replacement of the inner core of the nascent neutron star is justified by the fact that the high-density nuclear equation of state (EOS) remains uncertain despite considerable theoretical and experimental progress (see, e.g., Schneider et al. 2019).

At the onset of a calculation, the rest-mass density ρ, radial fluid velocity v, electron fraction Y_e, nuclear composition (in regions where nuclear statistical equilibrium (NSE) does not apply), and pressure P as functions of radius from the progenitor data are mapped onto the computational grid of P-HOTB. Using the pressure guarantees that hydrostatic equilibrium in the progenitor star and the developing core contraction at the onset of core collapse are well represented. The period from core collapse until core bounce is treated using the deleptonization scheme of Liebendörfer (2005), the $Y_e(\rho)$ trajectory of Figure 1 in Ertl et al. (2016a), and the nuclear EOS of Lattimer & Swesty (1991) with an incompressibility modulus of 220 MeV. After core bounce, neutrinos and antineutrinos of all flavors are followed with the gray transport approximation.

About 10 ms after bounce (specifically, at the time the shock encloses 1.25 $M_\odot$), the central high-density core of the proto–neutron star (PNS) with a mass of 1.1 $M_\odot$ is excluded from the computational domain and replaced by a gravitating point mass. The gravitational force of this point mass and the self-gravity of the matter on the grid are corrected for general relativistic effects (see Arcones et al. 2007). For the hydrodynamics, the inner grid boundary corresponds to a Lagrangian mass coordinate at which the boundary conditions of the hydrodynamic variables ensure hydrostatic equilibrium. As long as the evolution of the PNS is tracked, the simulations of the present paper follow Arcones et al. (2007), Ugliano et al. (2012), Ertl et al. (2016a), and Sukhbold et al. (2016) in the contraction of the inner grid boundary and the boundary conditions for the neutrino properties at this location. The inner grid boundary, and with it the whole computational grid, is moved according to an exponential interpolation between initial radius $R_{\rm ib,i}$ and defined final radius $R_{\rm ib,f}$: $R_{\rm ib} = R_{\rm ib,f} + (R_{\rm ib,i} - R_{\rm ib,f}) \cdot \exp(-t/t_0)$. Here $R_{\rm ib,i}$ is the radius corresponding to an enclosed mass of 1.1 $M_\odot$ at about 10 ms after bounce. It is typically around 60 km. For the contraction timescale, we use $t_0 = 0.4$ s, and for the final radius, $R_{\rm ib,f} = 20$ km (see also Ugliano et al. 2012).

The neutrino emission of the excised core, which defines the boundary condition for the neutrino transport at the inner grid boundary, is computed from an analytic one-zone model (see Ugliano et al. 2012; Sukhbold et al. 2016). The model equations are based on the requirements of energy conservation and the validity of the virial theorem. The relative weights of neutrinos and antineutrinos are constrained by the lepton number loss associated with the neutronization of the PNS core (Scheck et al. 2006). The values of the parameters in this analytic model are thus constrained by (global) physics arguments, but three of them are varied within small ranges to obtain explosions in 1D that are in agreement with observationally constrained energies and ^{56}Ni masses of the well-studied SN 1987A and SN 1054-Crab. These two observational cases are used to calibrate our "neutrino engine" that drives explosions in spherical symmetry. This choice is motivated, on the one hand, by the fact that the Crab supernova had a low explosion energy (only around 10^{50} erg) with little nickel production (some 10^{-3} $M_\odot$), and the gaseous remnant has a high helium abundance and relatively oxygen-poor filaments. These characteristics are compatible with the explosion of a low-mass star with an extremely low core compactness value. On the other hand, SN 1987A had an explosion energy over 10^{51} erg and expelled about 0.07 $M_\odot$ of ^{56}Ni and roughly 1 $M_\odot$ of oxygen, classifying it as a more "normal" supernova of a massive star greater than 15 $M_\odot$. For a detailed discussion, see Sukhbold et al. (2016).

Following Sukhbold et al. (2016), we use a 9.6 $M_\odot$ star (model Z9.6) for a Crab progenitor and a set of 15, 18, and 20 $M_\odot$ blue supergiant stars (models W15, W18, W20, and N20), as well as a 19.8 $M_\odot$ red supergiant star (model S19.8), as SN 1987A progenitors. The values of the PNS core parameters for these neutrino engines, calibrated by comparison to Crab and SN 1987A, are listed in Table 3 of Sukhbold et al. (2016). In addition, we also tested several of the binary progenitor models proposed for SN 1987A by Menon & Heger (2017) and found that all of them could be exploded with at least one of our sets of engine-parameter values from single-star progenitors to yield reasonable agreement with the explosion energy and nickel production of SN 1987A (see Appendix A). Therefore, the binary progenitors of SN 1987A do not provide any new neutrino engines but can be considered as variants of the already available single-star engines.

In the present paper, we will present results of all engines used by Sukhbold et al. (2016), but for a detailed analysis of population-integrated supernova outcomes, we will mostly focus on Z9.6 in combination with W18. The latter provides a neutrino engine not much below the strongest ones (N20 and S19.8), and its choice allows for detailed comparisons with single-star results discussed by Sukhbold et al. (2016). In practice, we interpolate the PNS core model parameters between the Z9.6 and SN 1987A engines in terms of a parameter M_{3000}, which measures the mass enclosed by a radius of 3000 km in the core of the precollapse star. This

interpolation provides a smooth transition from "Crab-like" to "SN 1987A–like" cases. For details, see again Sukhbold et al. (2016).

In all simulations, the EOS of Lattimer & Swesty (1991) with $K = 220$ MeV is used for $\rho \geqslant 10^{11}$ g cm^{-3}. At lower densities, a multicomponent EOS is employed that includes radiation, electrons, positrons, and ions. The composition is followed using two approximations. Above a temperature of 7×10^9 K, NSE is assumed, and the composition is tracked using a table that includes, as a function of ρ, T, Y_e, the 13 α-nuclei, neutrons, protons, and a "tracer nucleus" (Tr) that represents neutron-rich nuclei and replaces ^{56}Ni in regions where $Y_e < 0.49$ and neutron-rich species are expected to become abundant. Neutrino capture and electron and positron capture on neutrons and protons are followed so that Y_e evolves with time (for the neutrino treatment, see Scheck et al. 2006). For temperatures between 7×10^9 and 10^8 K, the composition is followed using a reaction network that links the 13 α-nuclei by the triple-α reaction for helium, subsequent (α, γ) reactions for nuclei with atomic mass numbers, $A < 28$, the faster (α, p) (p, γ) reaction channel compared to the latter for $A \geqslant 28$, and heavy-ion reactions, ^{12}C(^{12}C, α)^{20}Ne, ^{12}C(^{16}O, α)^{24}Mg, ^{16}O(^{16}O, α)^{28}Si (original version by Müller 1986, upgraded by Kifonidis et al. 2003). In regions where lepton capture on nucleons has reduced Y_e below 0.49, the tracer nucleus Tr replaces ^{56}Ni in the network and is produced instead of it by the reaction ^{52}Fe$(\alpha, p)(p, \gamma)^{56}$Ni. The small network approximately tracks the explosive burning of carbon, oxygen, and silicon as the shock moves out. Material that has been above 7×10^9 K and is ejected has its composition followed in the small network as it expands and cools down, so that, e.g., the helium has an opportunity to recombine. In regions where silicon has been depleted, i.e., regions that have attained NSE, the final composition consists of a mixture of helium from photodisintegration, ^{56}Ni from regions where Y_e has remained greater 0.49 at all times, and Tr, a partially neutronized species whose actual identity reflects the history of weak interactions in the matter but is not well determined in P-HOTB.

As in Ertl et al. (2016a) and Sukhbold et al. (2016), the network and EOS are fully self-consistently coupled, thus taking into account the energy release by nuclear reactions for the hydrodynamical evolution of the explosion.

A number of improvements have been implemented in the P-HOTB code since the work of Sukhbold et al. (2016).

(1) In solving the neutrino-transport equation by an analytic method (see Scheck et al. 2006), the energy source term associated with neutrino–nucleon scattering (whose average energy transfer per scattering reaction is taken into account) is not described in a closed form as in Scheck et al. (2006) but is split into an absorption part and emission part of energy. This considerably improves the numerical stability of the transport integrator.

(2) For the long-time simulations of supernova explosions over several weeks, the radioactive decays of freshly produced ^{56}Ni to ^{56}Co (half-life 6.077 days) and ^{56}Co to stable ^{56}Fe (half-life 77.27 days) are included. This has some influence on the expansion velocities of the innermost ejecta shells (see Jerkstrand et al. 2018) and a minor effect on the late-time fallback.

(3) An adaptive grid-refinement algorithm is added to ensure that the density differences between neighboring grid cells in the PNS surface layers obey the constraint $\Delta\rho/\rho \lesssim 6\%$. This improves the possibility of maintaining hydrostatic equilibrium for the increasingly steep density gradient at the PNS surface.

(4) For the long-time simulations during phases of homologous or nearly homologous expansion, a steerage algorithm moves the grid with the expanding matter. This reduces the numerical diffusion of, e.g., composition components, and it also reduces computational costs by allowing for larger time steps.

The first two points have some smaller consequences for the explosion results published by Ertl et al. (2016a) and Sukhbold et al. (2016), and in particular, point (1) leads to slightly more optimistic conditions for explosions. Therefore, with the improved P-HOTB code, we obtain a slightly larger number of exploding cases, in particular at the edges of ZAMS mass intervals where failures or fallback supernovae were obtained before. In Appendix A we provide a detailed comparison of explosion results obtained by Sukhbold et al. (2016) with the previous version of the P-HOTB code and results obtained for all neutrino engines with the present, upgraded version of the code.

The stellar collapse and explosion simulations are computed with a radial grid of up to 2000 zones. After core bounce, the grid is dynamically adjusted, and its number of zones varies between about 1300 and 2000. After usually 10–15 s, the neutrino cooling of the compact remnant is no longer followed, and the inner grid boundary is moved outward. Also, the outer grid boundary is relocated to larger radii as the supernova shock propagates through the progenitor star. We have confirmed by tests that the radial position of the inner grid boundary has no relevant effect on the computation of the fallback, which is determined by mass escaping through the inner grid boundary with negative velocities (see Ertl et al. 2016b).

The supernova explosions are typically followed for about 5 weeks. In order to perform these simulations beyond the breakout of the supernova shock from the stellar surface, the progenitor star is embedded in a dilute circumstellar medium. For this purpose, we assume a constant mass-loss rate $\dot{M}_{\rm w}$ and prescribe a wind velocity of $v_{\rm w}(r) = v_\infty \cdot (1 - R_*/r)$, where R_* is the radius of the progenitor star and v_∞ is the asymptotic velocity at large distances. This yields a wind-density profile of $\rho_{\rm w}(r) = \dot{M}_{\rm w} \cdot [4\pi r^2 v_{\rm w}(r)]^{-1}$. The temperature in the wind is computed by the assumption of hydrostatic equilibrium. For the supernova simulations discussed in this work, we used $\dot{M}_{\rm w} = 10^{-4}\, M_\odot$ yr^{-1} and $v_\infty = 10^8$ cm s^{-1}. With these values, the density in the first computational cell exterior to the star is typically 1–2 orders of magnitude lower than the density in the outermost cell of the stellar model. The corresponding total mass of the circumstellar medium within the computational grid with an outer boundary radius of 10^{18} cm is lower than $0.04\, M_\odot$. This mass, in addition to the precollapse mass of the progenitor, is so low that it has no dynamical influence on the expanding supernova ejecta.

3.2. *Modeling with* KEPLER

KEPLER is used to postprocess the explosions calculated by P-HOTB in order to capture the details of the nucleosynthesis and test for consistent results. This postprocessing is facilitated by the fact that the presupernova models used by P-HOTB were calculated using *KEPLER*, so the starting points are identical. It is complicated by the fact that P-HOTB uses an Eulerian grid, carries the PNS, and includes neutrino transport,

while *KEPLER* is Lagrangian and does neither. Since regions outside what will eventually be the final mass separation have their dynamics modified considerably by neutrino-energy deposition, postprocessing is not so simple as just taking the history of a single mass shell in P-HOTB and using that as a piston in *KEPLER*. Particularly problematic is matter that passes through the accretion shock in P-HOTB and dwells for a considerable time between that shock and the neutrinosphere while experiencing an irregular radial history. It may take up to a second for the explosion to develop in P-HOTB. Attempting to model this delay with a piston in *KEPLER* results in multiple bounces and the artificial accumulation of high-density matter just outside the piston.

In Sukhbold et al. (2016), the approach taken was to define a "special trajectory" in P-HOTB for use as a piston in *KEPLER* (see their Figures 10 and 11). This trajectory tracked the first mass shell to move outward vigorously once the stalled shock was revived. The radius of that shell contracted from a few thousand km to a minimum of 80–140 km (more typically 120–140 km) before rapidly moving out and being ejected. The mass inside this shell, its minimum radius, and the time at which the matter moved out defined the initial motion of a piston in the *KEPLER* calculation. The inward motion of that piston, from the time the core first collapsed, i.e., reached a collapse speed of $1000\,\mathrm{km\,s^{-1}}$ in any zone, to the time it reached its minimum radius was approximated by fitting a parabolic curve to the initial and final radius; see Equation (7) of Sukhbold et al. (2016). Its subsequent outward motion was given by a ballistic trajectory in a modified gravitational field, i.e., a constant times the local Newtonian acceleration due to gravity. Given the assumed final radius of the piston, 10^9 cm, the strength of this field, and hence the transit time to 10^9 cm, was adjusted so that the kinetic energy of all ejecta at late time agreed with the P-HOTB simulation. By design then, the explosion energy in *KEPLER* and the initial mass separation were the same as in P-HOTB. Subsequent fallback was followed independently in both codes and usually agreed well. All remnant masses (e.g., those used in Section 6) were taken from the P-HOTB simulation and not *KEPLER*.

For the piston trajectory just described, the nucleosynthesis of the iron group and ^{56}Ni usually agreed quite well between the two codes. Most of the ^{56}Ni made in P-HOTB was produced outside of the special trajectory, so its synthesis was accurately captured by *KEPLER*. Between the special trajectory and the deeper final mass separation, however, there was matter in P-HOTB with an electron mole number, Y_e, that had been affected by neutrino capture during both the delayed explosion and the neutrino-powered wind that followed. As discussed in Section 3.1, this matter consisted, in P-HOTB, of helium from photodisintegration and iron-group elements, Tr, with an uncertain isotopic composition. For all models in Sukhbold et al. (2016), the mass in the form of Tr was much less than that of ^{56}Ni, so fitting the total iron (^{56}Ni plus other "neutronized" isotopes) well also resulted in fitting ^{56}Ni well. In the end, the total iron-group synthesis in *KEPLER* always fell between the values of Ni and Ni+Tr in all the matter ejected by P-HOTB. In some cases where this condition was not initially satisfied, the piston location was moved inward in *KEPLER* until it was. The adjustment was small, of order $0.01\,M_\odot$. Ultimately, the total ejected iron-group synthesis in *KEPLER* and P-HOTB agreed to within a few thousandths of a solar mass for models below $12\,M_\odot$ and about $0.02\,M_\odot$ for heavier models. The average difference in total iron ejected for the two codes was 24% or $0.014\,M_\odot$ (see Figure 12 and Tables 4 and 5 of Sukhbold et al. 2016).

While no additional modifications were made to tune the production of ^{56}Ni itself, it turned out that the agreement between the two codes was even better for that isotope. The ^{56}Ni production in *KEPLER*, on average, was within 9.8% ($0.005\,M_\odot$) of the P-HOTB values for just ^{56}Ni and 28% ($0.016\,M_\odot$) for ^{56}Ni+Tr. In the worst case, the ^{56}Ni-to-^{56}Ni comparison was off by $0.021\,M_\odot$.

In the present paper, iron and ^{56}Ni synthesis in *KEPLER* were computed this "old way," but an additional set of models was calculated that used a deeper mass cut for the piston location. Except for a few cases with large amounts of late-time fallback, this location was equal to the final mass separation in the P-HOTB simulation. For those cases with massive fallback, the nucleosynthesis of iron did not matter, and the final remnant mass was taken from P-HOTB, so the special trajectory continued to be used. Moving the mass cut in like this increases the production of iron and ^{56}Ni in *KEPLER*. Because interactions with neutrinos may have reduced Y_e in these deepest layers, the ^{56}Ni production is a maximum. The timing of the bounce and the minimum radius in this other set were still that of the "special trajectory," and the same agreement in final kinetic energy was enforced, but the initial location of the piston was deeper and not varied.

3.3. The Evaluation of Iron and ^{56}Ni Yields in P-HOTB and KEPLER

Because of the central role of ^{56}Ni in producing the light curves of SNe I, we discuss here how our best estimates were calculated and their possible error. Ultimately, six possibilities were considered, each with its own special meaning.

Part of the variation is because *KEPLER* and P-HOTB both calculate iron-group nucleosynthesis. *KEPLER* uses a large network that is necessary for determining isotopic and trace element nucleosynthesis, while P-HOTB uses a 13-species network (α-nuclei from helium through ^{56}Ni) for temperatures below 7×10^9 K, supplemented by a 15-species NSE solver for higher temperatures (Section 3.1; Kifonidis et al. 2003; Scheck et al. 2006; Ugliano et al. 2012; Ertl et al. 2016a). The dynamical history of zones near the mass cut is tracked more accurately by P-HOTB, which also calculates a 1D approximation to the neutrino-powered wind. To do so, it follows the evolution of ejecta near the mass cut for at least 10 s after core collapse. See Figure 10 of Sukhbold et al. (2016) for an example.

As discussed in Section 3.1, P-HOTB delineates its iron-group synthesis into three components, Ni, Tr, and α, and there is some ambiguity in the interpretation of each. The "Ni" component is the ^{56}Ni synthesized in the 13-isotope network and the 15-species NSE solver when Y_e is greater than 0.49. The "Tr" component is ^{56}Ni plus other iron-group species produced in both the network and the NSE solver when $Y_e < 0.49$, especially in the neutrino-powered wind. In the present studies, Y_e was typically ~0.46–0.49 in the wind region, and thus Tr would contain essentially no ^{56}Ni. Other more realistic studies have shown, however, that Y_e in the wind should be close to or even greater than 0.50 (Martínez-Pinedo et al. 2012; Roberts 2012; Mirizzi et al. 2016). Studies by, e.g.,

Pruet et al. (2006) show the fraction of heavy species that are ^{56}Ni is 30%–80% for Y_e near 0.54. Consequently, we take the fraction of Tr that is ^{56}Ni here to be some uncertain fraction that might be near 0.5.

The α-particles are produced by photodisintegration in the shock but also in the wind at late times, where their mass fraction can approach 90%. The total mass of material that has achieved NSE in P-HOTB is bounded above by Ni+Tr+α. It is an upper bound, since the sum also includes a small amount of ^{56}Ni produced by incomplete explosive silicon burning for shock temperatures between 4 and 5×10^9 K. Since we are interested not just in best estimates but also in upper bounds (Section 8), it is possible that some greater fraction of the α-particles might reassemble in a multidimensional model. Regardless of dimensionality, a comparable amount of matter needs to absorb energy from neutrinos in order to obtain the observed energy of the supernova. In 1D, this mass expands like a wind; in 3D, it will come from overturn, accretion, and re-ejection of matter after heating. An open question is whether the average entropy of the bottommost layers ejected in a 3D explosion is less than in 1D. This would promote the assembly of more α-particles into ^{56}Ni. Coupled with the desire to explore the sensitivity of the light curves to the ^{56}Ni mass, this motivates treating the α-particles calculated here by P-HOTB as a potential mixture of ^{56}Ni and α. Studies with *KEPLER* with the mass separation at the P-HOTB value (Section 3.2) show that for matter ejected solely by shock heating, the average ^{56}Ni mass ejected is 75% of the matter that achieved NSE. This suggests that 0.75 times the sum of Ni+Tr+α from the P-HOTB calculation is an upper bound to the ^{56}Ni synthesis. It is an upper bound because *KEPLER* does not include neutrino capture.

Figure 9, shown later in the paper in Section 4.3, illustrates the possibilities. For the neutrino-powered models calculated here (see Section 8.5 for other possibilities), the least amount of ^{56}Ni is mainly the iron-group material that did not experience any appreciable change in Y_e during the explosion as modeled in P-HOTB. This is the thin black line at the bottom of the figure. It also contains the ^{56}Ni made by explosive burning in shock-heated ejecta plus ^{56}Ni produced by nuclear recombination in neutrino-heated wind matter for $Y_e \geqslant 0.49$. This last contribution is usually very small because the Y_e in neutrino-processed matter that ends up being ejected is $Y_e \sim 0.46$–0.49 in the P-HOTB models. Close to that, the blue line gives the *KEPLER* results for calculations using the special trajectory as the mass cut, the same approach used by Sukhbold et al. (2016; see Section 3.2). The two dashed lines are for Ni+Tr/2 and Ni +Tr as calculated by P-HOTB. As discussed in Section 3.1 it is probable that not all of the Tr is neutronized iron, but the fraction of ^{56}Ni is undetermined when the Y_e in the wind is lower than 0.49. The band between the two is our best estimate for ^{56}Ni synthesis in the current model set. The top solid black curve shows the *KEPLER* result when the mass cut is moved into the deepest possible value for the present models. It is very similar to the red curve, which is all of the ^{56}Ni, Tr, and helium from photodisintegration ejected by P-HOTB (i.e., essentially all the matter that has reached NSE) multiplied by 0.75. The factor 0.75 was chosen so that the two curves would match. The best value is thus in the gray band, and the two values explored as maxima and minima for the light curves (Section 8) are the red and blue lines. The results in the figure are for the W18 central engine, but those for S19.8 are similar.

4. Explosion Results Using P-HOTB

Before describing specific results for the various central engines, it is useful to define a maximum mass for cold neutron stars. This was unnecessary in our previous study (Sukhbold et al. 2016) because the progenitors there either blew up and formed neutron stars with baryonic (gravitational) masses below 2.15 $M_\odot$ ($\sim$1.8 $M_\odot$) or collapsed to compact remnants with masses well above 3 $M_\odot$. The latter value was beyond any mass limit that can be stabilized using present-day nuclear EOSs. In the new study of helium stars, though, there are many cases where the PNS has a baryonic mass between 2.5 and 3 $M_\odot$ at the time the explosion sets in. This is illustrated in Figure 2, which discriminates between the compact remnant mass at the onset of the explosion, $M_{\rm NS}(t_{\rm exp})$; the remnant mass before fallback, $M^{\rm bfb}_{\rm NS/BH}$; and the final remnant mass after fallback, $M_{\rm NS/BH}$. Revisiting our calculations of single stars using the revised version of P-HOTB (Appendix A) has also revealed a few cases where fallback lifts the baryonic mass of the compact object to between 2.5 and 3 $M_\odot$, even in the single-star case. Reasons for the variation are discussed in Section 4.4.

Here we choose a baryonic mass limit for neutron stars of 2.75 $M_\odot$, corresponding to a gravitational mass between $\sim$2.18 and $\sim$2.30 $M_\odot$ for neutron star radii between 9 and 12 km according to Equation (36) of Lattimer & Prakash (2001). This limit is compatible with estimates based on the gravitational wave and kilonova measurements associated with the first detection of a neutron star merger event in GW170817 (see, e.g., Margalit & Metzger 2017; Rezzolla et al. 2018). Since the thermal pressure of a hot neutron star can stabilize an additional mass of several 0.1 $M_\odot$ and thus increase the threshold mass for black hole formation (O'Connor & Ott 2011; Steiner et al. 2013), this is a lower bound for PNSs. All cases in Figure 2 that exceed the cold limit of $M_{\rm b,NS}(t_{\rm exp}) = 2.75\ M_\odot$ by only a small margin (crosses above the horizontal black line) are considered transiently stable hot neutron stars, whose neutrino emission can trigger supernova explosions. The circles represent the neutron star masses after the phase of neutrino cooling but before fallback. They are lower than the corresponding masses at $t_{\rm exp}$ (indicated by crosses) because of the mass that is blown away in the neutrino-driven wind. Plus signs mark the baryonic masses of the compact objects after fallback. They are treated as neutron stars when $M_{\rm b,NS/BH} \leqslant 2.75\ M_\odot$, otherwise as black holes. In the latter case, we obtain "fallback supernovae," i.e., low-energy explosions with black hole formation due to massive fallback, which in 1D simulations do not eject any iron-group material.

4.1. Dependence on the Central Engine

Three different outcomes of stellar core collapse can be distinguished: supernova explosions with neutron star formation, supernova explosions with black hole formation by massive fallback ("fallback supernovae"), and failed explosions with "direct" black hole formation, i.e., continuous accretion of the transiently existing neutron star until collapse to a black hole takes place ("Implosion and BH" in Figures 3 and 4).

Figures 3 and 4 show our results from P-HOTB simulations for all of the central engines employed for the set of helium stars with a standard mass-loss rate and the set with an enhanced mass-loss rate, respectively. The engines are named by the combination of Crab and SN 1987A progenitors, whose sets of parameter values are interpolated with a dependence on the core compactness (more

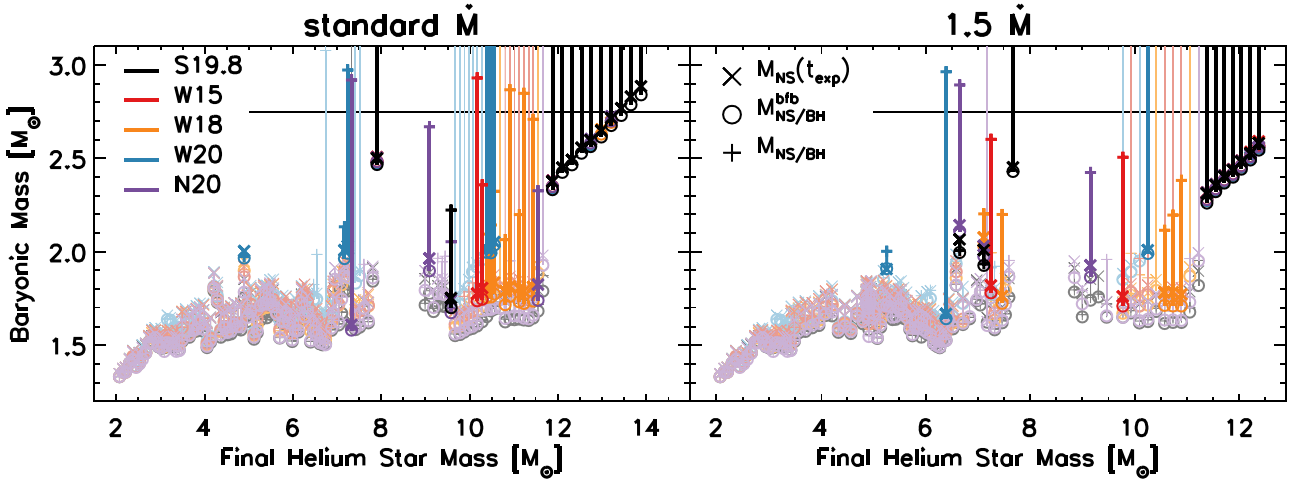

Figure 2. Baryonic neutron star mass vs. precollapse helium star mass in P-HOTB simulations of helium stars with standard mass loss (left) and enhanced mass loss (right) for all central engines (S19.8, W15, W18, W20, and N20). Three different masses are indicated by different symbols: $M_{\rm NS}(t_{\rm exp})$ is the neutron star mass at the time the explosion sets in (crosses), $M^{\rm bfb}_{\rm NS/BH}$ is the mass of the compact remnant after mass loss by the neutrino-driven wind but before fallback (open circles), and $M_{\rm NS/BH}$ is the final mass of the compact remnant including the mass accreted from fallback (plus signs). The dark colored symbols mark cases where at least one of these three masses lies between 2 and 3 $M_\odot$, whereas the light colored symbols correspond to all other cases. Different colors correspond to different engines, as noted by labels in the left panel. Vertical bars show the fallback masses, which are usually too small to be visible. The thin black horizontal line marks the baryonic mass limit of 2.75 $M_\odot$ assumed for cold neutron stars.

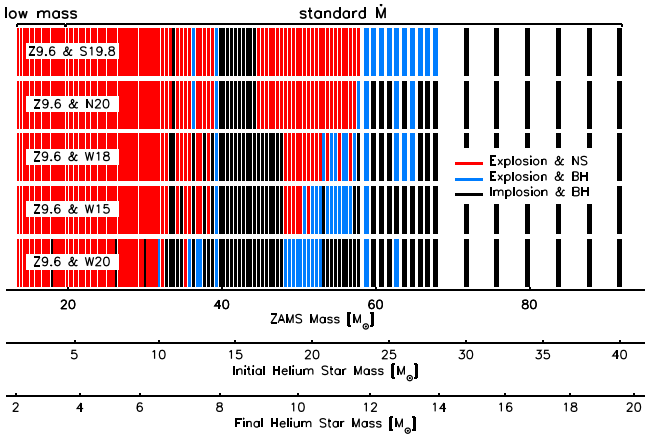

Figure 3. Outcome of core collapse in calculations with P-HOTB for helium stars with the standard mass-loss rate and all neutrino engines considered. Supernova explosions with neutron star formation are indicated by red bars, failed explosions with black hole formation by black bars, and supernova explosions with black hole formation due to massive fallback accretion ("fallback supernovae") by blue bars. The different engines are sorted by their strength. The strongest engine with the largest number of successful explosions is shown on top, the weakest engine at the bottom. The horizontal axes provide ZAMS mass (as estimated with Equations (4) and (5) of Woosley 2019), as well as initial and final helium star masses.

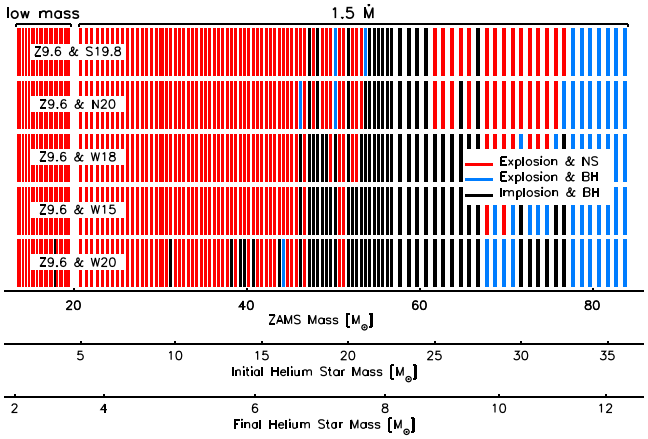

Figure 4. Same as Figure 3 but for the helium star models that employed an enhanced mass-loss rate during helium burning.

specifically, M_{3000}; see Section 3.1). The strongest neutrino engine is shown at the top, the weakest at the bottom. It is evident that the number of cases with supernova explosions and neutron star formation (red) decreases from top to bottom, whereas the number of cases with black hole formation, either by failed explosions (black) or fallback supernovae (blue), increases. While below a final helium star mass of about 6 $M_\odot$, essentially all progenitors blow up and give birth to neutron stars (with very few exceptions for the weakest engine), there is a mix of outcomes with neutron star or black hole formation for final helium star masses between ∼6 and nearly 12 $M_\odot$, where the strongest engine produces mostly successful explosions, and the weakest engine produces mostly black holes. Above a final helium star mass of ∼12 $M_\odot$ for the progenitors with standard mass loss and ∼11.3 $M_\odot$ for enhanced mass loss, only black hole formation by continuous or fallback accretion takes place.

A subset of the massive helium stars is especially interesting because they produce very massive PNSs before an explosion sets in (the baryonic neutron star masses at this time are between ∼2.3 and ∼2.9 $M_\odot$). Later, fallback triggers black hole formation (see Figure 2). This is the case for final helium star masses between ∼12 and 14 $M_\odot$ (ZAMS mass between ∼58 and 68 $M_\odot$) for standard mass loss, in particular with the three strongest neutrino engines, and for final helium star masses between ∼11.3 and 12.5 $M_\odot$ (ZAMS mass between ∼77 and 85 $M_\odot$) for enhanced mass loss and all neutrino engines. Below these mass windows, there is only a single exception of a lower-mass helium star with a similar behavior, namely a progenitor with a final helium star mass of nearly 8 $M_\odot$ (ZAMS mass ∼39 $M_\odot$) for the standard mass loss and one with a final helium star mass close to 7.7 $M_\odot$ (ZAMS mass ∼54 $M_\odot$) for the higher mass loss. In all of these cases, M_4, i.e., the mass where the dimensionless entropy per baryon reaches a value of $s = 4$, is large (>1.85 $M_\odot$). But the explosions set in even later, typically later than 1.5 s after bounce, at which time the neutron

star masses are considerably bigger than M_4. Consequently, the final explosion energies are low, less than $\sim 0.5 \times 10^{51}$ erg.

In these cases, M_4 underestimates the neutron star mass at the time the explosion sets in, because the star blows up only when matter whose entropy per baryon equals about 6 in the presupernova star collapses into the stalled shock. This roughly corresponds to the outer boundary of the convective oxygen-burning shell in the presupernova star and is often close to strong carbon- and neon-burning shells in cases where these shells have merged. At this location, the mass accretion rate makes another drop by about a factor of 2. Successful explosions in these cases occur because M_6 (which is the mass enclosed by the radius where $s = 6$) is still smaller than in other nonexploding progenitors, namely between about 2.3 and 2.9 $M_\odot$. Using M_4 instead of M_6 as a proxy of the neutron star mass and μ_4 as a parameter scaling with the mass accretion rate places these cases above the two-parameter curve separating neutron star formation from black hole formation in the $M_4\mu_4$–μ_4 plane (see Appendix B and Ertl et al. 2016a for the theoretical background), i.e., on the side of black hole formation. This is appropriate because it reflects the fact that these stars do not blow up when the infalling M_4 shell arrives at the shock, but they explode marginally only later with low energies and several solar masses of stellar material falling back onto the compact remnant.

In the following discussion of explosion results and their astrophysical consequences, we will focus on the two engines based on the W18 and S19.8 progenitors of SN 1987A. The reason is that the former allows for the most detailed comparison with the single-star results discussed by Sukhbold et al. (2016). The latter is our strongest neutrino engine, marginally beating N20, and thus is suitable to demonstrate the range of possibilities on the optimistic side for explosions. When this aspect is of relevance, we will also refer to our results with the S19.8 engine.

4.2. Conversion of Baryonic to Gravitational Masses

In our P-HOTB simulations, neutrino-energy loss from the newly formed compact remnant is taken into account by the binding energy of the analytic inner-core model plus the neutrino emission from the matter that gravitationally settles in the outer PNS layers followed directly by our hydrodynamics and neutrino-transport simulations. The description is very approximate. Nevertheless, detailed comparisons (D. Kresse et al. 2019, in preparation) reveal that the total release of neutrino energy, $E_{\nu,\mathrm{tot}}$, overestimates the binding energy computed from Equation (36) of Lattimer & Prakash (2001; see also Equations (9) and (10) of Sukhbold et al. 2016) only by a modest 10%–20% when neutron star radii of 11–12 km are used in these formulae. This difference not only stems from the rough approximations in our neutron star model but also results from the fact that the PNS is transiently more massive than the neutron star after its mass loss by the neutrino-driven wind and before fallback, i.e., $M_{\mathrm{b,NS}}(t_{\mathrm{exp}}) > M_{\mathrm{b,NS}}^{\mathrm{bfb}}$ (see Figure 2). It therefore radiates transiently more neutrinos than expected by the final neutron star mass. Such time-dependent effects of the dynamical supernova evolution in spherical symmetry are not captured by the formulae of Lattimer & Prakash (2001).

The difference implies a small underestimation of the gravitational neutron star mass by typically 0.02–0.04 $M_\odot$ in the P-HOTB simulations compared to the estimates derived on the grounds of Lattimer & Prakash (2001). For example, for neutron stars with baryonic masses of 1.4, 1.6, 1.8, 2.0, and 2.2 $M_\odot$, our P-HOTB simulations yield about 1.24, 1.40, 1.56, 1.71, and 1.90 $M_\odot$ for the gravitational masses, whereas Equation (36) of Lattimer & Prakash (2001) gives 1.27, 1.43, 1.60, 1.75, and 1.90 $M_\odot$ with $R_{\mathrm{NS}} = 12$ km and 1.26, 1.42, 1.58, 1.73, and 1.88 $M_\odot$ with $R_{\mathrm{NS}} = 11$ km. In the worst case and for a very massive neutron star, the gravitational mass of the cold remnant estimated with our neutrino loss in the P-HOTB simulation is lower by $\sim$0.1 (0.07) $M_\odot$ for a neutron star radius of 11 (10) km, corresponding to an underestimation of the gravitational neutron star mass by 4%–5% compared to the values derived from Equation (36) of Lattimer & Prakash (2001).

However, the gravitational wave and kilonova observations of GW170817 have set new constraints on neutron star radii, which reduce the uncertainties of the nuclear EOS in cold neutron stars. The numerical factors in Equations (35) and (36) of Lattimer & Prakash (2001) are averages over a wide range of possibilities, some of which are not compatible with the new radius constraints. Abbott et al. (2018) concluded that the radii of the two merger components (whose masses are most likely between $\sim$1.1 and $\sim$1.7 $M_\odot$) are $11.9^{+1.4}_{-1.4}$ km for EOSs that permit neutron stars with masses larger than 1.97 $M_\odot$ as required by observations (Antoniadis et al. 2013). Bauswein et al. (2017) argued that the radius of a nonrotating cold neutron star with a gravitational mass of 1.6 $M_\odot$ is larger than $10.68^{+0.15}_{-0.04}$ km, and the radius of the maximum mass configuration must be larger than $9.60^{+0.14}_{-0.03}$ km. Such small radii tend to favor higher binding energies than obtained with the numerical factors used in Equations (35) and (36) of Lattimer & Prakash (2001). The EOSs that are still compatible with the new constraints—for example, WFF2, AP3, AP4, ENG, and, on the very compact side, WFF1—are above the average line in Figure 8 of Lattimer & Prakash (2001). Therefore, they yield binding energies that are roughly 5%–25% higher than the mean value when neutron stars have gravitational masses exceeding $\sim$1.4 $M_\odot$.

For all of these reasons, we will use our P-HOTB results for the neutrino-energy loss of the newborn neutron stars in the whole paper. They are displayed in Figures 5 and 7, and they are employed to convert baryonic masses to gravitational masses of the compact remnants as given in Figures 6 and 8. For reference, we will also provide the numbers derived with Equation (36) of Lattimer & Prakash (2001) when we discuss initial mass function (IMF)–averaged masses.

Different from our approach in the previous works on single stars (Ertl et al. 2016a; Sukhbold et al. 2016; see also Appendix A), the greater number of present cases with massive fallback motivates us now to also take into account the release of the gravitational binding energy associated with the accretion of fallback matter. Because the neutrino-energy release calculated with P-HOTB and the values computed from Equation (36) of Lattimer & Prakash (2001) exhibit close agreement, we use the latter formula for estimating the energy loss from accretion. Several cases need to be distinguished.

(1) In the case of direct black hole formation by continuous accretion without supernova explosion, the neutron star is assumed to collapse to a black hole when it reaches a baryonic mass of $M_{\mathrm{b,NS}}^{\mathrm{max}} = 2.75\ M_\odot$.

(1a) If this limiting mass is reached during the P-HOTB simulation, we use the neutrino-energy output $E_{\nu,\mathrm{tot}}$ from the simulation to estimate the gravitational mass of the black hole

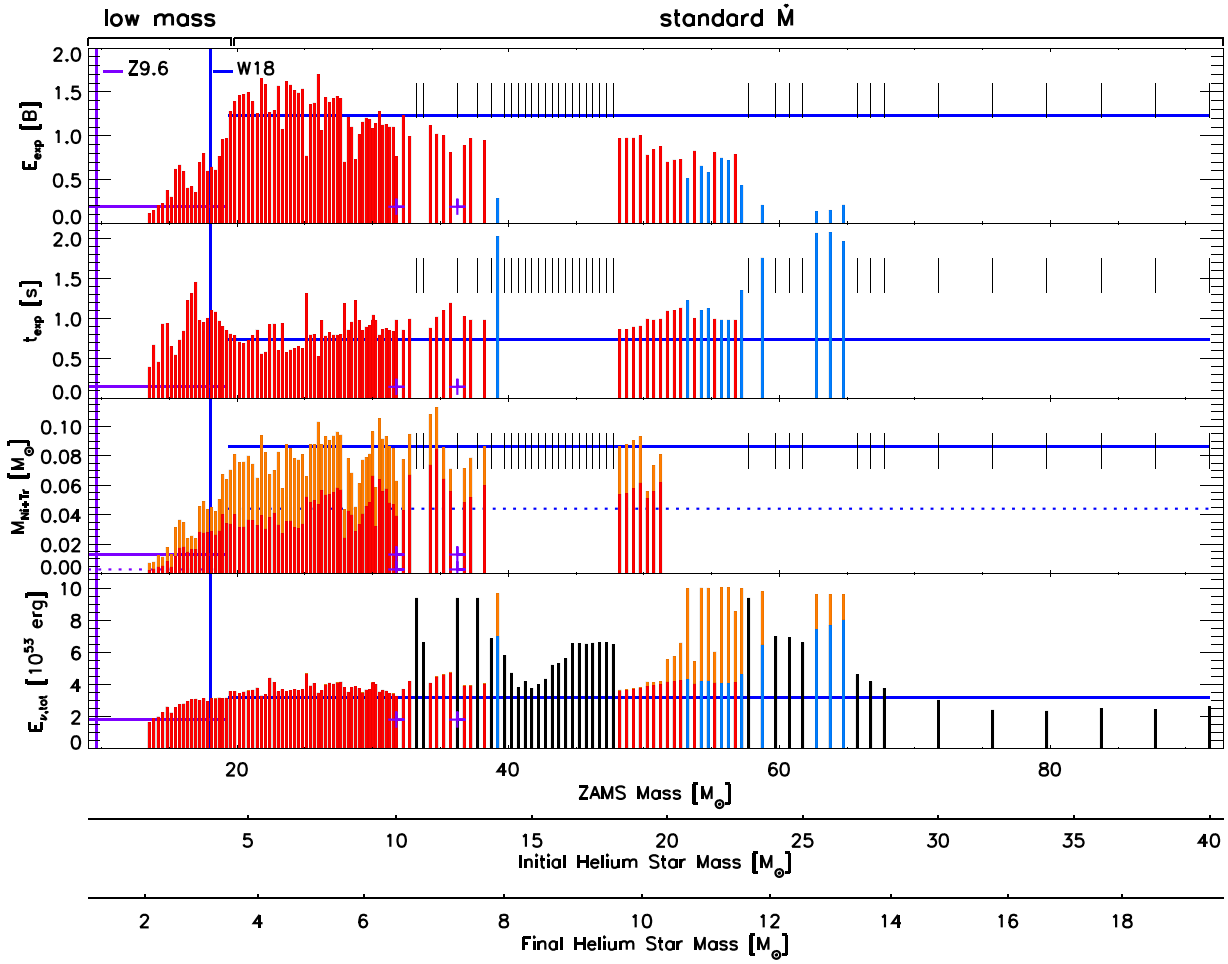

Figure 5. Overview of the explosion properties for our full set of helium star models with standard mass-loss rate, computed with the P-HOTB code and the Z9.6 and W18 neutrino engine. From top to bottom, the panels show the final explosion energy (1 B = 10^{51} erg), the time the explosion sets in (i.e., when the supernova shock expands beyond 500 km), the summed mass of the finally ejected ^{56}Ni (red) plus tracer (orange), and the total energy radiated in neutrinos, which takes into account the additional neutrino loss from fallback accretion (orange sections of the histogram bars). Red histogram bars denote the cases of neutron star formation, black bars denote those of "direct" black hole formation by continuous accretion, and blue bars correspond to cases where an explosion takes place but the final baryonic mass of the compact remnant exceeds our assumed black hole formation limit of 2.75 $M_\odot$. Nonexploding cases are marked by thin, short, vertical black dashes in the upper part of each panel. The vertical purple and blue lines mark the masses of the engine models, Z9.6 and W18, respectively, and the corresponding results of these engine models are indicated by solid and dashed horizontal purple and blue lines. The mass range spanned by the horizontal purple line of model Z9.6 indicates the region of Crab-like behavior, where the Crab and SN 1987A engines are interpolated.

by

$$M_{\rm g,BH} = M_{\rm b,BH} - \frac{1}{c^2}\, E_{\nu,\rm tot}(M_{\rm b,NS}^{\rm max}). \quad (1)$$

Here $M_{\rm b,BH}$ is the total mass of the stellar matter that collapses into the black hole, and we assume that the loss of energy from matter accreted after black hole formation is negligible. This assumption holds well for radial accretion, in which case neutrinos (and, of course, photons as well) do not have enough time to efficiently escape from the fast inward flow. Moreover, we make the approximation that thermal stabilization of the hot neutron star has a minor effect; i.e., we take our assumed mass limit for cold neutron stars to also set the limiting mass of the accreting remnant. This is valid only when the accretion proceeds slowly and the neutron star survives for a long period of time to cool efficiently. However, if the neutron star collapses on a short timescale compared to the cooling timescale, our approximation is acceptable as well, because the neutrino-energy loss in this case is fairly small, and therefore the gravitational-to-baryonic mass difference accounts only for an insignificant correction to the black hole mass.

(1b) If the accreting neutron star does not reach the limiting mass of $M_{\rm b,NS}^{\rm max} = 2.75\ M_\odot$ until our P-HOTB simulations are terminated at $t_{\rm end} = 10$ s after bounce, we extrapolate its further energy loss by using the Lattimer & Prakash (2001) estimate. The gravitational black hole mass is therefore calculated as

$$M_{\rm g,BH} = M_{\rm b,BH} - \frac{1}{c^2}\, \max\{E_{\nu,\rm tot}(t_{\rm end}),\, E_{\rm b,10\,km}^{\rm LP01}(M_{\rm b,NS}^{\rm max})\}, \quad (2)$$

where $E_{\rm b,10\,km}^{\rm LP01}(M_{\rm b,NS}^{\rm max})$ is the binding energy of a cold, maximum mass neutron star of 10 km radius according to Equation (36) of Lattimer & Prakash (2001). In practice, its value is higher than the neutrino-mass decrement obtained in the P-HOTB simulation at $t_{\rm end}$.

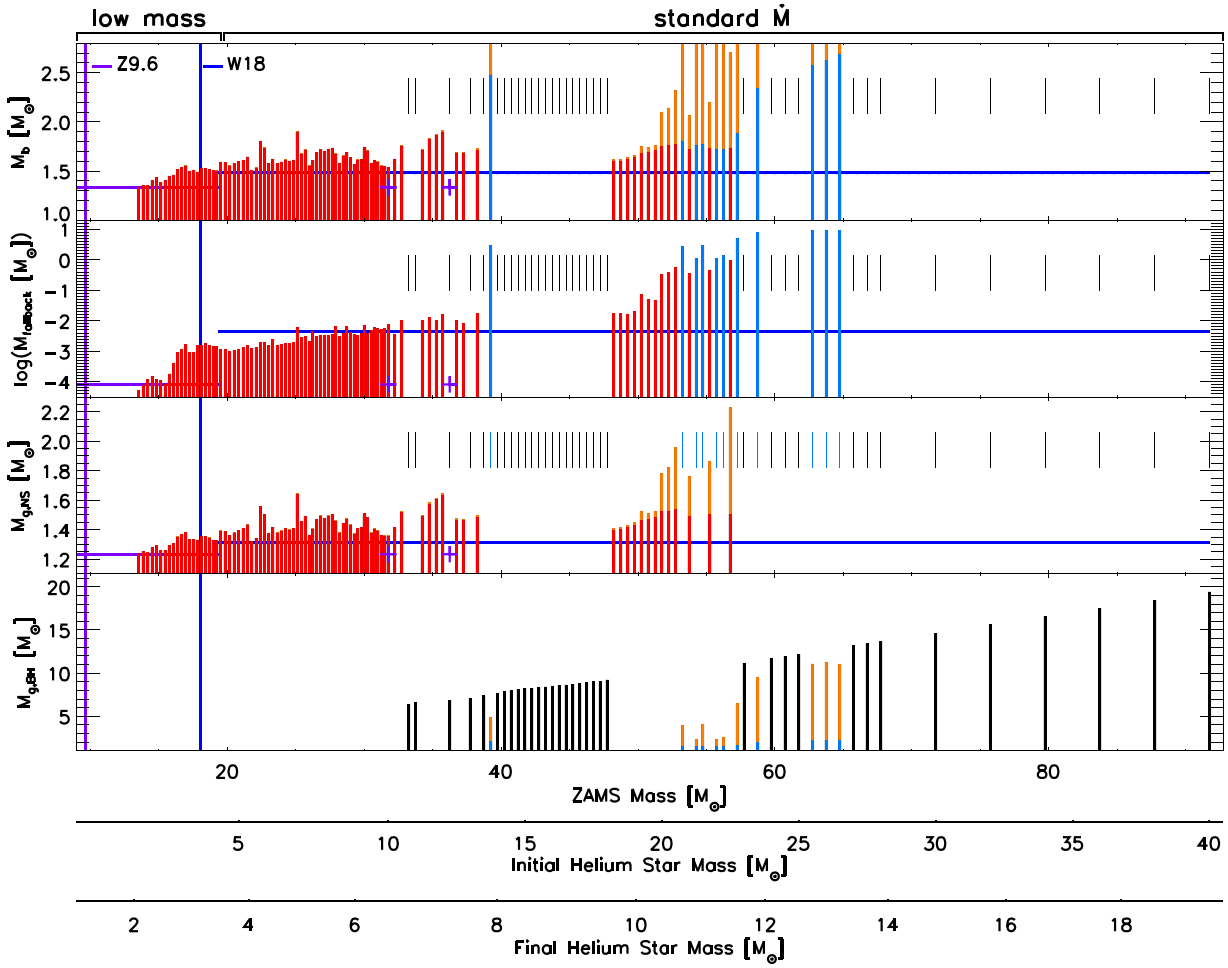

Figure 6. Overview of the properties of the compact remnants for our full set of helium star models with standard mass-loss rate, computed with the P-HOTB code and the Z9.6 and W18 neutrino engine. Red histogram bars denote the cases of neutron star formation, black bars denote those of "direct" black hole formation by continuous accretion, and blue bars correspond to cases where an explosion takes place but the final baryonic mass of the compact remnant exceeds our assumed black hole formation limit of 2.75 $M_\odot$. From top to bottom, the panels show the final baryonic mass of the remnant, with the fallback mass indicated by the orange part of the histogram bar; the logarithm of the fallback mass; the gravitational mass of the neutron star, with the fallback contribution again indicated by the orange section of the bar; and the gravitational mass of the black hole, also including the fallback contribution marked by the orange sections. In all blue cases where black holes form by fallback accretion, the fallback mass is close to 1 $M_\odot$ or higher. Gravitational masses for neutron stars and black holes are computed from baryonic masses as detailed in Section 4.2, including neutrino losses from fallback matter. Nonexploding cases are marked by thin, short, vertical black dashes in the upper part of each panel.The vertical purple and blue lines mark the masses of engine models Z9.6 and W18, respectively, and the corresponding results of these engine models are indicated by solid and dashed horizontal purple and blue lines. The mass range spanned by the horizontal purple line of model Z9.6 indicates the region of Crab-like behavior, where the Crab and SN 1987A engines are interpolated.

(2) In the case of black hole formation by fallback accretion, we compute the gravitational black hole mass according to

$$M_{\rm g,BH} = M_{\rm b,NS}^{\rm bfb} + M_{\rm fb} - \frac{1}{c^2} E_{\rm b,NS}^{\rm max}, \quad (3)$$

where $M_{\rm fb}$ is the fallback mass and $M_{\rm b,NS}^{\rm bfb}$ the baryonic mass of the transiently stable neutron star before fallback, whose neutrino emission has triggered the supernova explosion. The maximum binding energy of a neutron star is assumed to be

$$E_{\rm b,NS}^{\rm max} = E_{\nu,\rm tot}(t_{\rm end}) + E_{\rm b,fb}^{\rm LP01}. \quad (4)$$

Here we estimate the neutrino-energy release associated with the fallback, $E_{\rm b,fb}^{\rm LP01}$, by employing Equation (36) from Lattimer & Prakash (2001) for computing the difference between the binding energy of the final neutron star when it collapses to a black hole and the initial neutron star mass before fallback accretion:

$$E_{\rm b,fb}^{\rm LP01} = E_{\rm b,10\,km}^{\rm LP01}(M_{\rm b,NS}^{\rm max}) - E_{\rm b,12\,km}^{\rm LP01}(M_{\rm b,NS}^{\rm bfb}). \quad (5)$$

This assumes that fallback accretion proceeds slowly enough, and therefore the accreting neutron star remains stable for a sufficiently long period of time, to allow all of the binding energy to be radiated away.

Neutrino- or radiation-energy loss by further radial (in 1D) accretion after black hole formation is again assumed to be negligible. In the few cases of the standard mass-loss set of progenitors where $M_{\rm b,NS}^{\rm bfb} > M_{\rm b,NS}^{\rm max} = 2.75\ M_\odot$ (see Figure 2, left panel), we expect that the neutron star collapses to a black hole due to neutrino emission after 10 s of simulated post-bounce evolution. Therefore, in these cases, we also consider no additional neutrino-energy loss during the fallback accretion by the black hole.

(3) For consistency, we also include mass decrement corrections due to neutrino and radiation loss from fallback

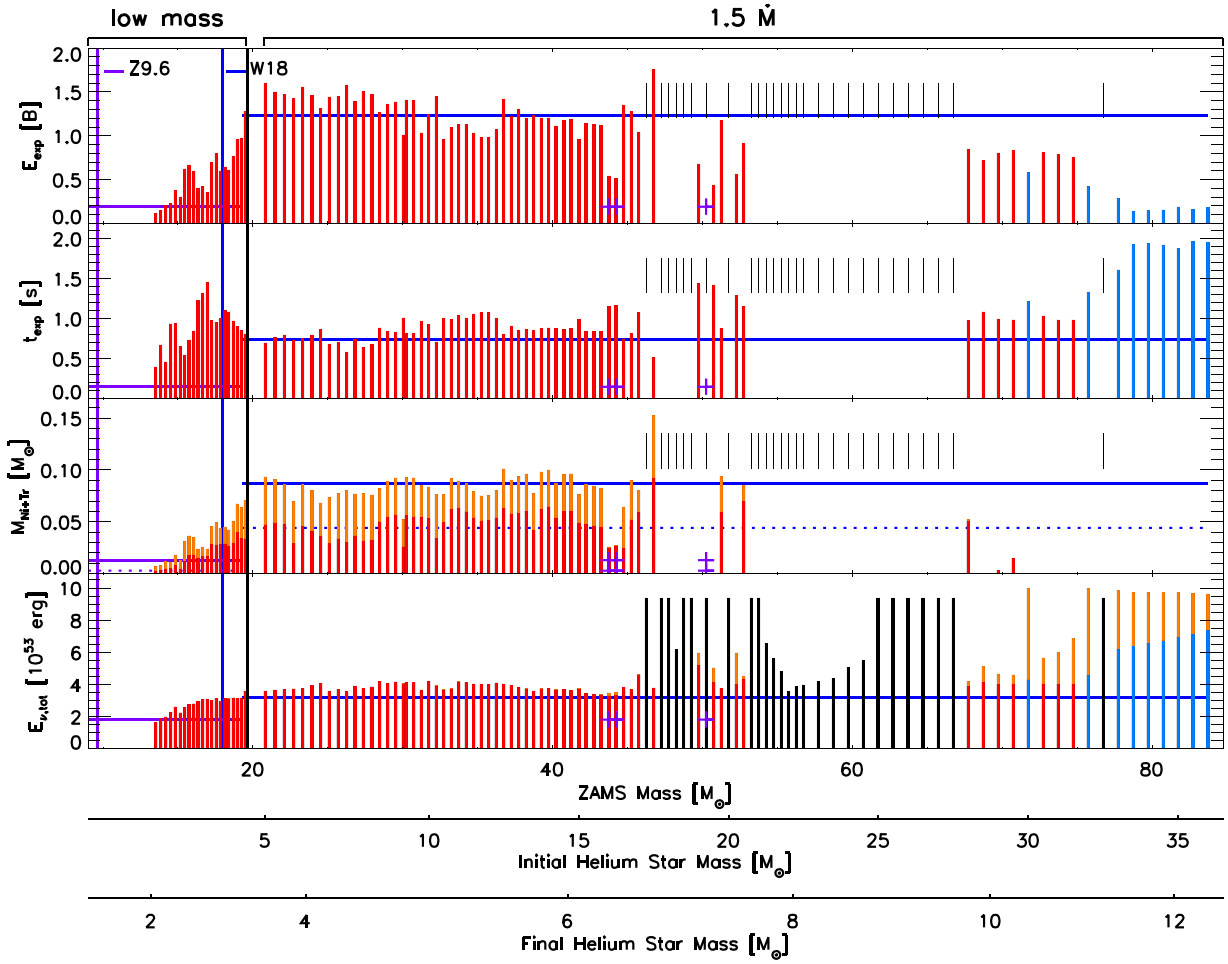

Figure 7. Same as Figure 5 but for the full set of helium star models with increased mass-loss rate (right of the black vertical line).

matter accreted by the stable neutron stars in our simulations, although these corrections are minuscule in the vast majority of cases because of the usually small fallback masses. In order to do that, we follow a procedure analog to the one applied in point (2). The corrected gravitational mass of the neutron star is

$$M_{\rm g,NS} = M_{\rm b,NS}^{\rm bfb} + M_{\rm fb} - \frac{1}{c^2} E_{\rm b,NS}(M_{\rm b,NS}), \quad (6)$$

where $M_{\rm b,NS}^{\rm bfb}$ is the baryonic mass of the neutron star before fallback, and $M_{\rm b,NS}$ is the final baryonic neutron star mass including fallback. The binding energy of the final neutron star is taken to be

$$E_{\rm b,NS}(M_{\rm b,NS}) = E_{\nu,\rm tot}(t_{\rm end}) + E_{\rm b,fb}^{\rm LP01}, \quad (7)$$

with

$$E_{\rm b,fb}^{\rm LP01} = E_{\rm b,12\,km}^{\rm LP01}(M_{\rm b,NS}) - E_{\rm b,12\,km}^{\rm LP01}(M_{\rm b,NS}^{\rm bfb}). \quad (8)$$

Again, we estimate the neutrino-energy release associated with the fallback, $E_{\rm b,fb}^{\rm LP01}$, by employing Equation (36) from Lattimer & Prakash (2001), but now we compute the difference between the binding energy of the final neutron star and the binding energy of the neutron star before fallback by adopting a radius of 12 km both times.

We finally repeat that only in a tiny subset of our present simulations is the assumed baryonic neutron star mass limit of $2.75\,M_\odot$ exceeded at the time the explosion sets in, i.e., $M_{\rm b,NS}(t_{\rm exp}) > 2.75\,M_\odot$ (see Figure 2, left panel). However, the overshoot is so small that we can safely assume that thermal pressure stabilizes the neutron stars long enough for them to power the associated weak fallback supernova explosions by their neutrino emission. We also treat these neutron stars such that they survive for the full simulation time of 10 s to radiate neutrinos. This is a crude assumption. But since these cases have high fallback masses and give birth to black holes of $\sim 10\,M_\odot$ or more, this implies only minor errors in our estimates of the black hole masses.

4.3. Results for the W18 Central Engine

Figures 5–8 summarize the P-HOTB simulations of helium stars with standard and enhanced mass-loss rates that use the Z9.6 and W18 engine. Cases with neutron star formation are shown by red bars, fallback supernovae with black hole formation by blue bars, and black hole formation without explosion by black bars. The direct black hole formation cases are also marked by short vertical black dashes in the upper halves of all panels, and the fallback black hole formation cases are marked by short vertical blue dashes in some panels.

Overall, the explosion energies and timescales, Ni+Tr masses, and remnant masses for the helium stars are quite similar to those for single stars; see Sukhbold et al. (2016) and Appendix A. The minimum values of the explosion energy, $E_{\rm exp}$, with the Z9.6 and W18 engine are near 10^{50} erg, and the maximum values are near 1.8×10^{51} erg. The corresponding

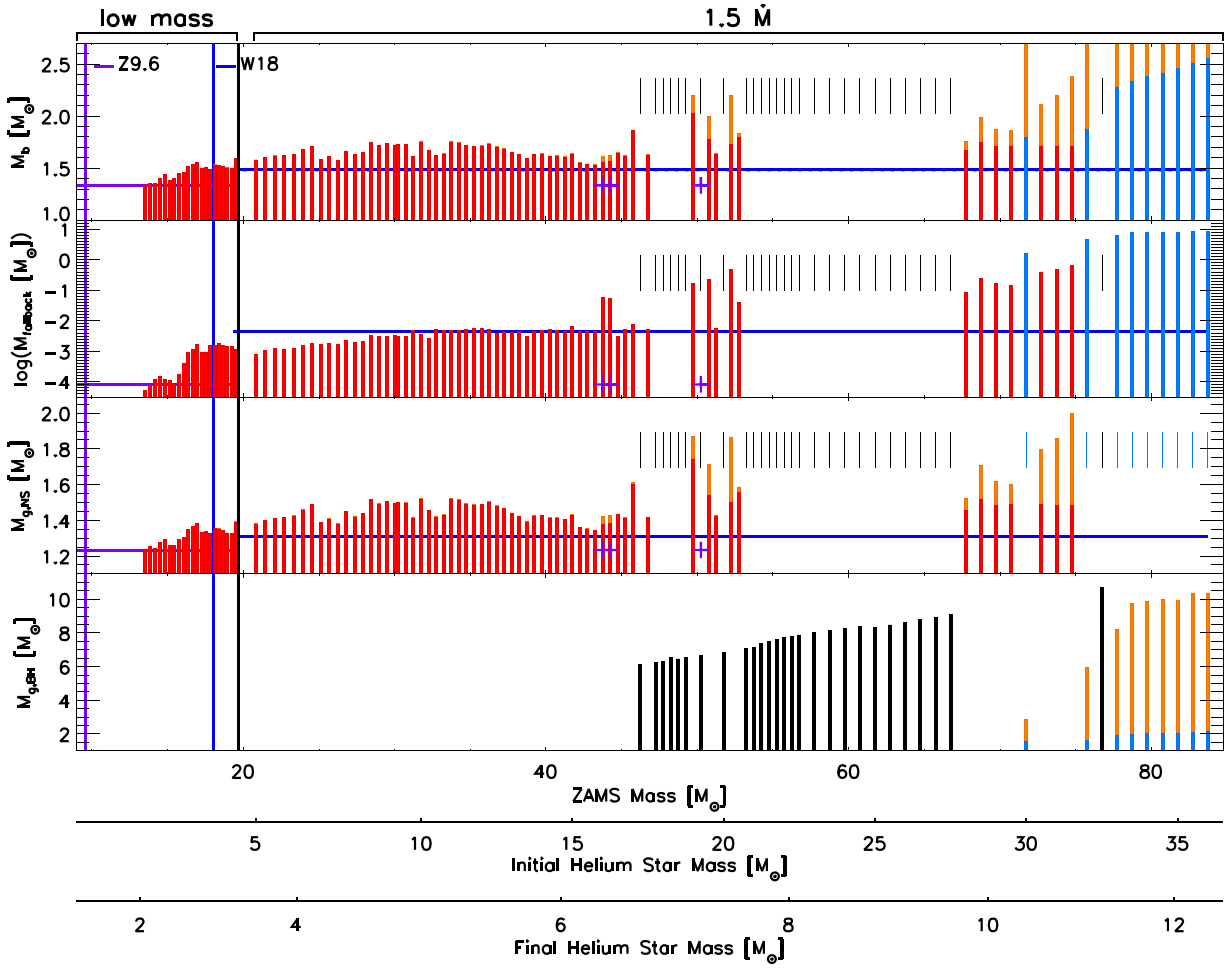

Figure 8. Same as Figure 6 but for the full set of helium star models with increased mass-loss rate (right of the black vertical line).

Ni+Tr masses range from $\sim 0.007\,M_\odot$ for the weakest explosions to $\sim 0.10\,M_\odot$ for the most energetic ones. A single outlier in the model set with enhanced mass loss produces slightly more than $0.15\,M_\odot$ (Figure 7). This star, with an initial helium star mass of $17.5\,M_\odot$, exploded unusually early with a high energy of 1.75×10^{51} erg and a correspondingly high yield of Ni+Tr. These special explosion conditions resulted because the base of the oxygen shell was characterized by an exceptionally high entropy jump (roughly from $s \approx 2.5$ to a value near 6), leading to a more dramatic drop of the mass accretion rate than for neighboring stars with similar helium star masses and values of M_4.

The lowest fallback masses of less than $10^{-4}\,M_\odot$ were obtained for the helium stars with the smallest precollapse masses and the lowest explosion energies, while the more typical cases had fallback masses between $\sim 10^{-3}$ and roughly $10^{-2}\,M_\odot$. Only for progenitors with initial helium star masses above about $15\,M_\odot$ did fallback significantly greater than $10^{-2}\,M_\odot$ become more frequent.

The estimated gravitational masses of the neutron stars ranged from about $1.24\,M_\odot$ up to $\sim 2.23\,M_\odot$ for a progenitor of roughly $57\,M_\odot$ ZAMS mass ($22.50\,M_\odot$ initial helium star mass) in the standard mass-loss set. For this heavy case, fallback of nearly $1.0\,M_\odot$ lifted the baryonic mass of the compact remnant to $\sim 2.71\,M_\odot$, which was just below our assumed mass limit for cold neutron stars. A similarly high value of $M_{\rm g,NS} \approx 2\,M_\odot$ ($M_{\rm b,NS} \approx 2.4\,M_\odot$) came from another progenitor of $\sim 75\,M_\odot$ ZAMS mass ($31.50\,M_\odot$ initial helium star mass) for the model set with enhanced mass loss.

The black hole masses range from values just above the threshold mass for black hole formation, to $\sim 19.5\,M_\odot$ for the most massive helium stars with standard mass loss, to $\sim 10.7\,M_\odot$ for the set with a higher mass-loss rate. At the lower end, the black hole mass was set by fallback; at the upper end, the entire presupernova star collapsed.

The most obvious difference of the helium star explosions compared to the single-star models of Sukhbold et al. (2016; see also Appendix A) is the greater number of cases with significant fallback. These fill in a "gap" in the remnant mass distribution that might have existed between gravitational masses of about 2–$6\,M_\odot$. Most cases where black holes are formed by fallback are associated with progenitors that explode very late ($t_{\rm exp} \sim 2$ s) at the time the infalling point with entropy per baryon 6.0 reaches the shock. Such cases form massive PNSs (see Section 4.1) that explode with relatively low energies (about $(1$–$4) \times 10^{50}$ erg) and eject no iron-group material (in the absence of mixing). The fallback includes much of the progenitor mass. Typically, 2–$3\,M_\odot$ is still ejected in models with standard mass loss but only 1–$1.5\,M_\odot$ for the most massive helium stars with enhanced mass loss. We estimate the neutrino-energy release in such cases (including the energy loss from fallback accretion) to be up to $\sim 10^{54}$ erg (or about $0.55\,M_\odot$), very similar to black hole formation by continuous slow accretion.

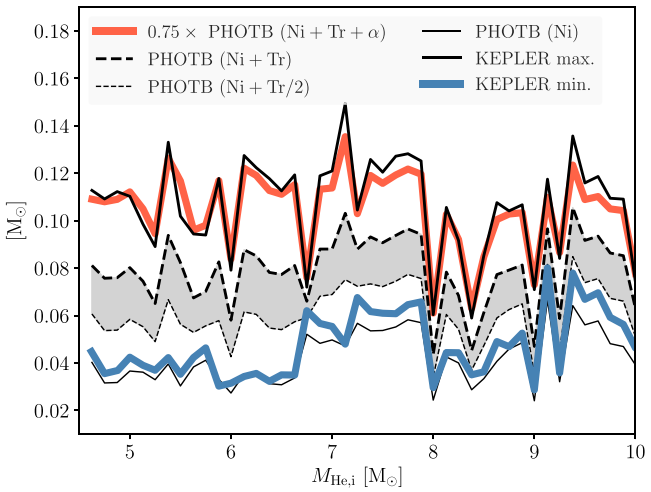

Figure 9. Production of ^{56}Ni for various assumptions in P-HOTB and *KEPLER* vs. initial helium star mass. The explosion simulations of the helium stars with standard mass-loss rate were performed with the Z9.6 and W18 neutrino engine. The thick solid black line is the ^{56}Ni production in the *KEPLER* code when the piston is located at the final mass cut in the explosion. It is an upper bound. The red curve is 75% of the matter that has experienced NSE in P-HOTB plus a small amount made by explosive silicon burning. The gray band bounded by dashed black lines is our estimate of the most likely ^{56}Ni production in the explosion. The lines are Ni+Tr (top) and Ni+Tr/2 (bottom) from the P-HOTB simulation. The blue line is the production in *KEPLER* when the special trajectory (Sukhbold et al. 2016) is used. The thin solid black line is just the ^{56}Ni produced in the P-HOTB simulation with no contribution from the wind or matter that has experienced weak interactions to get ejected with $Y_e < 0.49$. See the discussion in Section 3.3. The red and blue lines were used to compute maximum and minimum light curves in Section 8.

Also, the black holes with the lowest masses originate from fallback accretion. In the standard mass-loss set, these are just above the gravitational mass threshold for black hole formation, namely 2.31, 2.29, and 2.56 $M_\odot$ for final helium star masses of 10.91, 11.23, and 11.34 $M_\odot$, respectively. In the progenitor set with enhanced mass loss, there is a similar case with 2.89 $M_\odot$ for the fallback black hole in a star with a final helium star mass of 11.38 $M_\odot$.

In the context of this work, the production of radioactive nickel during the explosion is of particular interest. A detailed discussion of the associated uncertainties, which are connected to our simplifications of the explosion modeling, was provided in Section 3.3. For a subset of stars with initial helium star masses between about 4.6 and 10 $M_\odot$ and standard mass loss exploded with the Z9.6 and W18 neutrino engine, Figure 9 displays lower and upper estimates of the nickel yields compared to our best estimates. Five different quantities are shown: ^{56}Ni calculated using the same approach as Sukhbold et al. (2016), Ni from P-HOTB, Ni+Tr/2 from P-HOTB, Ni +Tr, and 0.75 times Ni+Tr+α from P-HOTB. The thin solid black line for Ni from P-HOTB represents the results shown by the red parts of the histogram bars in the third panel of Figure 5, and the thick dashed black line for Ni+Tr corresponds to the whole histogram bars in the same panel. The analysis of Sukhbold et al. (2016) gives values that we now believe are close to the minimum value, "Ni only" in the figure, but not far below the best estimate, Ni+Tr/2. The upper bound, 0.75 times Ni+Tr+α, is much larger than any of these and is probably a gross upper bound, though more extreme variations, probably not appropriate for a purely neutrino-powered explosion, are discussed in Section 8.5.

In neutrino-driven explosions, independent of the dimensionality of the modeling, the explosion energy, $E_{\rm exp}$, is provided by neutrino-heated matter that is expelled from the close vicinity or surface of the neutron star after having absorbed energy from neutrinos. Neutrino heating basically transfers the energy to lift this matter to a gravitationally marginally bound state, i.e., to specific energy $\epsilon_{\rm tot} = \epsilon_{\rm int} + \epsilon_{\rm grv} + \epsilon_{\rm kin} \lesssim 0$ (with $\epsilon_{\rm int}$, $\epsilon_{\rm grv}$, and $\epsilon_{\rm kin}$ being the specific internal, gravitational, and kinetic energies, respectively). The excess energy that fuels the supernova explosion mainly stems from nuclear recombination in the neutrino-heated matter as it expands and cools down from its initial conditions in NSE (see discussion in Appendix C of Scheck et al. 2006; see also Marek & Janka 2009; Müller 2015; Bruenn et al. 2016; Janka 2017). This leads to the simple relation (Scheck et al. 2006)

$$\frac{E_{\rm exp}}{10^{51}\,{\rm erg}} \approx \frac{M_{\rm rec}}{0.1\,M_\odot} \cdot \frac{\epsilon_{\rm rec}}{5\,{\rm MeV}}, \tag{9}$$

where $M_{\rm rec}$ is the neutrino-driven ejecta mass releasing the recombination energy, and $\epsilon_{\rm rec}$ is the mean recombination energy per nucleon. Typical values of $\epsilon_{\rm rec}$ are around 5–6 MeV. These are below the maximum value of 8.8 MeV set free when nucleons recombine to iron-group nuclei because recombination can be incomplete (producing α-particles). Moreover, some fraction of the released energy is usually still needed to overcome the gravitational binding energy of the ejected gas.

In our 1D simulations, neutrino-heated matter has Y_e values between ~0.45 and 0.49. Therefore, neutrons and protons present at NSE recombine to tracer (Tr) material and α-particles, depending on the entropy and expansion timescale of the ejecta, i.e., $M_{\rm rec} = M({\rm Tr}) + M(\alpha)$ (see Section 3.1). At conditions of $Y_e \gtrsim 0.5$, a significant mass fraction of ^{56}Ni would be assembled.

Because of Equation (9), the explosion energy correlates with $M_{\rm rec}$, and since the mass of explosively produced ^{56}Ni in the shock-heated progenitor layers with $Y_e = 0.5$ should also correlate with the explosion energy, we expect a strong correlation between $E_{\rm exp}$ and the summed masses of Ni+Tr+α. This correlation is visible in the top and bottom panels of the two plots in Figure 10 and even more tightly in the middle panels. In our simulations, the masses of ^{56}Ni and Tr are roughly equal (see Figure 9 and third panels of Figures 5 and 7). Since Ni is formed in nuclear reactions of oxygen and silicon, releasing only ~1 MeV per nucleon, its fusion contributes only a little to the explosion energy.

Note that in Figure 10, M(Ni+Tr+α) is measured before fallback, which means that it constitutes the mass of these nuclear species that contributes to the energy provided by the explosion mechanism through nuclear recombination and fusion. The total energy that the mechanism would have to make available to unbind the complete star and explode it with energy $E_{\rm exp}$ is denoted by $E_{\rm mech}$ in Figure 10. It is defined as

$$E_{\rm mech} = E_{\rm exp} - E_{\rm bind}(m > M^{\rm bfb}_{\rm b,NS};\, t_{\rm exp}), \tag{10}$$

where $E_{\rm bind}(m > M^{\rm bfb}_{\rm b,NS};\, t_{\rm exp})$ is the (negative) total energy (internal plus gravitational plus kinetic), measured at the time the explosion sets in, of all matter exterior to the baryonic mass of the neutron star before fallback. Consistent with our hydrodynamic modeling, we take general relativistic corrections into account in calculating the gravitational energy of all matter, $m > M^{\rm bfb}_{\rm b,NS}$. The bounding mass shell, $m = M^{\rm bfb}_{\rm b,NS}$, is

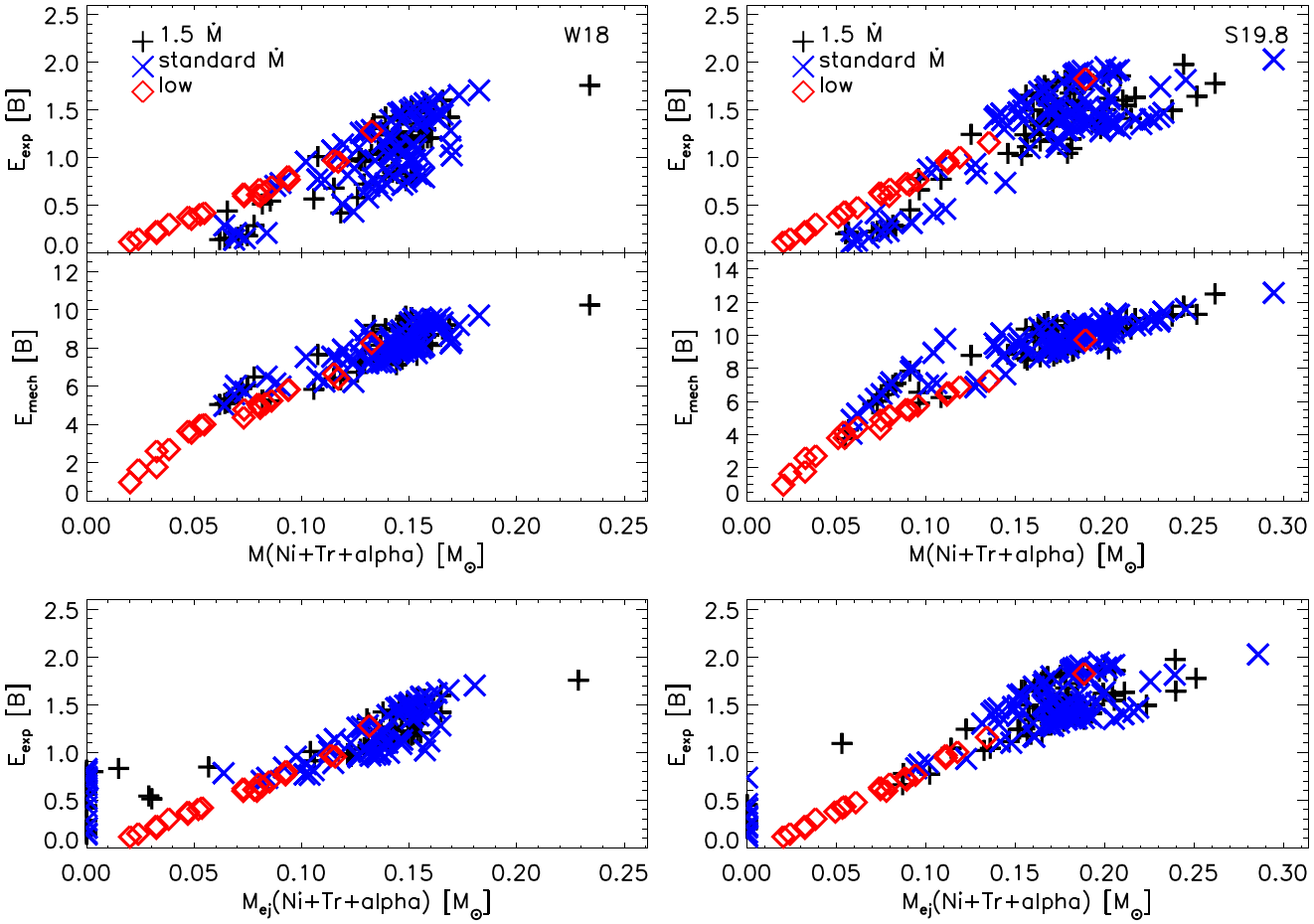

Figure 10. Correlations between the mass of Ni+Tr+α produced by the supernova explosion and the explosion energy, $E_{\rm exp}$ (top and bottom panels), as well as the energy $E_{\rm mech}$ that the neutrino-driven mechanism has to provide to lift the ejecta out of the gravitational potential of the neutron star and unbind the whole star with an energy of $E_{\rm exp}$ (for the exact definition, see Equation (10); middle panels). In the upper four panels, M(Ni+Tr+α) on the abscissa is the mass of these species before fallback; in the bottom two panels, $M_{\rm ej}$(Ni+Tr+α) is the corresponding mass corrected for fallback, i.e., the actually ejected mass of the three nuclei. The plots show P-HOTB simulations for all investigated helium star progenitors with the Z9.6 and W18 (left panels) and Z9.6 and S19.8 (right panels) neutrino engines.

located below the surface of the PNS at time $t_{\rm exp}$, and the overlying shells are blown out by neutrino heating in the neutrino-driven wind to deliver the energy to the explosion as described above. Therefore, $E_{\rm mech}$ is much larger than the final explosion energy $E_{\rm exp}$. On the one hand, this is so because $E_{\rm mech}$ includes the energy that the explosion mechanism has to spend on lifting the matter that contains M(Ni+Tr+α) out of the gravitational potential trough of the neutron star and unbinding all of the overlying stellar material ahead of the supernova shock. On the other hand, fallback removes some of the energy initially transferred to the transiently expanding stellar matter, which can lead to a reduction of $E_{\rm exp}$. Measuring $E_{\rm bind}(m > M_{\rm b,NS}^{\rm bfb}; t_{\rm exp})$ at $t_{\rm exp}$ is an approximation because the neutron star contracts with time and its surface layers become gravitationally more strongly bound as time goes on. However, our approximation yields a useful proxy because the neutrino-driven outflow is strongest in the phase when the explosion sets in and shortly afterward.

The correlation between $E_{\rm mech}$ and M(Ni+Tr+α) in the middle panels of Figure 10 is considerably tighter than between $E_{\rm exp}$ and M(Ni+Tr+α) in the top two panels. In the latter panels, the uppermost data points describe the relation of Equation (9) very closely. These are the normal explosions with very little fallback (typically much less than $\sim 10^{-2}\,M_\odot$; see Figures 6 and 8). The cases that lie well below this imagined correlation line in the top panels, while their correspondents in the middle panels are well integrated in the main data band, are supernova explosions with more significant fallback. In these cases, the binding energy of the collapsed stellar core is considerably larger, and a bigger fraction of $E_{\rm mech}$ is needed to lift the ejecta out of the gravitational potential trough. Therefore, the resulting explosion energies are noticeably lower than the typical values.

The cluster of data points below the main data band at M(Ni+Tr+α) between $\sim$0.05 and $\sim$0.10 $M_\odot$ in the top panels of Figure 10 is even more extreme. These are our cases of fallback supernovae with black hole formation caused by very large fallback masses as discussed above. They are characterized by collapsed stellar cores that possess particularly high binding energies because the explosion sets in very late and the neutron star is extremely massive and compact. These conditions permit only marginal explosions because (a) the binding energy in $E_{\rm mech}$ is much bigger than usual and (b) M(Ni+Tr+α) is rather low when the explosion starts late. Since the mechanism cannot provide the energy to unbind the whole star, massive fallback is the consequence, and $E_{\rm exp}$ becomes small. Therefore, the data

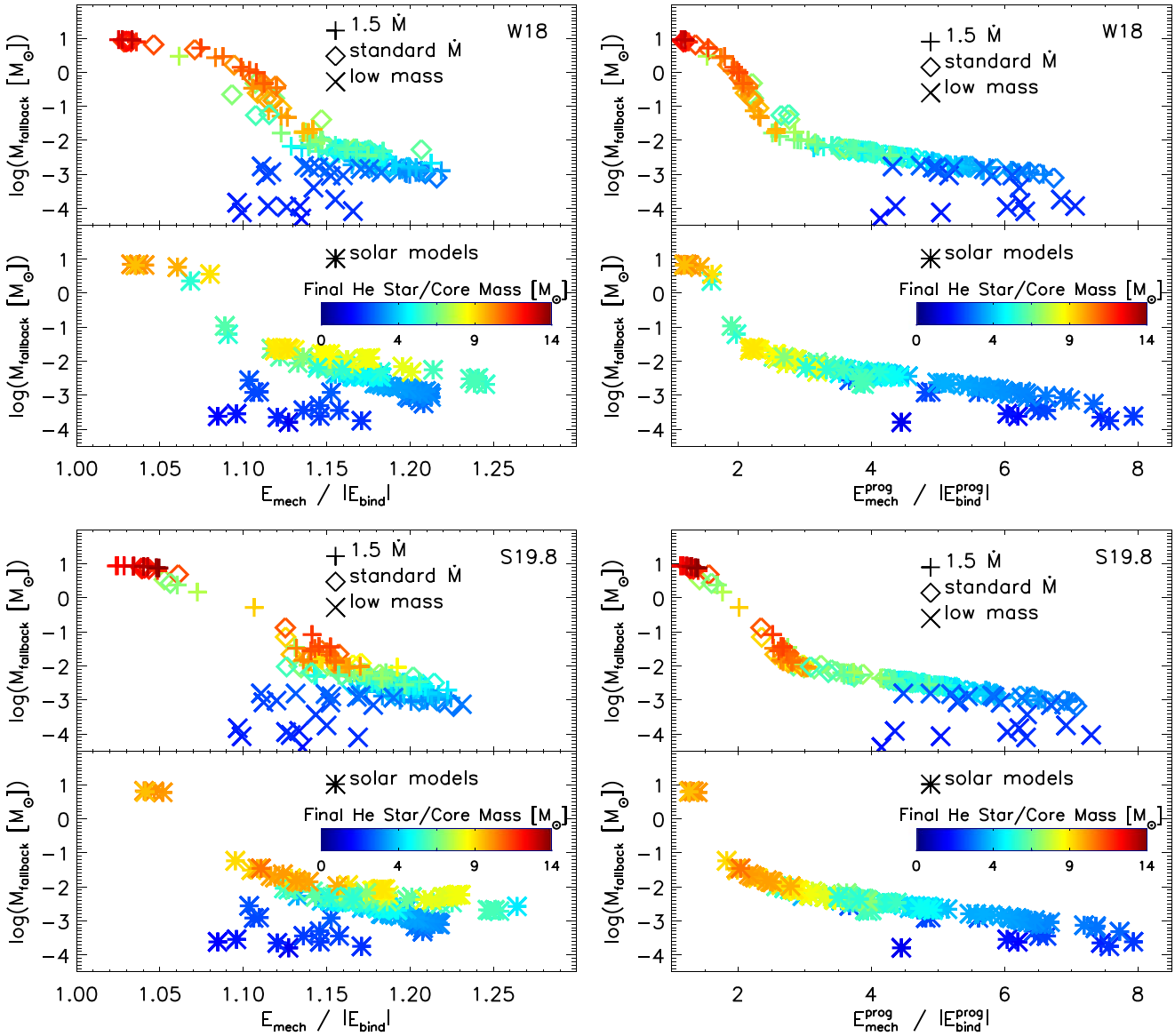

Figure 11. Left plots: fallback masses (log-scale) vs. ratio of $E_{\rm mech}$ (as defined in Equation (10)) to binding energy $|E_{\rm bind}|$ for all helium star progenitors (upper panels in all plots) and the single-star progenitors from Sukhbold et al. (2016; lower panels in all plots) that explode in P-HOTB simulations with the Z9.6 and W18 (top plots) or Z9.6 and S19.8 (bottom plots) neutrino engines. The ratio $E_{\rm mech}/|E_{\rm bind}|$ is computed for all mass outside of the initial mass cut ($m > M^{\rm bfb}_{\rm b,NS}$) in the profile of the collapsed star at time $t_{\rm exp}$ when the explosion sets in. Right plots: same as left plots but with $E^{\rm prog}_{\rm mech}/|E^{\rm prog}_{\rm bind}|$ evaluated for this mass range in the precollapse profiles of the progenitors. The color coding of the symbols in all panels corresponds to the final helium core masses.

points are located close to the bottom of the top panels in Figure 10.

Figure 10 demonstrates that the mass of Ni+Tr+α produced by neutrino-driven explosions is limited due to its correlation with the explosion energy. The latter is not found to exceed $\sim 2 \times 10^{51}$ erg even for our strongest neutrino engine, Z9.6 and S19.8 (see right plot in Figure 10). For this reason, we do not obtain an M(Ni+Tr+α) higher than $\sim 0.2\,M_\odot$. For the Z9.6 and W18 engine, the limit is even only around $\sim 0.15\,M_\odot$ (corresponding to an extreme upper bound on ^{56}Ni of $\sim 0.12\,M_\odot$, indicated by the red line in Figure 9). In most cases, fallback reduces the ejected mass of Ni+Tr+α, $M_{\rm ej}$(Ni+Tr+α), only slightly compared to the nucleosynthesized mass represented by M(Ni+Tr+α). However, the data points for the cases with more massive fallback are shifted considerably in the two bottom panels of Figure 10, where $M_{\rm ej}$(Ni+Tr+α) is plotted on the abscissa instead of M(Ni+Tr+α). This concerns most of the points with small explosion energies in the lower parts of the two top panels. They are moved closer to the correlation line describing Equation (9). This leads to a narrower band of data points in the bottom panels and a correlation similarly as tight as the one seen in the two middle panels. Outliers are only the (few) cases in which all or most of the nucleosynthesized Ni+Tr+α falls back. The corresponding data points cluster in the left part of the bottom panels, where the ejected mass $M_{\rm ej}$(Ni+Tr+α) is very small or zero. Since mixing is not included in our 1D simulations, it is unclear whether multidimensional effects during the long-time evolution of the supernova can change this result.

4.4. Fallback

In the new helium star models, a considerably larger number of cases show appreciable fallback than in our previous studies

of single stars (Ertl et al. 2016a; Sukhbold et al. 2016). This fallback results in neutron stars with high gravitational masses up to more than $2\,M_\odot$ and black holes with smaller gravitational masses between 2.3 and $6\,M_\odot$. Such cases were absent in our previous works on single-star explosions. Why?

Figure 11 compares the fallback conditions of the helium stars with the explosions of the single-star progenitors considered by Sukhbold et al. (2016). All simulations, including those of single stars, were calculated using the upgraded version of P-HOTB. As discussed in Section 4.3, large fallback often happens when a high energy, $E_{\rm mech}$ (see Equation (10)), is required in order to gravitationally unbind the whole star and provide an energy of $E_{\rm exp}$. This quantity can be used to measure the probability of massive fallback in the explosion. In the left panels of Figure 11, the fallback mass is displayed as a function of the ratio of $E_{\rm mech}$ to the absolute value of the total energy $E_{\rm bind}$ as used and defined in Equation (10). In the right panels of Figure 11, $E_{\rm mech}/|E_{\rm bind}|$ is replaced by the corresponding ratio of energies when the binding energy of the star is not computed from the structure at $t_{\rm exp}$ but from the precollapse profile of the star. This means that $E_{\rm bind}^{\rm prog}$ is the (negative) total energy of all progenitor shells above the initial mass cut, i.e., of all mass shells $m > M_{\rm b,NS}^{\rm bfb}$. With that, $E_{\rm mech}^{\rm prog} = E_{\rm exp} - E_{\rm bind}^{\rm prog}$. The upper panel of each plot shows the results for helium stars, and the lower panel shows single stars for comparison.

The figure shows, as expected, that massive fallback anticorrelates with these energy ratios. In all panels of Figure 11, there is a narrow main band that contains the majority of all data points. Outliers from this main band, where most of the models cluster, are only low-mass helium star and single-star progenitors that explode with very little fallback and are therefore located below the main band. For helium stars, fallback masses of more than about $0.1\,M_\odot$ become frequent when $E_{\rm mech}/|E_{\rm bind}| \lesssim 1.1$ or $E_{\rm mech}^{\rm prog}/|E_{\rm bind}^{\rm prog}| \lesssim 2.4$. This implies that in explosions with high fallback masses, the final explosion energy is less than ∼10% of the energy needed to gravitationally unbind the initial ejecta, or $E_{\rm exp}$ is less than 1.4 times the gravitational binding energy of the progenitor shells exterior to the initial mass cut. These values are lower for single-star progenitors, where $M_{\rm fallback} \gtrsim 0.1\ M_\odot$ for $E_{\rm mech}/|E_{\rm bind}| \lesssim 1.07$ or $E_{\rm mech}^{\rm prog}/|E_{\rm bind}^{\rm prog}| \lesssim 1.7$, which implies $E_{\rm exp} \lesssim 0.07\ |E_{\rm bind}|$ and $E_{\rm exp} \lesssim 0.7\ |E_{\rm bind}^{\rm prog}|$. Since $E_{\rm bind}$ is similar for single and helium stars, this means that the former explode less energetically when the fallback masses are $\gtrsim 0.1\,M_\odot$. This seems to be a consequence of the fact that there is not only a reverse shock from the C+O/He interface but also a second reverse shock from the interface between the helium core and the hydrogen envelope. Both together damp the supernova blast more strongly than just the reverse shock from the C+O/He interface.

Massive fallback occurs for helium stars with final helium star masses between ∼10 and $\sim 14\,M_\odot$, whereas in the set of single stars, only a few cases with final helium core masses around $10\,M_\odot$ show this behavior. There are two reasons for more fallback cases in our current P-HOTB simulations of helium stars. First, in the set of single-star progenitors used by Sukhbold et al. (2016), there were many fewer models with final helium core masses from 10.5 to $13\,M_\odot$, where both the helium stars and the single stars make fallback supernovae. Unfortunately, our model set of 2016 was sparse in exactly this region (see Table 2 in Sukhbold et al. 2016). Second, the

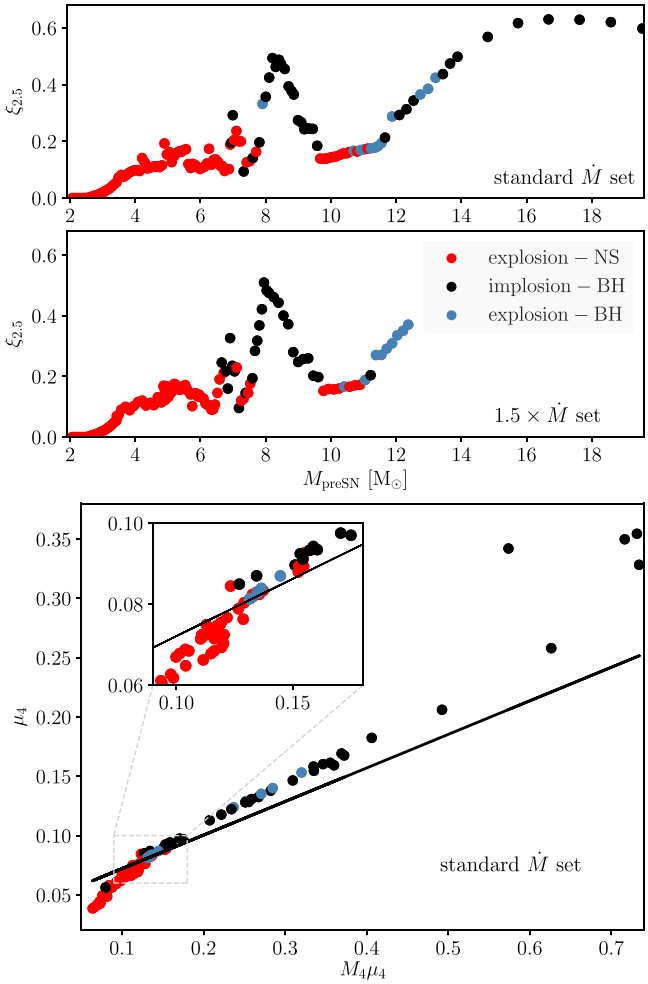

Figure 12. Top: compactness parameter (O'Connor & Ott 2011) characterizing the inner $2.5\,M_\odot$ of the presupernova star as a function of ZAMS mass for all helium star models. Bottom: Ertl parameterization (Ertl et al. 2016a) for the same sets of models. All panels display the color-coded outcomes of P-HOTB simulations with the W18 and Z9.6 neutrino engine.

helium stars have lower compactness values for precollapse helium star masses between ∼10 and $\sim 12\,M_\odot$, namely $\xi_{2.5} \approx 0.15$–0.2 (Figure 12, upper two panels), whereas the single stars possess $\xi_{2.5} \approx 0.2$–0.3. This favors direct black hole formation for single stars and more fallback supernovae for helium stars.

In the panels that show single-star results in Figure 11 for both neutrino engines (Z9.6 and W18 and Z9.6 and S19.8), one can see a corresponding gap of explosion cases around $E_{\rm mech}/|E_{\rm bind}| \sim 1.05$ and $E_{\rm mech}^{\rm prog}/|E_{\rm bind}^{\rm prog}| \sim 1.5$, which separates the few cases with the largest fallback from the continuum of data with fallback masses $M_{\rm fallback} \lesssim 0.1\ M_\odot$. For helium stars, such a gap is absent (for the Z9.6 and W18 engine) or much less pronounced (for the Z9.6 and S19.8 engine).

4.5. Comparison with Single-star Results

Figure 12 displays the core-collapse outcomes, i.e., supernova explosion and neutron star formation (red), explosion and black hole formation (blue), or collapse with black hole formation (black), for the Z9.6 and W18 neutrino engine, with a dependence on the compactness parameter $\xi_{2.5}$ as a function of the final helium star mass for both model sets with standard and enhanced mass loss (top panels; a similar pattern for single

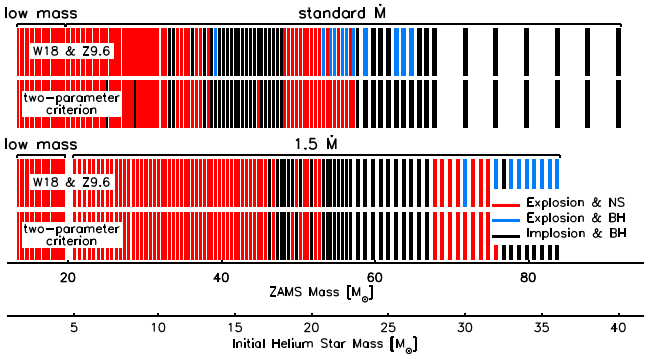

Figure 13. Core-collapse outcomes color-coded for the helium stars according to the Ertl parameterization (Figure 12, bottom panel; Ertl et al. 2016a), compared to results directly from P-HOTB simulations.

stars was found by Pejcha & Thompson 2015; Müller et al. 2016). In comparison, the bottom panel shows the separation of neutron star formation cases (red) from black hole formation cases (black and blue) by the Ertl et al. (2016a) two-parameter criterion for the same neutrino engine. Compactness values $\xi_{2.5} \lesssim 0.2$ favor explosions, compactness values above this threshold characterize mostly core collapse with black hole formation, but for values between 0.1 and 0.2, both outcomes are possible.

In contrast, the Ertl et al. (2016a) criterion separates neutron star formation (red) from black hole formation (blue and black) more reliably. This can be seen in Figure 13, where the patterns for direct simulation results with P-HOTB and core-collapse outcomes predicted by the Ertl et al. (2016a) criterion agree very well for helium stars with both standard and enhanced mass loss. Essentially, only fallback supernovae, which are weak explosions with high fallback masses and black hole formation, are hard to predict with the Ertl et al. (2016a) criterion.

Figure 14 compares the results for our current survey of mass-losing helium stars to our previous results (Sukhbold et al. 2016). The x-axis in each case is the presupernova mass for the helium stars or the mass of the helium and heavy-element core of the presupernova models for single stars. The mass ranges for the two are slightly different. Here it is assumed that helium stars below $2.50\,M_\odot$ (presupernova masses below $2.1\,M_\odot$) result in neon–oxygen white dwarfs. There could be a narrow range of electron-capture supernovae below this mass, but their existence and mass range are uncertain, and they are not included here. The single stars are bounded on the lower end by a ZAMS mass of $9.0\,M_\odot$ that has a helium core of $1.57\,M_\odot$ when the iron core collapses. This limit is also set by the neglect of electron-capture supernovae. The limits are the same in the sense that they are both the lightest models to experience iron core collapse. They are different because radius expansion in the helium star models is thought to lead to a second phase of binary mass transfer.

The models also differ at higher masses. Above about $35\,M_\odot$, the single stars lose their hydrogen envelope and experience WR mass loss, similar to the present models. But a different, larger mass-loss rate was used in 2016, so the final masses were smaller. For example, the presupernova mass for a $100\,M_\odot$ star in Sukhbold et al. (2016) was $6.04\,M_\odot$. Here it would be $22\,M_\odot$. Both stars collapsed to black holes with gravitational masses approximately equal to their presupernova masses.

Figure 14 shows a remarkable overall similarity between the earlier single-star results and the present study. To first order, it is the presupernova mass of the helium and heavy-element core (aka "the helium core") that determines its explosion energy, remnant mass, and ^{56}Ni nucleosynthesis. This has important implications. The minimum and maximum iron yields derived here probably characterize all massive stars, whether single or in binaries, even though the core masses at the time of collapse may have resulted from very different evolutionary paths and main-sequence masses.

In detail, however, they are different. The compactness of the core, however measured (Figure 12), is different in the two sets (Figure 14). This reflects the different entropy and composition of the two stars, one being derived from a helium core that lost mass—including, at the high end, most of its helium—and the other from a helium core that grew until the end. As noted by Woosley (2019), there is an offset in the mass giving rise to the first peak in compactness. For single stars, the peak is at about $8\,M_\odot$; for the present models, it is more like $9\,M_\odot$. This reflects in part the larger carbon abundance following helium depletion in the helium stars (Woosley 2019) and ultimately is a consequence of central carbon burning transitioning to the radiative regime at higher progenitor mass in the binary models (see Sukhbold & Adams 2020).

As a result, there is a gap in neutron star production around $8\,M_\odot$ in the old models that is shifted to $9\,M_\odot$ in the new ones.

5. Nucleosynthesis

Isotopic nucleosynthesis up to atomic mass number $A = 80$ was calculated using a large reaction network in the *KEPLER* code for all presupernova models, and explosive nucleosynthesis was calculated for all α-particle nuclei up to ^{56}Ni. These results and isotopic nucleosynthesis for the various central engines will be discussed elsewhere. Arguably though, the two most important nucleosynthetic products of core-collapse supernovae are oxygen and ^{56}Ni. Observers of SNe Ib and Ic frequently report averages of peak luminosities and attempt to extract average ^{56}Ni mass fractions (e.g., Lyman et al. 2016; Prentice et al. 2016). Oxygen is primarily made in massive stars. Observing the abundance ratio O/Fe in low-metallicity stars, presumably formed before SNe Ia contaminated the iron in the Sun, can thus constrain the amount of iron made as ^{56}Ni in earlier generations of massive stars. Magnesium, a representative "α-nucleus" made in massive stars, is also well studied in low-metallicity stars, and the Mg/Fe ratio can give similar constraints on iron production. It is thus useful to compute the IMF-weighted averages for the bulk yields for these three elements.

Table 2 gives the average explosion energies, ^{56}Ni yields, oxygen and magnesium yields, and explosion frequencies for two different central engines: W18, which is regarded as typical, and S19.8, which is more energetic. The explosion percentages ($f_{\rm SN}$) are the fractions of all star deaths that produced neutron stars and ejected ^{56}Ni. One minus that fraction is the percentage that made black holes and swallowed most of their ^{56}Ni. The actual supernova percentage would be slightly larger because some "successful" explosions made black holes by fallback, and their ^{56}Ni is assumed to reimplode. All averages were computed using a Salpeter IMF with $\alpha = -2.35$ (Salpeter 1955).

The ^{56}Ni yield in Table 2 is calculated in five different ways (Section 3.3 and Figure 9) that span the expected range of

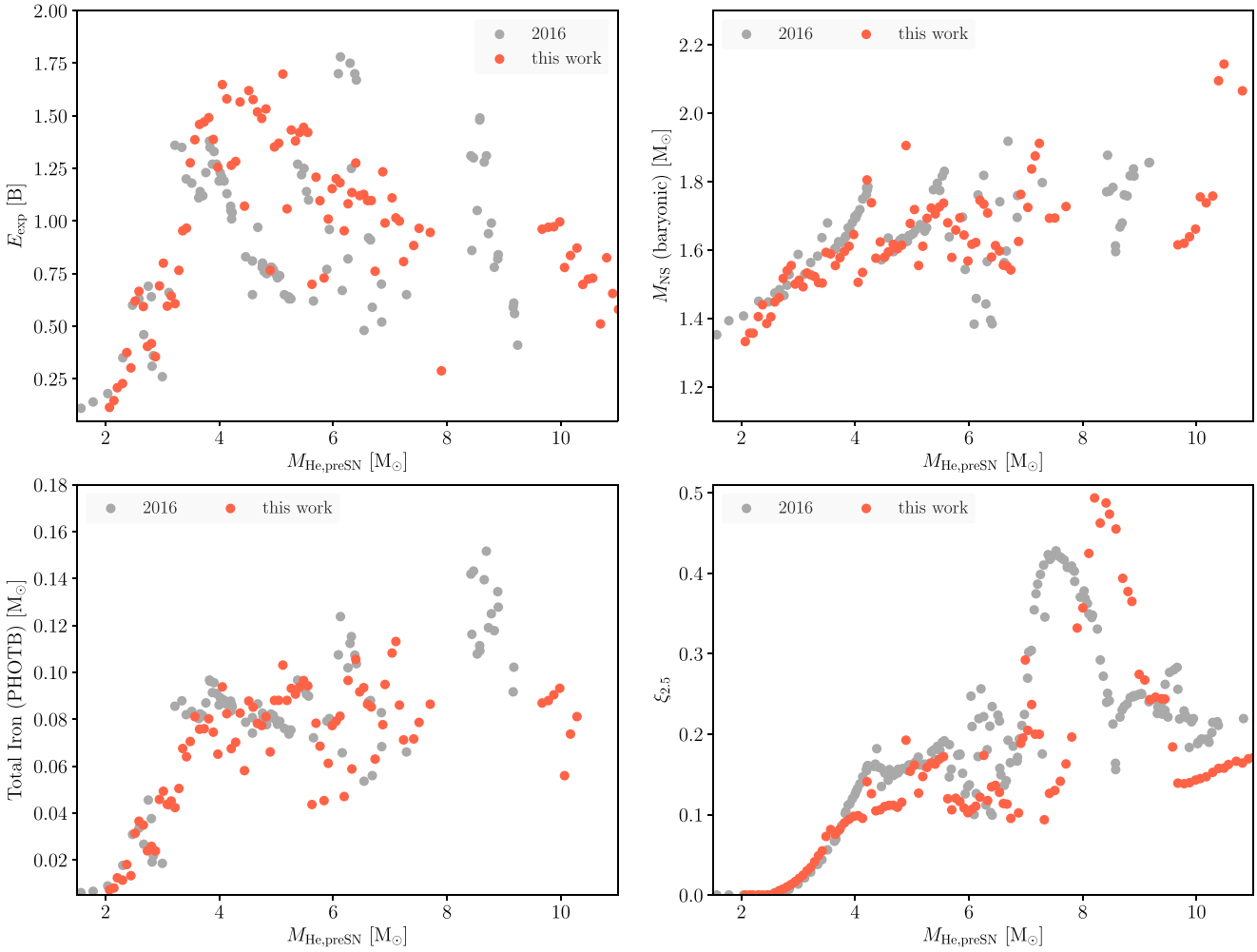

Figure 14. Comparison of current results for simulated binary evolution with those of Sukhbold et al. (2016) for single-star evolution.

minimum (Ni only) and maximum ($0.75 \times$ (Ni+Tr+α)) yields. The most likely value is between Ni+Tr/2 and Ni +Tr from the P-HOTB simulations. Also given for comparison are the yields calculated using the special trajectory in *KEPLER* as in Sukhbold et al. (2016). The oxygen and magnesium yields include contributions from the winds of all stars, even those whose cores later collapsed to black holes. On the other hand, ^{56}Ni comes only from supernovae that make neutron stars. Because of its relevance to the light curve, ^{56}Ni production is expressed as an average *per supernova*, but because they are made by every massive star, oxygen and magnesium yields are expressed per massive star death (or, equivalently, per massive star birth). The ^{56}Ni yield per star death is the yield per supernova times the fraction of supernovae, f_{SN}. It is important when comparing yields that all productions be normalized to the same event (per star death or per supernova). It is the total production of each in a generation of massive stars that matters.

For the standard W18 engine, the average ^{56}Ni yield is between 0.029 and 0.073 $M_\odot$, with a most likely value between 0.041 and 0.053 $M_\odot$. These relatively small numbers are influenced by a large number of low-mass, low-yield supernovae with initial helium star masses between 2.5 and 3 $M_\odot$. If one examines only the mass range 5–8 $M_\odot$ (presupernova masses 3.82–5.64 $M_\odot$) where most SNe Ib and Ic originate (Section 8.3), the range of ^{56}Ni yields becomes 0.040–0.11 $M_\odot$ with a typical value of 0.061–0.081 $M_\odot$. For the more energetic S19.8 engine, the values are slightly larger. The range for all masses rises to 0.036–0.090 $M_\odot$ with a typical value of 0.052–0.068 $M_\odot$. In summary, the favored ^{56}Ni production overall is around 0.04–0.06 $M_\odot$ per supernova with an upper bound about twice that. For the heaviest SNe Ib and Ic, the average is probably between 0.06 and 0.11 $M_\odot$.

The oxygen and magnesium yields have their own uncertainties. A larger WR mass-loss rate would increase their production in stars that make black holes. Changes in ^{12}C(α, γ)^{16}O and the treatment of convection will also change their yield. Examples using the current physics are presented to illustrate a constraint but are not precise. It is also assumed that these averages characterize the deaths of all massive stars of all metallicities, not just the solar-metallicity binaries simulated here. Oxygen and magnesium are primary elements, and their nucleosynthesis in supernovae is not so sensitive to metallicity, though variations in the winds are expected. The averages in Table 2 are very similar to those obtained by Sukhbold et al. (2016) for single stars, and the comparison is discussed further in Section 4.5.

Adopting iron and oxygen mass fractions in the Sun of 1.37×10^{-3} and 6.60×10^{-3}, respectively (Lodders 2003), the mass ratio of oxygen to iron in the Sun is 4.8. Taking 0.840 $M_\odot$ for the mean oxygen yield per star death and 0.053 $M_\odot$ per supernova for ^{56}Ni+Tr from W18 and multiplying the latter by the frequency of supernovae, 0.79, gives a ratio of

Table 2
Average Nickel, Oxygen, and Magnesium Yields

		E_{exp} (B)	Ni_{min} ($M_\odot$)	Ni + Tr/2 ($M_\odot$)	Ni + Tr ($M_\odot$)	Ni_{max} ($M_\odot$)	Ni (2016) ($M_\odot$)	O ($M_\odot$)	Mg ($M_\odot$)	f_{SN}
					Overall					
W18	Median	0.753	0.028	0.042	0.054	0.069	0.036	0.382	0.050	0.79
	Mean	0.832	0.029	0.041	0.053	0.073	0.035	0.840	0.078	
S19.8	Median	0.966	0.031	0.051	0.070	0.097		0.474	0.069	0.83
	Mean	1.015	0.036	0.052	0.068	0.090		1.096	0.090	
					$5 > M_{He,i} \geqslant 3$					
W18	Median	0.628	0.026	0.034	0.042	0.059	0.036	0.236	0.040	1.00
	Mean	0.738	0.023	0.034	0.044	0.064	0.032	0.268	0.052	
S19.8	Median	0.680	0.025	0.032	0.041	0.059		0.235	0.040	1.00
	Mean	0.833	0.025	0.037	0.049	0.071		0.270	0.053	
					$8 > M_{He,i} \geqslant 5$					
W18	Median	1.429	0.037	0.058	0.081	0.113	0.042	0.972	0.149	1.00
	Mean	1.408	0.040	0.061	0.081	0.110	0.045	0.985	0.141	
S19.8	Median	1.782	0.038	0.069	0.100	0.136		0.971	0.148	1.00
	Mean	1.719	0.045	0.071	0.097	0.130		0.986	0.141	
					$M_{He,i} \geqslant 8$					
W18	Median	0.969	0.050	0.064	0.079	0.100	0.058	1.367	0.056	0.40
	Mean	0.900	0.052	0.066	0.080	0.095	0.060	1.566	0.094	
S19.8	Median	1.363	0.066	0.087	0.109	0.130		1.953	0.117	0.54
	Mean	1.190	0.067	0.089	0.112	0.130		2.282	0.125	
				Per Supernova				Per Death		

Note. Here Ni_{min} is ^{56}Ni calculated by P-HOTB ignoring Tr and α, and Ni_{max} is 0.75 × (Ni+Tr+α). See Section 3.3 and Figure 9.

20, implying that core-collapse supernovae make 4.8/20 = 24%, by mass, of the iron in the Sun. Using Ni+Tr/2 gives 19%, perhaps on the low side. Observationally, the fraction of iron from core-collapse supernovae, based on measurements of O/Fe or α/Fe (where α may be Mg, Si, S, Ca, or Ti), is usually thought to be about 1/4–1/3 (e.g., Fulbright et al. 2007; Barbuy et al. 2018; Amarsi et al. 2019), though some recent observations suggest it may be as large as 50% (Griffith et al. 2019). Taking 0.073 for 0.75 × (Ni+Tr+a) increases the maximum average ^{56}Ni production for W18 and raises the fraction to 33%, which is also acceptable. Using the more energetic explosion, S19.8, and taking the high ^{56}Ni yield, however, raises the fraction to 42%. Even given the considerable uncertainty in oxygen production in winds and abundances in metal-poor stars, much larger average ^{56}Ni production than this may cause difficulty for models of galactic chemical evolution.

Similar restrictions come from considering magnesium. The mass fraction of Mg in the Sun is 6.6×10^{-4} (Lodders 2003), all of which is believed to be made in core-collapse supernovae and WR winds. Taking a typical synthesis of 0.078 $M_\odot$ from Table 2 and using the Ni+Tr value for iron, 0.053 $M_\odot$ implies that 27% of solar iron is made in the current calculations (and presumably core-collapse supernovae in general). Raising that value by a factor of 2 would also conflict with measurements of the Mg/Fe ratio in low-metallicity stars (Weinberg et al. 2019).

The implication is that the ^{56}Ni abundances used in our brightest standard light-curve calculations (Section 8; Figures 23 and 26) are probably close to the largest values allowed by galactic chemical evolution. Greater oxygen-to-iron yields in low-metallicity stars than calculated here for solar metallicity or a greater production of oxygen and magnesium in the winds of WR stars, possibly because of a larger mass-loss rate, would help ease this restriction. Conversely, less mass loss in metal-poor stars would make it worse. Further work is needed.

The average ^{56}Ni yields for the most optimistic models are also in conflict with observations of SN 1987A. The presupernova helium core mass for SN 1987A was 5–7 $M_\odot$ (Utrobin et al. 2015; Sukhbold et al. 2016), corresponding to initial helium core masses in the range 7–11 $M_\odot$ in Table 2. Adopting a value for the yield of ^{56}Ni of 0.75 × (Ni+Tr+α) implies that the average ^{56}Ni production for the W18 or S19.8 central engines would be 0.11–0.13 $M_\odot$. This is much larger than the 0.07 $M_\odot$ observed for SN 1987A (Suntzeff et al. 1992). These are average productions, and there are individual models in this mass range that make substantially less ^{56}Ni than the mean, some even as low as 0.07 $M_\odot$, but they are rare and have explosion energies considerably less than observed in SN 1987A, about 1.5×10^{51} erg. This energy is also needed to explain the maximum velocities above 3500 km s^{-1} observed for nickel in SN 1987A (Utrobin et al. 2015, 2019).

6. Bound Remnants

Tables 3 and 4 give the IMF-averaged masses for neutron stars and black holes produced in this study. Both sets of masses are given before and after corrections for neutrino losses during their formation. Baryonic masses are determined by the final mass cut in the P-HOTB explosion. Gravitational masses for neutron stars have been calculated in two different ways (Section 4.2). In the standard case, the total neutrino losses calculated for the explosion by P-HOTB divided by c^2 are subtracted from the baryonic mass and a further correction for late-time fallback accretion. For comparison, the gravitational mass computed for the cold neutron star using the analytic formula of Lattimer & Prakash (2001) is also given for an assumed neutron star radius of 12 km. The two numbers differ slightly because of different assumptions regarding the EOS. The gravitational masses of black holes are also corrected

Table 3
Average Neutron Star Masses

		$M_{\rm NS,b}$ ($M_\odot$)	$M_{\rm NS,g}$ ($M_\odot$)	$M_{\rm NS,g,PL01}$ ($M_\odot$)	$M_{\rm NS,b}$ ($M_\odot$)	$M_{\rm NS,g,PL01}$ ($M_\odot$)	$M_{\rm NS,b}$ ($M_\odot$)	$M_{\rm NS,g,PL01}$ ($M_\odot$)
		P-HOTB			Fe Core		(2016)	
		Overall						
W18	Median	1.531	1.351	1.378	1.396	1.267	1.555	1.397
	Mean	1.554	1.371	1.397	1.415	1.283	1.588	1.424
S19.8	Median	1.514	1.335	1.364	1.407	1.277	1.563	1.404
	Mean	1.534	1.349	1.380	1.428	1.294	1.571	1.410
		$5 > M_{\rm He,i} \geqslant 3$						
W18	Median	1.510	1.337	1.361	1.367	1.243	1.537	1.383
	Mean	1.502	1.333	1.354	1.379	1.253	1.530	1.377
S19.8	Median	1.492	1.319	1.346	1.367	1.243	1.524	1.372
	Mean	1.488	1.318	1.343	1.379	1.253	1.520	1.369
		$8 > M_{\rm He,i} \geqslant 5$						
W18	Median	1.611	1.406	1.443	1.513	1.363	1.661	1.483
	Mean	1.646	1.433	1.471	1.511	1.362	1.694	1.509
S19.8	Median	1.585	1.375	1.422	1.513	1.363	1.647	1.471
	Mean	1.611	1.394	1.443	1.511	1.362	1.670	1.490
		$M_{\rm He,i} \geqslant 8$						
W18	Median	1.669	1.457	1.489	1.431	1.296	1.706	1.518
	Mean	1.726	1.486	1.534	1.466	1.325	1.760	1.561
S19.8	Median	1.636	1.414	1.463	1.469	1.327	1.688	1.504
	Mean	1.654	1.427	1.477	1.497	1.350	1.698	1.512

Note. The P-HOTB gravitational mass, $M_{\rm NS,g}$, is computed by tracking the radiated neutrino energies and a correction for late-time fallback accretion (see Section 4.2), while the $M_{\rm NS,g,LP01}$ values were computed only through the equations from Lattimer & Prakash (2001).

Table 4
Average Black Hole Masses

		$M_{\rm BH,b}$ ($M_\odot$)	$M_{\rm BH,g}$ ($M_\odot$)
	$90 > M_{\rm He,i} \geqslant 8$		
W18	Median	11.42	10.88
	Mean	14.81	14.44
S19.8	Median	10.96	10.49
	Mean	16.36	16.10
	$40 > M_{\rm He,i} \geqslant 8$		
W18	Median	8.96	8.61
	Mean	10.39	10.14
S19.8	Median	10.07	9.65
	Mean	10.79	10.42

Note. See Section 6.2 for details.

for the neutrino emission that occurs during their formation (Section 4.2).

In Tables 3 and 4, entries are given for both the median and mean masses. The median is that mass above and below which equal numbers of remnants are expected. This is the most relevant quantity for observations. The mean mass is the IMF-weighted average total mass (neutron star or black hole) divided by the number of remnants. It is thus weighted toward heavier masses. Separate sets of numbers are given for the W18 and S19.8 central engines. In this paper, W18 is the standard engine, and S19.8 is an upper bound to the explosion energy. As expected, average neutron star masses are larger for the less energetic explosions for the self-consistent calculations using P-HOTB. The black hole mass averages do not always follow such a simple expectation. While a larger explosion energy reduces the amount of fallback, it also results in stars exploding that might have become black holes. There are fewer low-mass black holes, while the heavy ones continue to implode. Though not given in the tables, average remnant masses for the other central engines, N20, W15, and W20, were also calculated and were similar.

6.1. Neutron Stars

Of the many values in Table 3, we suggest the range 1.35–1.38 $M_\odot$ as the most appropriate for the median gravitational mass of neutron stars in close binary systems. This is the range of results for the median value using the W18 central engine and either the P-HOTB or Lattimer and Prakash corrections to the baryonic mass. It is the average for systems of all initial masses. The table also gives the partition of this overall average into intervals of initial helium star mass: 3–5, 5–8, and >8 $M_\odot$. As expected, the average increases with progenitor mass as the core structure becomes less centrally condensed (Figure 15). The weighted birth function for neutron stars is given as a function of their gravitational mass in Figure 16. The mean mass (as opposed to median mass) overall is 1.37–1.40 $M_\odot$ with a standard deviation of 0.11 $M_\odot$.

The lightest neutron star in the standard (W18) set has a baryonic mass of 1.332 $M_\odot$, corresponding to a gravitational mass of 1.239 $M_\odot$ using the P-HOTB correction for neutrino losses (Section 4.2). If one uses the Lattimer & Prakash (2001) approximation instead, the gravitational mass is 1.214 $M_\odot$ for an assumed radius of 12 km and 1.205 $M_\odot$ for a radius of 11 km. Looking at all possible central engines, the overall minimum is for the 2.50 $M_\odot$ helium star using the W20 central engine. This combination gives a gravitational mass of 1.238 $M_\odot$ using the P-HOTB correction and 1.214 $M_\odot$ (1.204 $M_\odot$) using the Lattimer & Prakash (2001) approximation and an assumed radius of 12 km (11 km). Slightly smaller values are, in principle, possible using an artificial mass separation. For the 2.70 $M_\odot$ helium star and W20 central engine, the iron core is 1.288 $M_\odot$, and the equivalent

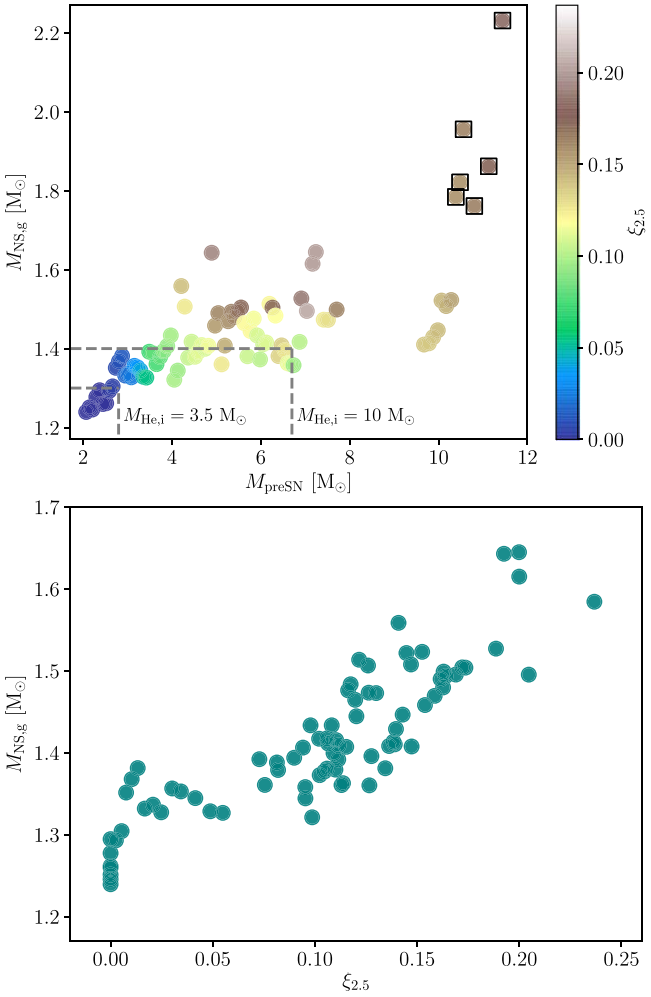

Figure 15. Neutron star mass systematics for the W18 central engine. Top: gravitational mass as a function of the presupernova mass ($M_{\rm He,final}$). Dashed boxes show that all neutron stars lighter than 1.30 $M_\odot$ come from helium stars with initial masses less than 3.5 $M_\odot$, while those lighter than 1.40 $M_\odot$ come from helium stars less than 10 $M_\odot$. The masses are color-coded according to the compactness parameter, $\xi_{2.5}$, showing that less massive neutron stars come from progenitors with sharp density declines outside their iron cores. Note a gap in the mass distribution for $M_{\rm He,fin}$ from 8 to 9 $M_\odot$ corresponding to a local maximum in compactness (Figure 12). The most massive neutron stars that experienced significant fallback (>0.1 $M_\odot$), which come from the most massive progenitors, are highlighted with black boxes. Bottom: the neutron star masses (excluding those that experienced significant fallback) are highly correlated with the compactness of the presupernova star. For $\xi_{2.5}$ smaller than 0.05, the baryonic remnant mass is essentially the cold Chandrasekhar mass of the presupernova core. As the entropy increases, the compactness parameter rises, and so does the neutron star mass.

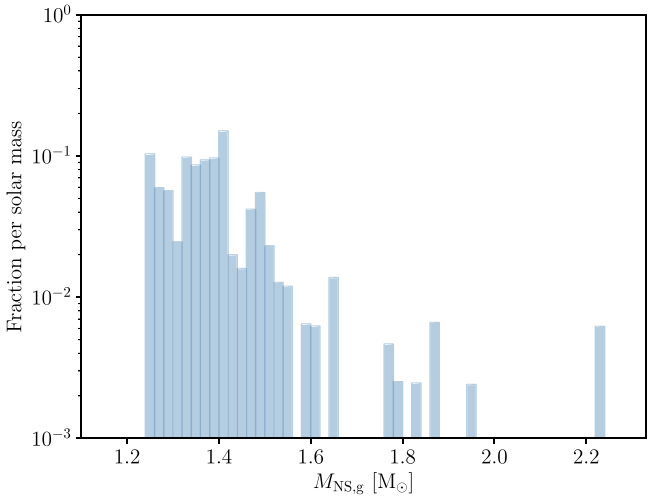

Figure 16. Neutron star gravitational mass result for the W18 central engine. The average mass is 1.371 $M_\odot$; the median is 1.351 $M_\odot$. The probability has been normalized so that the integral under the curve is 1. A few neutron stars at high mass result from fallback.

gravitational mass is 1.181 $M_\odot$ (1.167–1.178 $M_\odot$ for the Lattimer–Prakash mass with a radius of 12 or 11 km). This is unrealistically small, since mass separations this deep are not found in modern models. We conclude that a gravitational mass of 1.24 $M_\odot$ is a reasonable lower bound for our models, and 1.20 $M_\odot$ is the boundary of what might be reasonable with the physics employed in this study. Less massive neutron stars would require special conditions for their creation.

The most massive neutron star comes from the theoretical upper limit, taken here to be about 2.25 $M_\odot$ (Section 4). Thus, model He22.50 produces a neutron star with gravitational mass 2.23 $M_\odot$, while model He22.00 makes a black hole with mass 2.29 $M_\odot$. This continuum of masses is due to the action of fallback after the explosion, and low-mass black holes, while rare, should exist, as should a smattering of neutron stars up to the maximum mass. All neutron stars with gravitational mass over 1.65 $M_\odot$ come from helium stars over 20.0 $M_\odot$. All neutron stars with masses below 1.40 $M_\odot$ come from helium stars lighter than 10 $M_\odot$, as do a lot of more massive neutron stars. All neutron stars less massive than 1.30 $M_\odot$ come from helium stars less than 3.5 $M_\odot$ (Figure 15). Neutron stars between 1.24 and 1.7 $M_\odot$ are formed promptly in the explosion, but heavier neutron stars are produced by fallback (e.g., the six most massive points in Figure 15).

Figure 16 also suggests that the neutron star birth function has structure with a hint of peaks around 1.35 and 1.5 $M_\odot$. A larger set of models that explores variable metallicity, mass loss, explosion characterization, and binary parameters will be needed before this structure is statistically significant, but an exciting prospect is that the neutron star mass function reflects the nonmonotonic nature of the compactness parameter (Figure 12), which, in turn, is sensitive to the location of critical shell-burning episodes in the presupernova star.

The values derived here for median masses (1.35–1.38 $M_\odot$ favored) are in good agreement with those determined from observations. Lattimer (2012) gave an (error-weighted) observational mean of 1.368 $M_\odot$ for X-ray and optical binaries, 1.402 $M_\odot$ for neutron star binaries, and 1.369 $M_\odot$ for neutron star–white dwarf binaries. These are not far from the average neutron star mass found by Schwab et al. (2010), 1.325 ± 0.056 $M_\odot$.

Özel & Freire (2016) gave the range of accurately determined neutron star masses in 2016 as 1.17–2.0 $M_\odot$. Our calculated range, 1.24–2.25 $M_\odot$, is in reasonable agreement. As already remarked, a 1.17 $M_\odot$ neutron star may be difficult to produce. They also gave 1.33 $M_\odot$ with a dispersion of 0.09 $M_\odot$ as the average for double neutron stars; 1.54 $M_\odot$ with a dispersion of 0.23 $M_\odot$ for the recycled neutron stars; and 1.49 $M_\odot$ with a dispersion of 0.19 $M_\odot$ for the slow pulsars. A recent study by Antoniadis et al. (2016) raised the possibility of two peaks (see also Valentim et al. 2011) within the recycled millisecond pulsar population, with the first peak at 1.388 $M_\odot$ with a dispersion of 0.058 $M_\odot$ and the second peak at 1.814 with a dispersion of 0.152 $M_\odot$ (see single-star comparison in Raithel et al. 2018).

Also given in Table 3 are the neutron star masses resulting from taking the mass separation to arbitrarily occur at the edge of the iron core. This gives a lower limit neutron star mass and a maximum production of ^{56}Ni that is of interest for the light curve. These masses are consistently small compared with the observations, suggesting that such a deep mass cut is, on average, probably not realistic.

The neutron star masses based on the same approach as in Sukhbold et al. (2016) are also given for comparison. Since the "special trajectory" (Section 3.2) is more shallow, the neutron star masses are slightly higher.

6.2. Black Holes

Stellar collapses that fail to create a strong outward moving shock before 10 s in P-HOTB are assumed to form black holes. While Woosley (2019) gave results for helium cores up to 120 $M_\odot$ (presupernova masses up to 60 $M_\odot$), only those that had a reasonable likelihood of leaving a neutron star were followed with P-HOTB. It is expected that for helium stars of up to 60 $M_\odot$ (presupernova up to 30 $M_\odot$), the presupernova mass will collapse to a black hole with little mass ejection. For helium cores of 60–70 $M_\odot$ (presupernova 30–35 $M_\odot$), a mild pulsational instability is encountered that does not greatly affect the mass of the star when its iron core collapses. To good approximation, these stars also make black holes with masses equal to their presupernova mass. For helium stars initially above 70 $M_\odot$, the pair instability becomes an important consideration. As far as remnant masses go, the chief effect of the pair instability is to reduce the mass of the remnant. Woosley (2019) derived an upper limit to black hole masses coming from pulsational pair instability supernovae of 46 $M_\odot$. To good approximation, the black hole mass for masses bigger than 20 $M_\odot$ for the assumed mass-loss rate is given by

$$M_{\rm BH} = 0.463 M_{\rm He,i} + 1.49\ {\rm M}_\odot, \quad (11)$$

where $M_{\rm He,i}$ is the initial mass of the helium star, and

$$M_{\rm BH} = 0.232 M_{\rm ZAMS} - 1.23\ {\rm M}_\odot, \quad (12)$$

where $M_{\rm ZAMS}$ is the main-sequence mass of the star.

Figure 17 shows the resulting IMF-weighted birth function for black holes using the P-HOTB results and an extrapolation from 19 to 46 $M_\odot$ using the above equations (Woosley 2019). A more thorough study that explicitly includes the pulsational pair-instability supernovae results is planned.

The smaller-mass black holes are made by fallback after the initial launch of a successful shock. The lowest-mass black holes made in any models for the W18 central engine were 2.29, 2.31, and 2.56 $M_\odot$, which came from stars with initial helium star masses of 22.0, 21.25, and 22.25 $M_\odot$, respectively. The presupernova masses of these systems were 11.23, 10.91, and 11.34 $M_\odot$, respectively, so most of the mass was ejected in the explosion. There is no low-mass "gap" in the black hole mass distribution in the present study. Fallback produces a continuous spectrum of masses from the heaviest neutron stars to the lightest black holes. These low-mass black holes are rare, however, compared with their higher-mass counterparts.

The smallest black hole to be made directly in a failed explosion with no outgoing shock has a baryonic mass of 6.95 $M_\odot$ and a gravitational mass of 6.42 $M_\odot$. The low-mass peak in the birth function (Figure 17) below ~6 $M_\odot$ is due to fallback; the remainder is mostly black holes produced by the direct implosion of the progenitor star. From 5 to 15 $M_\odot$, the

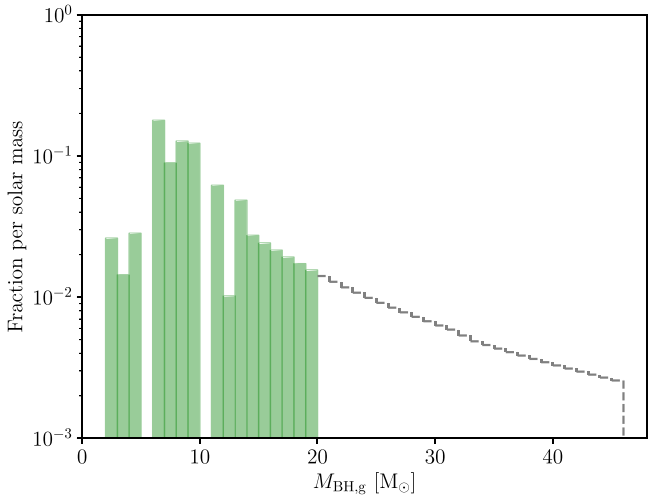

Figure 17. Black hole mass distribution result for the W18 central engine. The average black hole mass in the mass range studied (up to an initial helium star mass of 40 $M_\odot$) is 10.39 $M_\odot$, and the median gravitational mass is 8.61 $M_\odot$. Note the existence of a dip in production around 10 $M_\odot$ resulting from the island of explodability in Figure 5. The prominence of this feature depends on the central engine employed.

distribution shows structure correlated with the compactness of the presupernova stellar core (Figure 12). A pronounced minimum at ~10 $M_\odot$ results from the island of explodability near that mass. This suppression of black hole formation is robust for different choices of central engine, though its location may vary depending on the details of the presupernova model, especially the rate for ^{12}C(α, γ)^{16}O and convection physics. It should be a target of future gravitational wave surveys.

Table 4 gives the average properties of the distribution. Black holes are produced by 21% of all models. The median gravitational mass (after all neutrino losses) for the W18 central engine when all black holes up to 46 $M_\odot$ are included is 10.88 $M_\odot$. This is influenced by the extrapolation of the birth function from 20 to 46 $M_\odot$ in Figure 17 and is probably an overestimate. If only helium stars up to 40 $M_\odot$ (main-sequence masses up to 80 $M_\odot$) are considered, the median is 8.96 $M_\odot$. Both the IMF for stars above 80 $M_\odot$ on the main sequence and their mass-loss history, especially as luminous blue variables, are poorly known. A higher mass-loss rate would act to suppress the high-mass tail in Figure 17. Neither the median nor mean is a well-defined characteristic of the structure seen in Figure 17, especially if it is bimodal. There may not even be any black holes with masses near 10 $M_\odot$. Using a more energetic central engine, S19.8, actually increases the median value because more of the lower-mass models explode while the robustly collapsing massive models remain unchanged.

Given these uncertainties, our results compare favorably with black hole masses observed in X-ray binaries. Özel et al. (2010) gave a mean mass of 7.8 ± 1.2 $M_\odot$. The observed mean is consistent, but the narrow distribution is not. Farr et al. (2011) gave a lower limit at the 99% confidence level of about 4.5 $M_\odot$. This is inconsistent with the presence of a substantial number of less massive black holes in our results (Figure 17). These black holes are all made by fallback, though, and their masses are uncertain. On the other hand, Kreidberg et al. (2012) pointed out that errors in the inclination angle may have led to the overestimate of black hole masses in the gap and that black holes may exist all the way down to the maximum neutron star mass, as our analysis suggests. Their analysis also

suggests a peak around 7–8 $M_\odot$ and a sharp drop-off above 10 $M_\odot$. Figure 17 shows such a peak and a falloff, but the production remains substantial at higher masses. As remarked earlier, the abundance of such very massive black holes is sensitive to the treatment of mass loss and the IMF. All models with presupernova masses over 12 $M_\odot$ collapse directly to black holes. The issue is only how many such presupernova stars there are.

Fryer et al. (2012) also explored the black hole birth function using a different approach to modeling the explosion and found results that were sensitive to the mass loss. For solar metallicity, they found a maximum black hole mass around 10 $M_\odot$ when using presupernova models from Woosley et al. (2002), which had a larger mass-loss rate than the present study (see their Figure 9). On the other hand, using presupernova models from Limongi & Chieffi (2006) that employed a smaller mass-loss rate gave larger black hole masses. Clearly, an accurate birth function will require careful consideration of the effects of metallicity and mass loss. For now, we note that the outcome—explosion or collapse—and the mass of the collapsing object are mainly determined by the presupernova mass. It is thus feasible to estimate the black hole birth function to good accuracy from any choice of IMF, metallicity, mass-loss rate, binary parameters, etc. simply from an estimate of the masses of the stars at carbon ignition and the results shown in Figures 5–8.

For the models presented here (solar metallicity, W18 central engine, standard mass loss), 21% made black holes. This includes all stars with final masses above about 12 $M_\odot$ (initial helium star mass 25 $M_\odot$). This is substantially less than the 33% that make black holes in single stars for the same central engine (Table 6 of Sukhbold et al. 2016). This reflects both the smaller presupernova masses for stars of a given main-sequence mass when evolved in a mass-exchanging binary and their smaller compactness parameters (Figure 10 of Woosley 2019).

Since all presupernova stars with masses above 12 $M_\odot$ collapse, there is a maximum luminosity of any SN Ib or Ic progenitor, $10^{5.6}\,L_\odot$. The equivalent value for single stars is $10^{5.3}\,L_\odot$ or a birth mass of about 23 $M_\odot$ (Sukhbold et al. 2018), though the current observational limit is $10^{5.1}\,L_\odot$ or a birth mass of about 18 $M_\odot$ (Smartt 2009, 2015).

7. Light Curves—Code Physics

The *KEPLER* code incorporates flux-limited radiative diffusion and thus is capable of calculating approximate bolometric light curves for supernovae of all types. Calculating light curves for supernovae that have been stripped of their low-density hydrogen envelopes is more challenging than for SNe IIp, where hydrogen recombination plays a dominant role. The peak brightness depends sensitively on the amount of ^{56}Ni created in the explosion. Line opacity is more important; just carrying electron scattering is inadequate. The light curve and especially the spectrum are more sensitive to the degree to which that nickel has been mixed through the ejecta, and the opacity can be highly variable with both time and location. Within its limitations—1D, single temperature, no atomic line physics—*KEPLER* reasonably depicts the qualitative light curves of supernovae. It is no substitute, however, for a full calculation of radiative transfer, which eventually needs to be done. On the other hand, the light curves are also sensitive to details of the explosion physics, nuclear reactions, and shock hydrodynamics that are not customarily captured in spectral synthesis codes alone.

7.1. Opacity

The opacity consists of two parts, electron scattering and other processes that depend on details of the composition, ionization, velocity shear, and level populations. This second part will be referred to loosely as the "line opacity" or the "additive opacity." Electron scattering is calculated very well in the *KEPLER* code. A Saha equation is solved in every zone at every time step using the current temperature, density, and composition (Ensman & Woosley 1988). All ionization stages of all of the even-Z elements up to iron are calculated assuming thermal equilibrium. The resulting electron density is used to determine the electron scattering opacity, which is corrected for Compton scattering (including the change of a photon's energy in a scattering event), degeneracy, and the presence of pairs.

The line opacity, on the other hand, is treated poorly. It is represented by a single constant added to the electron scattering opacity at all times and places. In calculations of SNe IIp, this number is given a small value, $10^{-5}\,\mathrm{cm^2\,g^{-1}}$, that does not significantly affect the light curve. For SNe Ia, where it is generally recognized that, owing to the large metal content, lines play a dominant role, the constant frequently used is $\kappa_a \sim 0.1\,\mathrm{cm^2\,g^{-1}}$, where "$a$" stands for "additive." Figure 24 of Dessart et al. (2015) shows the actual opacity for a typical SN Ib model calculated using the CMFGEN code (Hillier & Dessart 2012), a state-of-the-art supernova radiation transport code. The non–electron scattering part is by no means constant but is larger near the center, where the nickel is concentrated, and at earlier times, when the density is higher. If one were to attempt to assign a single value to the difference in the dashed and solid lines in their figure (electron scattering and total opacity, respectively), it would be close to $\kappa_a \sim 0.2$ at early times for velocities less than $6000\,\mathrm{km\,s^{-1}}$ but much smaller near the peak of the light curve. There it ranges from about 0.07 near the center (v less than $3000\,\mathrm{km\,s^{-1}}$) to at most a few hundredths $\mathrm{cm^2\,g^{-1}}$ farther out. Since we are more interested in the behavior at peak than on the rise, κ_a was chosen to be $0.03\,\mathrm{cm^2\,g^{-1}}$. This low value may slightly underestimate the rise time compared with that of Dessart et al. (2012) but approximately captures the behavior near peak.

To test this calibration, the light curve of model 4.41 in Dessart et al. (2012) was recalculated using the *KEPLER* code and their assumption for mixing, which, in their most extreme case, is very similar to ours (Section 7.2). This entailed a running boxcar average with a box size of 0.2 $M_\odot$ passed through the model of Yoon et al. (2010) four times, a procedure identical to that used by Dessart et al. (2012). Several choices for κ_a were explored (Figure 18). In their Figure 7, the peak for their model 4.41×4 is $10^{42.47}\,\mathrm{erg\,s^{-1}}$, while ours is $10^{42.48}\,\mathrm{erg\,s^{-1}}$ for $\kappa_a = 0.03\,\mathrm{cm^2\,g^{-1}}$ and $10^{42.42}\,\mathrm{erg\,s^{-1}}$ for $\kappa_a = 0.05\,\mathrm{cm^2\,g^{-1}}$. Our two light curves peak at 27.5 and 30.6 days after explosion, while theirs peaks at 34.2 days. The discrepancy probably reflects the larger opacity early on in their models. The decline rate at late times is sensitive to the treatment of gamma-ray trapping, which is captured better in their full Monte Carlo simulation. All in all, though, if a single constant must be used, $\kappa_a = 0.03\,\mathrm{cm^2\,g^{-1}}$ seems to be a good value for calculating L_{peak}.

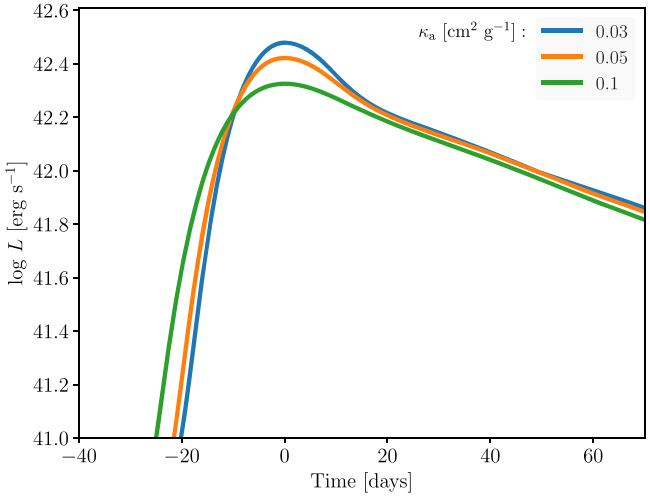

Figure 18. Light curve from the explosion of a 4.41 $M_\odot$ model (Yoon et al. 2010) with a kinetic energy of 1.2×10^{51} erg; an additive opacity $\kappa_a = 0.03$, 0.05, and 0.1 cm^2 g^{-1}; and strong mixing (Section 7.2). The smaller opacity ($\kappa_a = 0.03$ cm^2 g^{-1}) compares favorably in peak luminosity with an identical model calculated by Dessart et al. (2012) using the CMFGEN code with a more accurate treatment of radiation transport.

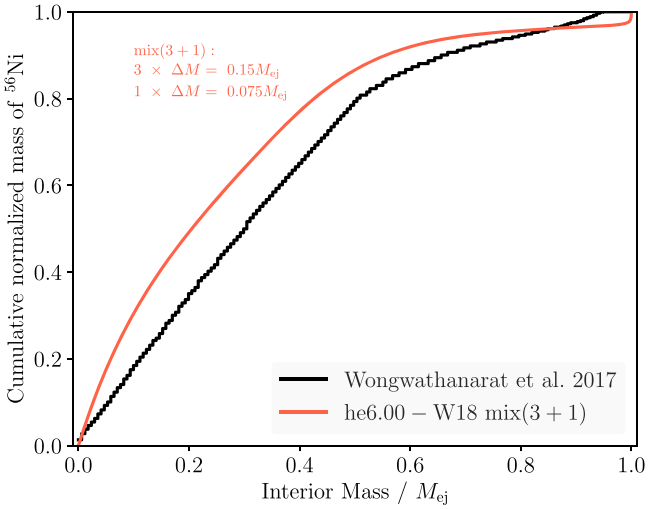

Figure 19. Mixing in our model He6.0 (red line), which had a final mass of 4.45 $M_\odot$, compared with mixing in the 4.5 $M_\odot$ helium core of model W15-2-cw-IIB of Wongwathanarat et al. (2017; black line). The plot shows the cumulative fraction of ^{56}Ni contained within the given mass. The inner 3.2 $M_\odot$ of our model He6.0 contains 90% of the ^{56}Ni. The velocity at that 90% point is 5190 km s^{-1}.

7.2. Mixing

The principal effect of mixing is to disperse ^{56}Ni from the central tenth or so solar masses where it is made to masses and speeds farther out in the star. The mixing in SNe I has its origin in the nonspherical nature of the central explosion, not so much the reverse shock as in SNe II. Mixing leads to a light curve that rises earlier, is a little broader, and declines earlier. Except for filling in a gap in emission at earlier times, the modification of the light curve near peak is not great. The effect on the spectrum (not calculated here), though, is very important (Dessart et al. 2012, 2015).

Mixing is inherently a 3D phenomenon and does not imply the homogenization at the atomic scale of any ejecta. Rather, clumps of one composition, which may carry radioactivity, are mixed out in velocity. As noted above, the average effects of mixing are incorporated in the *KEPLER* code using a "running boxcar average." A specified interval of mass (the "boxcar") is thoroughly mixed, and the process is repeated as this boxcar is moved out, zone by zone, through the star. The degree of mixing depends on the size of the boxcar and the number of times it passes through the star. The resulting distribution is quasi-exponential in mass.

Dessart et al. (2012) found that appreciable mixing was essential to obtain the correct colors and spectra for SNe Ib and Ic. Indeed, the degree to which ^{56}Ni was mixed into helium was the determining factor in whether the supernova was of Type Ib or Ic. Lacking the tamping influence of a massive hydrogen envelope, mixing in an almost stripped core extends farther out in velocity space than the 3500 km s^{-1} typical of models for SN 1987A (Wongwathanarat et al. 2015; Utrobin et al. 2019). There is a lack of 3D calculations of mixing in supernovae without hydrogen. The only exceptions are simulations of ultrastripped supernovae by Müller et al. (2018) and an SN IIb model of Wongwathanarat et al. (2017). The latter model, which had a hydrogen envelope of only 0.3 $M_\odot$ and therefore did not experience much deceleration by a reverse shock from the hydrogen-rich layer, was used to calibrate mixing in the present study.

The model they considered was the stripped-down core of a 15 $M_\odot$ red supergiant with a helium core of 4.5 $M_\odot$. For comparison, we used our 6.0 $M_\odot$ model, which had a final helium–plus–heavy-element core of 4.45 $M_\odot$. Figure 7 of Wongwathanarat et al. (2017) shows the angle-averaged ^{56}Ni mixing from their 3D run. The Wongwathanarat et al. (2017) model may have experienced more mixing than most others (A. Wongwathanarat 2019, private communication), so it is treated as an upper bound. The prescription finally employed in *KEPLER* used a boxcar width of 0.15 M_{ej}, where M_{ej} is the mass ejected in the supernova (presupernova mass minus remnant mass). This mixing region was moved through all of the ejecta three times, and then a final fourth mixing was applied using an interval half as great, i.e., 0.075 M_{ej}. The comparison with the model from Wongwathanarat et al. (2017) is shown in Figure 19. The result of the same mixing applied to the 2.5, 6.0, and 19.75 $M_\odot$ models is shown in Figure 20.

8. Calculated Light Curves

Given the input physics and parameterization described in Section 7, light curves were calculated for all models that exploded and left a neutron star remnant (Table 5). The lowest-mass models produced less ^{56}Ni and, in some cases, had large presupernova radii (Tables 3 and 5 of Woosley 2019). A few models that experienced a strong silicon flash had especially large radii. There the light curves were dominated by shock interaction and helium recombination. Higher-mass models resembled more common SNe Ib and Ic. Still higher masses resulted in long faint light curves that do not seem to be well represented in current observations. Which of these categories characterized a given model depended mostly on its presupernova mass. Depending on mass-loss rate, this could correspond to different initial helium core and main-sequence masses. Based on the standard mass-loss prescription used here, our discussion is broken into four sections: (a) helium stars with initial masses of 2.5–2.9 $M_\odot$ that have a large radius but did not experience a silicon flash, i.e., models with normal

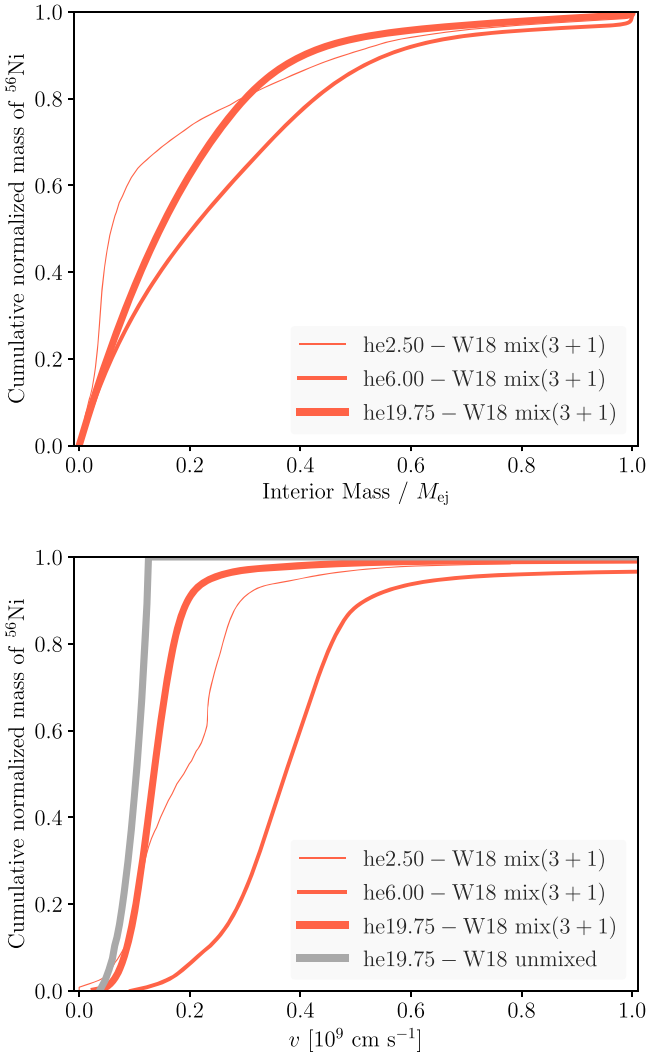

Figure 20. Mixing assumed in models He2.5, He6.0, and He19.75 as a function of mass and terminal speed. The presupernova masses of these models were 2.07, 4.45, and 10.28 $M_\odot$. The ejected masses are 0.731, 2.780, and 8.539 $M_\odot$. The curves show the integrated fraction of ^{56}Ni mass within the given mass or speed.

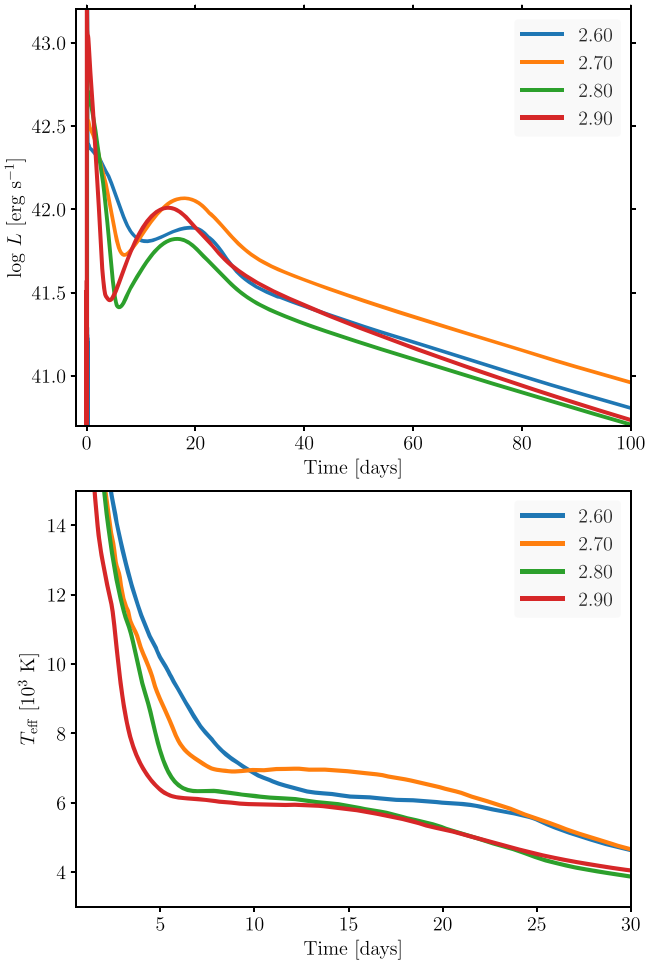

Figure 21. Light curves (top) and effective temperatures (bottom) for low-mass models (colors denote $M_{He,i}$). Some with radius expansion show an early peak from recombination and a fainter radioactive peak. None are very bright at second (radioactive) peak.

mass loss and initial helium masses of 2.6, 2.7, 2.8, and 2.9 $M_\odot$; (b) other low models that *did* experience an Si flash, i.e., models with initial helium core masses of 2.5, 3.0, 3.1, and 3.2 $M_\odot$; (c) "common" SNe Ib and Ic with initial masses 3.3–8.0 $M_\odot$; and (d) more massive stars. Some stars below 2.5 $M_\odot$ may still explode as electron-capture supernovae but are not included here, since their ^{56}Ni production would be very small and the presupernova radius large. They would resemble group (a). The physics of the silicon flash are sufficiently uncertain that groups (b) and (c) could perhaps be combined. Common SNe Ib and Ic would then extend down to models with initial helium masses of 3.0 $M_\odot$ with the lower bound set by radius expansion.

8.1. Low-mass Models with Radius Expansion

Models with initial helium core masses less than about 3.0 $M_\odot$ (3.3 $M_\odot$ if silicon flashes are strong) and standard mass loss experience significant radius expansion during their final stages of evolution (see Table 3 and Figure 5 of Woosley 2019). These stars have presupernova masses less than 2.45 $M_\odot$ (Table 1) and eject less than 1 $M_\odot$. Their explosion energies and ^{56}Ni production are smaller than the more massive models (Figure 5), so the radioactive portion of their light curves is fainter and faster. Some representative light curves are shown in Figure 21.

These are not what we usually think of as common SNe Ib or Ic. Their early display is dominated by envelope recombination. There are often two peaks, though the first is very blue. Some of these might be associated with "fast blue optical transients" (Kleiser et al. 2018; Woosley 2019), for example, models He2.60 and He2.70 with presupernova masses of 2.15 and 2.22 $M_\odot$ and radii of 7.8×10^{12} and 6.5×10^{12} cm, respectively. The properties of these two supernovae are summarized in Figure 21 and Table 6. These large presupernova radii, small ejected masses, and extended epochs of high effective temperature (Figure 21, lower panel) associated with shock breakout are also similar to what was inferred for SN 2013ge by Drout et al. (2016).

8.2. Silicon Flashes?

Particularly intriguing are the light curves of the low-mass models that experience a silicon deflagration and eject substantial matter well in advance of core collapse. As discussed

Table 5
Explosion and Light-curve Properties (Subset)

$M_{\rm He,i}$ ($M_\odot$)	$M_{\rm preSN}$ ($M_\odot$)	$M_{\rm ej}$ ($M_\odot$)	$E_{\rm exp}$ (B)	$M_{\rm Ni}$ ($M_\odot$)	log $L_{\rm peak}$ (erg s^{-1})	$t_{-1/2}$ (days)	$t_{+1/2}$ (days)	$M_{\rm ej}$ ($M_\odot$)	$E_{\rm exp}$ (B)	$M_{\rm Ni}$ ($M_\odot$)	log $L_{\rm peak}$ (erg s^{-1})	$t_{-1/2}$ (days)	$t_{+1/2}$ (days)
					Standard $\dot{M}$								
					W18						S19.8		
2.70	2.21	0.85	0.21	0.02	42.07	13.0	11.0	0.85	0.21	0.02	42.06	12.9	11.0
3.20	2.59	1.14	0.67	0.05	42.34	7.0	11.7	1.14	0.67	0.05	42.33	6.9	11.8
3.50	2.81	1.27	0.42	0.03	42.00	7.9	14.1	1.28	0.47	0.04	42.06	7.8	13.4
4.00	3.16	1.62	0.64	0.05	42.16	8.2	15.3	1.64	0.76	0.06	42.23	8.0	15.1
4.50	3.49	1.89	1.28	0.10	42.38	8.0	14.2	1.96	1.82	0.15	42.59	7.5	13.1
4.62	3.57	1.98	1.39	0.11	42.41	8.3	14.4	2.01	1.65	0.13	42.48	7.8	14.3
4.75	3.65	2.10	1.46	0.11	42.40	8.1	14.3	2.11	1.61	0.12	42.43	7.9	13.7
4.88	3.73	2.16	1.47	0.11	42.40	8.2	14.6	2.16	1.60	0.12	42.42	8.1	14.2
5.00	3.81	2.21	1.49	0.11	42.41	8.4	14.9	2.24	1.72	0.13	42.46	8.1	14.3
5.25	3.98	2.33	1.26	0.09	42.32	9.0	17.5	2.40	1.77	0.14	42.49	8.3	15.0
5.50	4.13	2.59	1.58	0.10	42.39	9.1	17.9	2.61	1.80	0.10	42.44	8.7	16.8
5.75	4.29	2.55	1.28	0.09	42.31	9.3	19.4	2.56	1.41	0.10	42.34	9.0	18.9
6.00	4.44	2.82	1.07	0.08	42.21	10.2	23.4	2.85	1.39	0.10	42.33	9.7	20.5
6.50	4.75	3.14	1.50	0.11	42.41	10.0	21.6	3.15	1.70	0.12	42.44	9.8	20.3
7.00	5.04	3.33	1.37	0.12	42.31	10.9	25.6	3.38	1.85	0.16	42.46	10.3	22.4
7.50	5.34	3.61	1.38	0.12	42.30	11.4	27.8	3.66	1.79	0.15	42.42	10.8	25.0
8.00	5.63	3.95	0.70	0.06	41.95	14.5	40.7	3.96	0.88	0.07	42.05	13.4	36.5
8.50	5.92	4.27	1.01	0.09	42.11	13.8	37.5	4.31	1.30	0.11	42.21	12.8	34.0
9.00	6.19	4.45	0.96	0.07	42.03	14.1	40.7	4.51	1.49	0.11	42.25	13.1	33.1
9.50	6.47	4.85	1.12	0.12	42.17	16.2	43.1	4.89	1.41	0.14	42.26	14.8	39.0
10.00	6.74	5.19	0.76	0.07	41.98	18.7	52.0	5.22	0.93	0.09	42.08	17.9	46.9
10.50	6.91	5.15	0.99	0.11	42.12	18.1	49.9	5.23	1.47	0.16	42.29	15.5	42.6
11.50	7.10	5.26	1.01	0.13	42.15	18.5	53.6	5.42	1.79	0.21	42.43	15.4	41.7
12.00	7.24	5.32	0.81	0.08	41.97	19.9	54.3	5.44	1.50	0.14	42.26	16.2	43.5
12.50	7.42	5.72	0.88	0.09	42.01	19.5	53.8	5.83	1.49	0.15	42.25	17.2	44.0
12.75	7.51	5.82	0.96	0.10	42.05	19.4	51.5	5.91	1.54	0.16	42.26	17.1	45.0
13.25	7.71	5.98	0.95	0.10	42.04	21.3	54.9	6.08	1.48	0.16	42.25	18.0	48.2
18.25	9.67	8.06	0.96	0.11	42.00	27.1	63.2	8.11	1.29	0.15	42.13	23.9	58.6
18.50	9.78	8.16	0.97	0.11	42.00	27.2	63.5	8.22	1.28	0.14	42.13	24.2	61.1
18.75	9.88	8.24	0.97	0.11	42.01	27.7	64.3	8.30	1.31	0.15	42.14	24.4	60.2
19.00	9.98	8.32	1.00	0.11	42.01	27.5	63.9	8.39	1.34	0.15	42.15	24.8	60.1
19.25	10.1	8.31	0.78	0.06	41.66	29.0	66.8	8.47	1.35	0.15	42.15	25.2	61.1
19.50	10.2	8.43	0.84	0.08	41.82	27.7	65.9	8.56	1.36	0.16	42.16	25.7	59.1
19.75	10.3	8.53	0.87	0.09	41.86	29.3	64.7	8.65	1.40	0.16	42.17	25.1	59.9
					$1.5 \times \dot{M}$								
					W18						S19.8		
5.00	3.43	1.85	1.58	0.12	42.49	7.5	13.4	1.88	1.86	0.14	42.58	7.2	12.6
5.25	3.57	1.96	1.50	0.12	42.46	7.7	14.5	2.00	1.81	0.15	42.52	7.6	13.4
5.50	3.70	2.08	1.47	0.11	42.43	8.1	15.2	2.12	1.80	0.14	42.53	7.8	14.1
5.75	3.83	2.20	1.42	0.10	42.37	8.3	15.2	2.24	1.76	0.13	42.47	7.9	14.7
6.00	3.96	2.32	1.55	0.12	42.42	8.4	15.7	2.35	1.80	0.14	42.47	8.0	15.3
6.25	4.09	2.41	1.47	0.11	42.38	8.7	17.1	2.43	1.68	0.12	42.44	8.4	16.7
6.50	4.21	2.50	1.31	0.10	42.32	9.0	19.5	2.55	1.79	0.14	42.47	8.5	16.8
6.75	4.33	2.74	1.44	0.11	42.33	9.4	19.6	2.76	1.66	0.11	42.39	8.9	19.0
7.00	4.45	2.84	1.44	0.11	42.37	9.5	20.7	2.86	1.71	0.14	42.45	9.3	19.6
7.50	4.69	3.02	1.39	0.12	42.33	10.0	23.0	3.04	1.65	0.13	42.39	9.7	21.5
8.00	4.92	3.26	1.47	0.12	42.38	10.4	23.8	3.30	1.83	0.14	42.51	10.0	21.5
8.50	4.90	3.18	1.35	0.12	42.31	10.8	24.8	3.21	1.61	0.14	42.37	10.2	23.0
9.00	4.87	3.14	1.01	0.08	42.14	11.4	26.7	3.16	1.23	0.09	42.22	10.7	25.3
9.50	4.89	3.16	1.41	0.13	42.33	10.6	24.3	3.21	1.87	0.16	42.46	10.1	21.8
10.00	4.96	3.20	1.24	0.11	42.27	11.4	27.4	3.26	1.72	0.15	42.40	10.5	23.2
10.50	5.08	3.45	0.96	0.10	42.16	13.5	32.9	3.53	1.48	0.15	42.35	11.8	27.2
11.00	5.19	3.44	1.12	0.11	42.23	12.6	31.3	3.49	1.48	0.14	42.34	11.8	27.2
11.50	5.32	3.60	1.02	0.10	42.17	13.7	33.1	3.66	1.47	0.14	42.33	12.1	28.2
12.00	5.43	3.71	0.98	0.09	42.15	13.4	35.2	3.78	1.45	0.13	42.32	12.4	29.2
12.50	5.53	3.82	1.41	0.14	42.30	12.3	30.7	3.88	1.86	0.17	42.44	11.8	26.6
13.00	5.64	3.98	1.29	0.12	42.30	13.1	33.0	4.00	1.45	0.14	42.34	12.8	31.1
14.00	5.86	4.22	1.20	0.12	42.24	14.6	37.2	4.27	1.52	0.16	42.32	13.5	33.4
15.00	6.09	4.45	0.95	0.09	42.10	16.1	43.5	4.53	1.46	0.14	42.30	14.3	34.7
16.00	6.34	4.72	0.54	0.03	41.44	17.6	49.7	4.79	0.66	0.06	41.91	19.1	49.2
17.00	6.59	4.72	1.04	0.10	42.11	16.1	44.4	4.76	1.37	0.12	42.23	14.8	39.6

Table 5
(Continued)

$M_{\rm He,i}$ ($M_\odot$)	$M_{\rm preSN}$ ($M_\odot$)	$M_{\rm ej}$ ($M_\odot$)	$E_{\rm exp}$ (B)	$M_{\rm Ni}$ ($M_\odot$)	log $L_{\rm peak}$ (erg s^{-1})	$t_{-1/2}$ (days)	$t_{+1/2}$ (days)	$M_{\rm ej}$ ($M_\odot$)	$E_{\rm exp}$ (B)	$M_{\rm Ni}$ ($M_\odot$)	log $L_{\rm peak}$ (erg s^{-1})	$t_{-1/2}$ (days)	$t_{+1/2}$ (days)
17.50	6.71	5.08	1.74	0.20	42.45	14.8	38.1	5.10	1.95	0.22	42.49	14.4	36.6
19.75	7.32	5.68	1.17	0.12	42.16	18.0	47.1	5.73	1.50	0.15	42.25	16.5	43.4
20.50	7.53	5.69	0.90	0.09	41.97	20.4	54.8	5.86	1.59	0.17	42.30	17.3	44.3
28.00	9.77	8.01	0.84	0.06	41.62	25.3	67.0	8.10	1.01	0.11	42.00	26.9	62.8
29.00	10.1	8.21	0.79	0.02	40.47	36.2	48.0	8.46	1.37	0.16	42.16	25.0	59.6
29.50	10.3	8.39	0.82	0.04	41.06	25.2	62.8	8.61	1.38	0.16	42.16	24.9	62.1

Table 6
Properties of Low-mass Models

	Time (days)	log $L_{\rm bol}$ (erg s^{-1})	$T_{\rm eff}$ (10^3 K)
He2.60	1	42.36	22.8
	2	42.32	16.3
	5	42.12	10.2
	Peak	41.89	6.11
He2.70	1	42.47	22.0
	2	42.36	15.3
	5	41.90	8.81
	Peak	42.07	6.64

Note. Peak is the time of the second light-curve peak powered by radioactivity, which was 19.4 and 18.0 days for models He2.60 and He2.70, respectively.

Table 7
Properties of Silicon Flash Models

$M_{\rm He,i}$ ($M_\odot$)	$M_{\rm preSN}$ ($M_\odot$)	$M_{\rm ej,Si}$ ($M_\odot$)	$t_{\rm ej,Si}$ (days)	$KE_{\rm ej,Si}$ (10^{47} erg)	$E_{\rm exp}$ (10^{51} erg)	$M_{\rm Ni}$ ($M_\odot$)
2.5	2.07	0.25	16	0.93	0.115	0.027
3.0	2.45	0.74	62	190	0.303	0.035
3.1	2.52	0.42	34	49	0.621	0.080
3.2	2.59	0.02	15	0.47	0.668	0.079

Note. Here $M_{\rm ej,Si}$ is the mass of the shell ejected by the silicon flash, and $KE_{\rm ej,Si}$ is its kinetic energy; $t_{\rm ej,Si}$ is the delay between the flash and iron core collapse. Many other combinations are possible.

in Woosley (2019), the amount of matter ejected and its timing depend on the poorly understood 3D aspects of the silicon flash and are uncertain. In cases where a lot of mass is lost months to years before collapse, the resulting supernova can be very bright.

Figure 22 and Table 7 show a representative range of possibilities with the brightness of the light curve being mostly determined by the timing and energy of the silicon flash. Typically, the flash occurs several weeks prior to iron core collapse. The mean velocity of the ejecta is $v_{\rm ej,Si} \sim (2\,KE_{\rm ej,Si}/M_{\rm ej,Si})^{1/2}$, and models where the shell expands to $v_{\rm ej,Si}t_{\rm ej,Si} \sim 10^{14}$–$10^{15}$ cm will be especially bright. This criterion explains the great brightness of models He3.0 and He3.1, which have $v_{\rm ej,Si}t_{\rm ej,Si} = 0.85$ and 0.32×10^{15} cm, respectively. The amount of mass ejected and the radius reached by that ejecta are not so extreme in the other two models (only to a few times 10^{13} cm), so they are brighter than typical SNe Ib and Ic only during the first few days after the explosion. At their second bright peaks, models He3.0 and He3.1 had peak luminosities of $10^{44.54}$ and $10^{44.88}$ erg s^{-1} at days 4.5 and 8.3. The effective temperatures there were not well determined, since they were due to shock interaction, but they were calculated to be 21,000 and 32,000 K. Models He2.5 and He3.2, on the other hand, had weak secondary maxima due to radioactivity of $10^{41.90}$ and $10^{42.34}$ erg s^{-1} at days 22 and 15. Their effective temperatures then were only 5900 and 6600 K.

The mass and energy of the ejected shell and the delay time are determined mostly by the amount of silicon that burns explosively in the flash and not directly by the mass of the star that explodes. Brighter explosions could be generated by 2.5 and 3.2 $M_\odot$ models and fainter ones by 3.0 and 3.1 $M_\odot$ models. The four choices here are a very limited sampling meant to illustrate a broad possibility of outcomes. In cases where the silicon flash is weak or absent, these supernovae would resemble the models of Section 8.1. See Woosley (2019) for further details and a comparison to SN 2014ft (De et al. 2018).

8.3. Common SNe Ib and Ic

For the standard mass-loss rate, the most likely candidates for common SNe Ib and Ic have initial helium star masses between 3.0 and 8.0 $M_\odot$. These produce presupernova stars with masses of 2.45–5.63 $M_\odot$. Lower-mass stars experience radius expansion, produce little ^{56}Ni, and do not look like common events. The subinterval 3.0–3.2 $M_\odot$ might make normal SNe Ib and Ic but is complicated by the possibility of strong silicon flashes. More massive stars expand too slowly and make broad, faint events (Section 8.6). Both boundaries, 3.0 and 8.0 $M_\odot$, are imprecise and depend on the assumed mass-loss rate.

Figure 23 shows the expected light curves for all of the models in this mass range that do not experience a strong silicon flash. The interval of initial helium core masses between 3.0 and 8.0 $M_\odot$ has been further divided into two subintervals, 3.0–5.0 $M_\odot$ ($2.5 < M_{\rm preSN} < 3.8$) and 5.0–8.0 $M_\odot$ ($3.8 < M_{\rm preSN} < 5.6$), to highlight some systematic variations with mass. More realistic calculations of radiation transport than possible with *KEPLER* will be needed to tell if, spectroscopically, these two regions correspond to SNe Ib and Ic. From Table 1, one expects that all of the models in this mass range would be Type Ib, since Y_s remains close to 1, but it may not be necessary to remove all of the helium to make a Type Ic. Similar presupernova models result from higher-mass stars with greater mass loss; Table 1 shows that if the mass-loss rate is multiplied by 1.5, stars with presupernova masses over 5 $M_\odot$ will lose their helium.

Figure 24 shows the mass ejected by supernovae in approximately this same mass range. These calculations used the W18 engine. Including every star that exploded, the median mass ejected was 2.21 $M_\odot$, and the average was 2.97 $M_\odot$, but for the limited range shown here and relevant to SNe Ib and Ic,

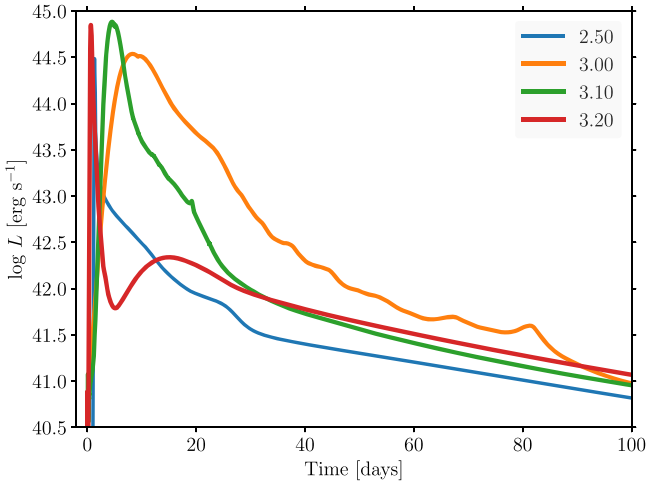

Figure 22. Light curves for supernovae that experienced silicon flashes accompanied by mass ejection prior to core collapse. The bright displays are due to the interaction of matter ejected by core collapse with the previously ejected shell. Colors denote $M_{\rm He,i}$.

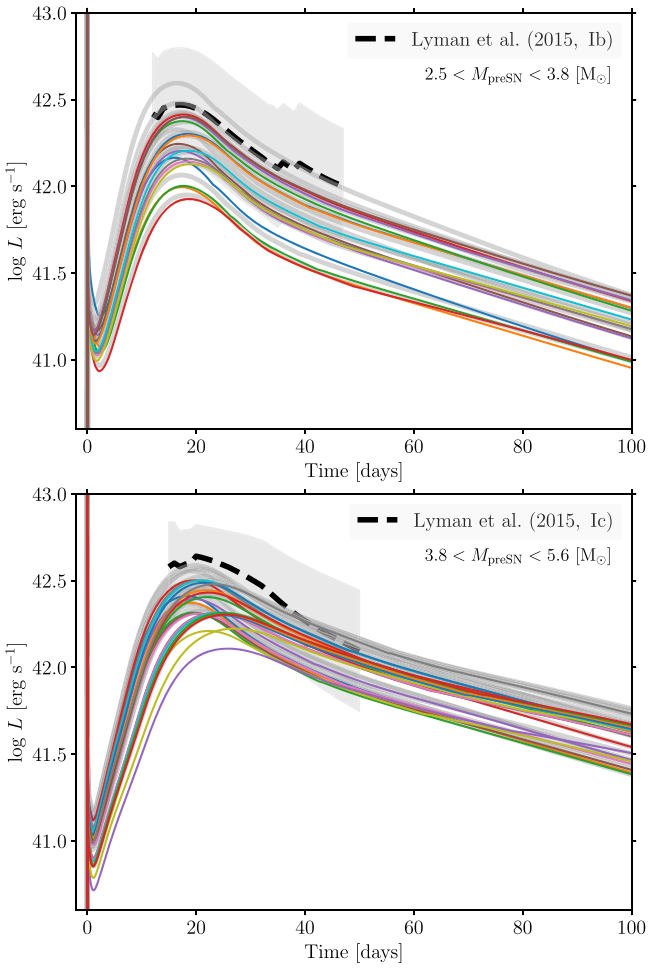

Figure 23. Light curves for SNe Ib and Ic. The mass range is broken into two intervals of $M_{\rm He,i}$, 3–5 (upper panel) and 5–8 (lower panel) $M_\odot$, to show systematics.

the median and mean masses were 2.31 and 2.30 $M_\odot$. This does not include the low-mass explosions with radius expansion or the high-mass ones that produce unusual light curves (Section 8.6). These values are similar to those for observed SNe Ib and Ic (Drout et al. 2011; Lyman et al. 2016;

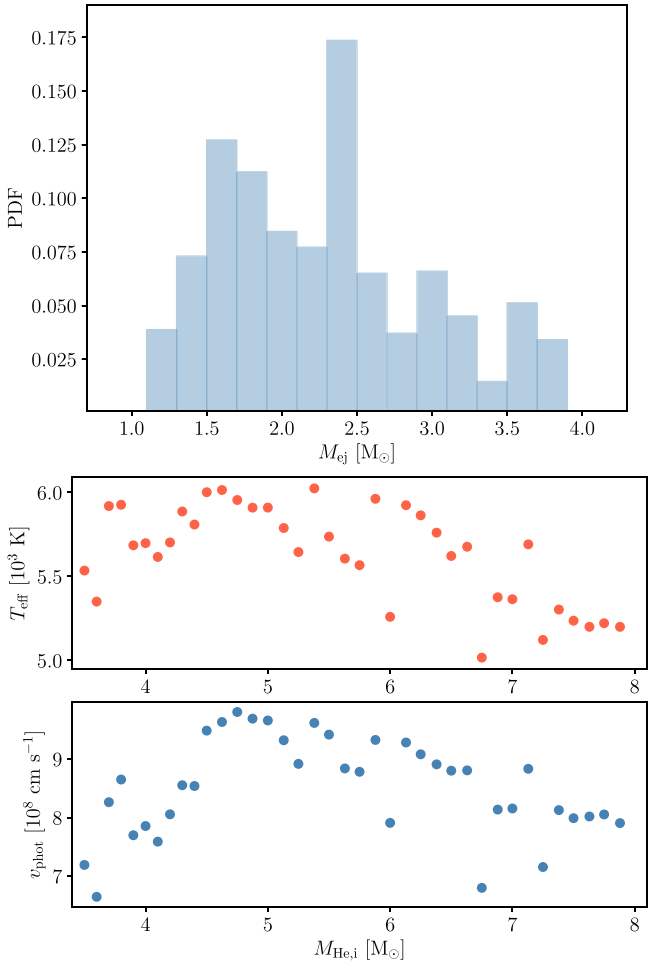

Figure 24. Top: mass ejected by SNe Ib and Ic weighted by the IMF. The initial helium star masses are in the range 3.05–7.9 $M_\odot$, so the presupernova stars have masses 2.45–5.64 $M_\odot$. The median mass ejected is 2.31 $M_\odot$, and the average is 2.30 $M_\odot$. Higher presupernova mass models that might be SNe Ic eject more mass than those with lower presupernova mass. Middle: photospheric velocity at light-curve maximum for this same set of models. Bottom: their effective temperatures.

Prentice et al. 2019). In particular, Prentice et al. (2019) reported observed median and mean ejected masses for Type Ib of 2.0 and 2.20 $M_\odot$. For Type Ic, the median is 2.2 $M_\odot$ and the mean is 3.2 $M_\odot$, though the error bars in all cases are large (of order 1 $M_\odot$). Figure 24 shows that this may reflect an actual large spread of masses in nature.

For a typical explosion energy of 10^{51} erg, our masses imply average expansion speeds of order 7000 km s^{-1}, but substantial material moves much faster than this average and dominates the spectrum at early times. The lower panels of Figure 24 show the effective temperature and the speed of the zone at the photosphere at the time of peak light. Low-mass models below 3.5 $M_\odot$ have not been included because of the lingering effects of radius expansion. The 8.0 $M_\odot$ model was also dropped because of an anomalously low explosion energy (7×10^{50} erg). That is not to say that these explosions do not exist, just that they are atypical. The remaining velocities at peak light lie between 6500 and 10,000 km s^{-1}. Speeds above the photosphere are larger and may affect the spectrum. Generally, though, these predictions agree with what is observed for Types Ib and Ic at peak (e.g., Table 6 of Lyman et al. 2016). Photospheric temperatures are between 5000 and 6000 K, and that also agrees reasonably well with

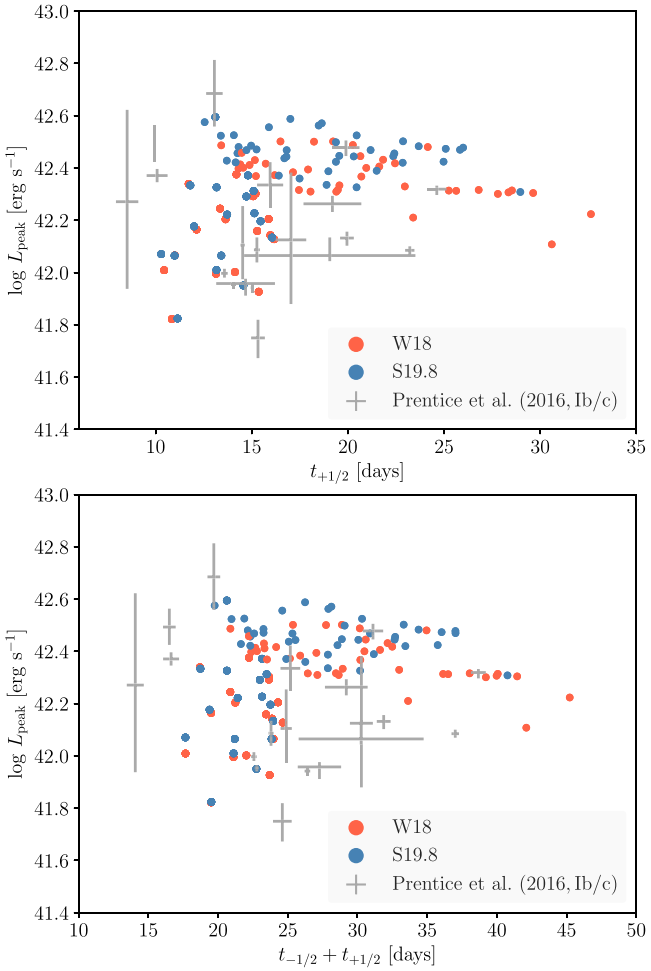

Figure 25. Width–luminosity relations for SNe Ib and Ic with initial helium star masses between 3.0 and 8 $M_\odot$ (presupernova masses 2.45–5.64 $M_\odot$), excluding the models with a silicon flash before final explosion. Top: peak luminosity vs. time for the light curve to decline to 50% of its peak value. Bottom: peak luminosity as a function of FWHM.

observations (Prentice et al. 2019), though perhaps on the cool side.

Generally speaking, the models also have light-curve shapes —rise times and durations—similar to observations (Figure 25; Table 8) but are too faint at peak, on average, by a factor of about 1.5, even using our most optimistic ^{56}Ni yields (0.75 times Ni+Tr+α; Figure 9; Section 3.3). Prentice et al. (2016) gave a median luminosity at peak for common SNe Ib and Ic of $10^{42.50}$ and $10^{42.51}$ erg s^{-1}, respectively. Lyman et al. (2016) gave a similar value for Type Ib but $10^{42.6}$ erg s^{-1} for Type Ic (our Figure 23; their Figure 3). Generally, only our brightest, most energetic supernovae approach these medians. The discrepancy is worse if the ^{56}Ni yield is estimated more conservatively using the approach of Sukhbold et al. (2016). A more recent observational study by Prentice et al. (2019) gives substantially reduced values, $10^{42.3\pm0.2}$ erg s^{-1} for the mean of SNe Ib and $10^{42.3\pm0.3}$ erg s^{-1} for narrow-lined Type Ic. These values are within reach of our more optimistic (highest-energy, greatest ^{56}Ni mass) models but are only for the emission from 4000 to 10000 Å. A larger value is expected when the ultraviolet and infrared emission is included (S. Prentice 2019, private communication). All in all, though, it seems that neutrino-powered explosions as parameterized here have trouble making enough ^{56}Ni to explain the light curves of

Table 8
Average Light-curve Properties

		log L_{peak} (erg s^{-1})	$t_{+1/2}$ (days)	$t_{-1/2}$ (days)	log L_{peak} (2016) (erg s^{-1})
		Overall			
W18	Median	42.15	14.6	8.33	41.87
	Mean	42.17	21.2	10.4	41.88
S19.8	Median	42.23	14.3	8.18	
	Mean	42.23	22.4	10.9	
		$8 > M_{He,i} \geqslant 3$			
W18	Median	42.29	15.0	8.29	41.96
	Mean	42.25	16.9	8.74	41.94
S19.8	Median	42.33	14.6	8.07	
	Mean	42.30	16.0	8.51	
		$5 > M_{He,i} \geqslant 3$			
W18	Median	42.15	14.1	7.99	41.94
	Mean	42.17	14.0	7.96	41.93
S19.8	Median	42.22	13.4	7.93	
	Mean	42.21	13.8	7.86	
		$8 > M_{He,i} \geqslant 5$			
W18	Median	42.37	20.2	9.85	41.98
	Mean	42.36	21.6	10.0	41.95
S19.8	Median	42.46	18.7	9.47	
	Mean	42.46	19.7	9.56	
		$M_{He,i} \geqslant 8$			
W18	Median	42.11	44.5	16.3	41.87
	Mean	42.08	47.3	17.9	41.88
S19.8	Median	42.24	42.2	16.0	
	Mean	42.22	46.8	18.5	

Note. The rise time from 50% to peak luminosity, $t_{-1/2}$; the decline time from peak to 50% of peak luminosity, $t_{+1/2}$; and the peak luminosity, L_{peak}, are based on models with maximum ^{56}Ni (Ni_{max} of Table 2).

many of the brighter ordinary SNe Ib and Ic reported in the literature. A similar conclusion was reached by Anderson (2019). This flies in the face of current convention, which states that all such supernovae come from binaries, are neutrino-powered, and have radioactive-powered light curves, and warrants some discussion.

8.4. Toward Brighter SNe Ib and Ic

The simplest, traditional way to make a SN I brighter is to increase its ^{56}Ni yield. Though numerically convenient, such variations are actually severely limited by physics and other observations. Whatever is done for Type Ib and Ic models must also be done for Type IIp models, which have very similar core structure and explosion characteristics (Section 4.5 and Appendix A). There are limits from iron nucleosynthesis (Section 5), the ^{56}Ni produced in SN 1987A (Section 5), the tails of the light curves of SNe IIp (Anderson 2019), and the masses of neutron stars (Section 6.1) that prohibit moving the mass cut in too deep. Thus, other explanations of the bright light curves of SNe Ib and Ic are also explored here: an embedded magnetar and circumstellar interaction.

8.5. A Deeper Cut—Some Limits on ^{56}Ni Production

The required average ^{56}Ni production for common SNe Ib and Ic, based upon observations and assuming the luminosity at peak is derived solely from radioactivity and given by Arnett's rule (a questionable assumption; Dessart et al. 2015), is $0.14^{+0.04}_{-0.04}\,M_\odot$ for Type Ib and $0.16^{+0.03}_{-0.10}\,M_\odot$ for Type Ic, according to Prentice et al. (2016). Lyman et al. (2016) gave

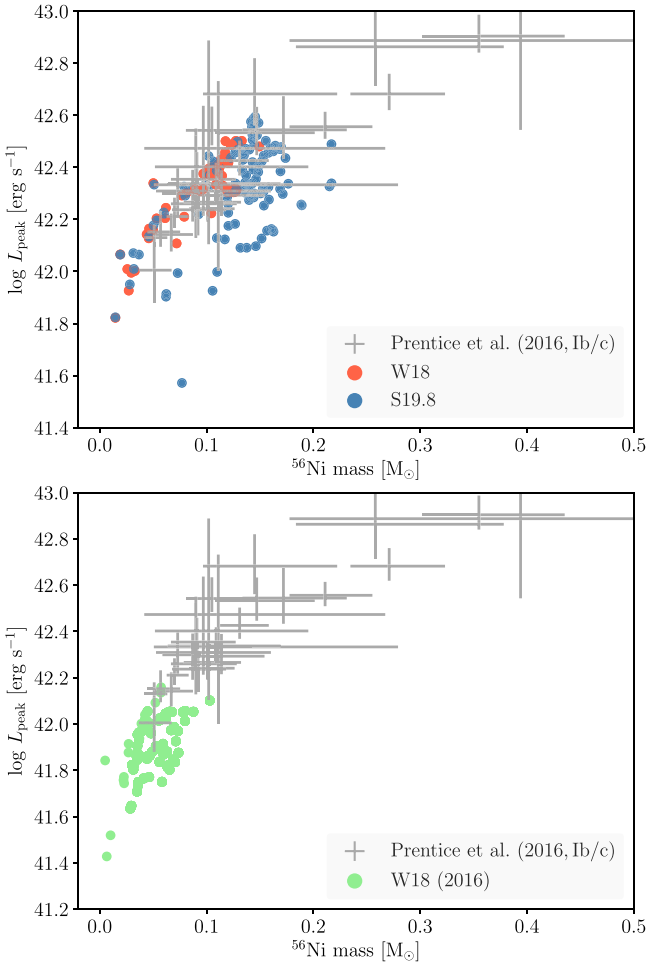

Figure 26. Peak luminosity as a function of ^{56}Ni mass for the present models compared with the bolometric luminosities at peak as determined for a large set of normal SNe Ib and Ic by Prentice et al. (2016). Top: Using the current analysis approach, which maximizes the ^{56}Ni yield (see text), the observations at a given ^{56}Ni mass are typically 1.5 times brighter than the models. Blue and red points represent two choices for the central engine; S19.8 is more energetic. There are also many very luminous supernovae that are observed to have luminosities and inferred ^{56}Ni masses greater than any of our standard models. Bottom: The discrepancy is worse if we analyze the ^{56}Ni yields using the approach of Sukhbold et al. (2016). Here green points are for the W18 central engine. The discrepancy in averages is now about a factor of 3.

slightly larger values, $0.17 \pm 0.16\,M_\odot$ for Type Ib and $0.22 \pm 0.16\,M_\odot$ for Type Ic. Anderson (2019) also gave similar values based on a literature survey, $0.163\,M_\odot$ for Type Ib and $0.155\,M_\odot$ for Type Ic. In mild tension with these numbers, recent studies by Prentice et al. (2019) gave mean ^{56}Ni production of $0.09 \pm 0.06\,M_\odot$ for Type Ib and $0.11 \pm 0.09\,M_\odot$ for Type Ic, but as noted previously, these values are based on observations in a limited wavelength range and are lower bounds. The larger values for the average ^{56}Ni masses (i.e., those other than Prentice et al. 2019) are appreciably greater than computed here for models in the initial mass range 3.0–8 $M_\odot$, the ones in our study deemed most likely to make these sorts of supernovae (Figure 26). As noted in Section 5 and Table 2, the average ^{56}Ni production for the W18 central engine for stars likely to become SNe Ib or Ic ranges from $0.034\,M_\odot$ for the lower-mass stars, weaker engine, and conservative approach to evaluating ^{56}Ni production to $0.13\,M_\odot$ for the highest-mass, most energetic models evaluated in the most optimistic way. Our best estimate would be between Ni and Ni+Tr/2 in Table 2 for the W18 and S19.8 central engines, which is between 0.034 and $0.097\,M_\odot$, with the smaller value appropriate for the lower-mass supernovae and weaker engine.

Since a large fraction of the observations are explained by models within our error bar, it is natural to ask if still larger values might be possible. Physically, the ^{56}Ni yield is constrained by the amount of matter that attains a peak temperature in excess of about 5×10^9 K and is ejected with a small neutron excess. This is an upper bound because other iron-group isotopes will be produced, and the fraction of helium from the alpha-rich freeze out is not small. A much smaller contribution to ^{56}Ni also comes from matter experiencing explosive silicon burning between 4 and 5×10^9 K. A popular ansatz for the explosion temperature, $T_{\rm exp}$, is given by (Woosley et al. 2002)

$$\frac{4}{3}\pi r^3 f a T_{\rm exp}^4 \approx E_{\rm exp}, \tag{13}$$

where $E_{\rm exp}$ is the energy of the explosion, usually taken to be the final kinetic energy; r is the radius at the time the supernova shock begins to move outward from the zone that eventually achieves $T_{\rm exp}$; a is the radiation constant; and f is a factor that accounts for the presence of electron–positron pairs. Often the radius of the given mass shell is evaluated using a presupernova model, assuming that the adjustment before the shock arrives is negligible and f is taken to be 1.

In the present situation, even an approximate result requires some improvements. First, the abundance of pairs is not negligible. For the temperatures of relevance, 4×10^9 K and higher, $f \approx 11/4$, similar to its value in the early Big Bang (Peebles 1993). This has been verified for our models using the *KEPLER* EOS. Second, the settling of mass shells located only a few thousand km out as the explosion develops cannot be neglected. The gravitational acceleration at 4000 km is about 10^9 cm s^{-2}, and the time from the presupernova stage to the launch of the shock is typically 0.5–1 s. Even though the layers are not far from hydrostatic equilibrium, a contraction of 35% is typical. Finally, the full energy of the explosion may not have been developed when the shock temperature declines to 5×10^9 K. Since the explosion energy only enters as $E^{1/3}$ and most of the explosion energy has usually been deposited, this last factor is not critical.

Still, appropriately corrected, Equation (13) works very well. For an explosion energy of 1.2×10^{51} erg and $f = 2.75$, the equation says that a temperature greater than 5×10^9 K is achieved inside a radius of 2800 km. For $f = 1$, the boundary radius is increased to 3900 km. Examining the runs themselves, 90% of ^{56}Ni is typically synthesized inside a radius that, if the structure is evaluated when the shock is launched, has a value of 2970 ± 9 km. The same 90% criterion gives a radius of 4470 ± 5 km using radii in the presupernova star. Of course, it is not realistic to neglect pairs, but it turns out that the correction to the radius for pairs, $(11/4)^{1/3} \approx 1.40$, very nearly cancels the contraction factor, $4470/2970 \approx 1.50$. Thus, Equation (13) can be used approximately with either $f = 1$ and r (the presupernova radius) or $f = 2.75$ and r (the radius in the star when the shock is launched). This Lagrangian mass shell in the presupernova star where the shock temperature declines below 5×10^9 K, the value required to achieve NSE on a hydrodynamic timescale, will be referred to as $M_{\rm T9=5}$.

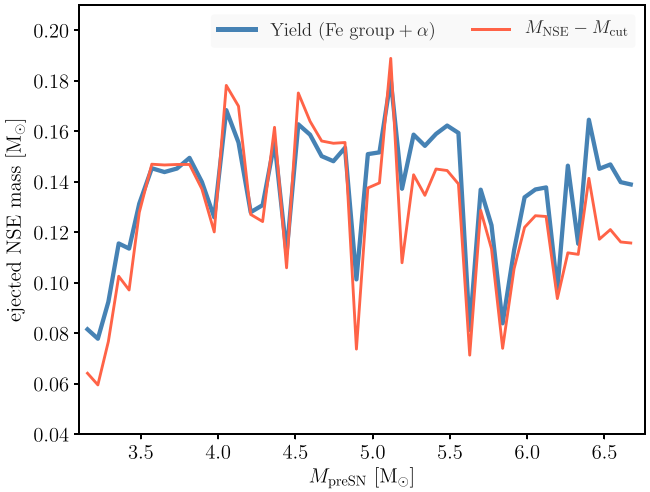

Figure 27. The estimated mass of material that attains NSE and is ejected is compared to the actual ejected mass of iron-group nuclei plus helium from photodisintegration in the models based on the S19.8 central engine. The estimated mass is the difference between the mass, $M_{T9=5}$, where the shock temperature falls below 5×10^9 K and the baryonic remnant mass when the explosion is over. Here the radius used for estimating the shock temperature was calculated using Equation (13) with $f = 2.75$ and the radii in the model when the shock was launched. A very similar plot would result if one used $f = 1$ in Equation (13) and the presupernova zonal radii. Final helium presupernova masses corresponding to these initial masses are given in Table 4 of Woosley (2019) and Section 2.

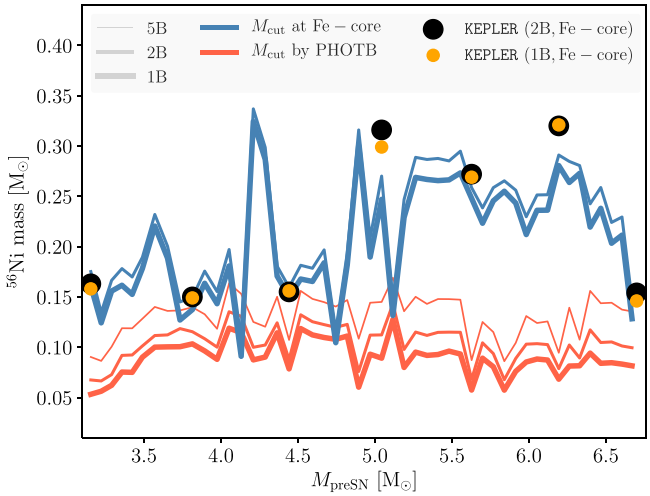

Figure 28. Maximum yields for ^{56}Ni. The red lines explore the effect of varying the explosion energy from 1 to 5×10^{51} erg. Values larger than 2×10^{51} erg are incompatible with neutrino-powered models using known physics. As in Figure 27, the ejected mass is estimated by subtracting M_{rem} from $M_{T9=5}$. The latter is calculated using the stars' density structure at bounce and Equation (13) with $f = 2.75$. The blue lines show that greater variation is obtained by artificially reducing the remnant mass, here taken to be the iron core. Black and orange circles represent actual *KEPLER* models that used the iron core mass for the location of the piston (which became the mass cut). In both cases, the mass that achieves NSE and is ejected has been multiplied by an efficiency factor, 0.75, to give ^{56}Ni synthesis. Potentially large ^{56}Ni yields, up to 0.33 $M_\odot$, are numerically possible but incompatible with neutrino-powered explosions and may give results that are inconsistent with constraints from stellar nucleosynthesis and neutron star masses.

It is important to note that $M_{T9=5}$ is mostly a function of presupernova structure. It depends only weakly on explosion energy and not on the mass cut. The mass of the ejecta that is heated above 5×10^9 K is then just $M_{T9=5} - M_{rem}$, where M_{rem} is the baryonic mass of the gravitationally bound remnant. Figure 27 shows the good agreement of this estimate with the mass of ejected material that actually achieved NSE in those models likely to make SNe Ib or Ic. The agreement suggests that the ^{56}Ni yield is not sensitive to details of how the explosion is calculated but mostly to the final mass cut and, secondarily, the explosion time.

This semianalytic model allows a qualitative exploration of how ^{56}Ni synthesis might change as the explosion energy and mass cut are varied for a given presupernova star. Figure 28 shows the results if the explosion energy is varied between 1 and 5×10^{51} erg or the mass cut is moved in to the edge of the iron core. These are extreme excursions. None of our models had explosion energies exceeding 2.0×10^{51} erg, even with the energetic S19.8 engine, and most had less (Figure 5). No modern calculation of a purely neutrino-powered model that we know of has greatly exceeded that (e.g., Fryer 1999; Fryer & Kalogera 2001; Scheck et al. 2006; Bruenn et al. 2016; Müller et al. 2017). Similarly, the mass cut in neutrino-powered models rarely, if ever, occurs as deep as the edge of the iron core. The reduction in remnant mass might also cause an unacceptable decrease in the mean neutron star mass (Section 6.1) and could make the contribution of SNe Ia to iron synthesis a minor component. Nevertheless, neglecting these constraints, the synthesis of iron group plus alphas might be pushed to $\sim$0.20 $M_\odot$. For reasonable explosion energies, the placement of the mass cut has more leverage on the yield than the explosion energy. The maximum ^{56}Ni mass, even in models that have unreasonable mass cuts, is 0.33 $M_\odot$. Some past studies, e.g., Dessart et al. (2012, 2015), arbitrarily placed the mass cut at the edge of the iron core and thus overestimated the ^{56}Ni yield for purely neutrino-powered explosions.

In summary, larger ^{56}Ni yields capable of resolving the discrepancy between the models and the observed brightness of SNe Ib and Ic might conceivably be possible, and certainly can be prepared in parameterized explosions, but they are not achievable in today's neutrino-powered models. The yields may violate limits on iron nucleosynthesis, and the neutron stars may be too small compared to observations. The same approximations applied to SN 1987A would overproduce ^{56}Ni there. An additional source of energy seems to be required to explain supernovae brighter than about $10^{42.5}$ erg s^{-1}.

8.5.1. Circumstellar Interaction

The brightness of the supernova could be amplified by colliding with a circumstellar gas, presumably the outcome of mass loss during the final year of the star's life (e.g., Shiode & Quataert 2014; Woosley 2017). On the positive side, ample energy exists in the outer edge of the ejecta, and the required circumstellar mass (CSM) is not large. In a typical Ib progenitor, e.g., model He6.0, the outer 0.001 $M_\odot$ moves at speeds in excess of 0.1c, implying a kinetic energy in this small mass of $\sim 10^{49}$ erg, more than enough to explain the full light curve of a typical SN Ib. This would only need to encounter $\sim$0.001 $M_\odot$ of CSM matter inside a radius of a few times 10^{15} cm.

On the other hand, getting the time structure of the light curve is problematic and requires the introduction of many uncertain parameters (Chatzopoulos et al. 2013; Vreeswijk et al. 2017). The spectrum from such high-velocity material might not resemble common SNe Ib and Ic. In the simplest case

of a steady wind in which $\rho \propto r^{-2}$, the luminosity

$$L_{\rm csm} \approx 0.5 \dot{M} v_{\rm shock}^3 / v_{\rm wind}, \quad (14)$$

where $\dot{M}$ is the mass-loss rate, $v_{\rm wind}$ is the wind speed, and $v_{\rm shock}$ is the speed of the fast-moving supernova ejecta. For $\dot{M} = 2 \times 10^{-4}\, M_\odot\ {\rm yr}^{-1}$, $v_{\rm wind} = 500\,{\rm km\,s^{-1}}$, and $v_{\rm shock} = 30{,}000\,{\rm km\,s^{-1}}$, the luminosity is $3 \times 10^{42}\,{\rm erg\,s^{-1}}$. This luminosity would persist and slowly decline until the fast-moving ejecta encountered about half its mass, or ~20 days. But the light curve would commence immediately and decline slowly, quite unlike what is observed.

Assuming a CSM shell with constant density only improves things marginally. Now the luminosity

$$L_{\rm csm} \approx 2\pi r^2 \rho v_{\rm shock}^3 \quad (15)$$

$$\approx 2\pi \rho v_{\rm shock}^5 t^2 \quad (16)$$

$$\approx 4 \times 10^{42} \left(\frac{v_{\rm shock}}{3 \times 10^9}\right)^5 \left(\frac{\rho}{10^{-17}}\right) {\rm erg\ s^{-1}} \quad (17)$$

increases quadratically with time and declines once the edge of the shell is reached. A density structure, $\rho(r)$, could be found to match any given light curve (Chatzopoulos et al. 2013), but its construction seems artificial. Given the lack of narrow CSM lines in the spectra of common SNe Ib, CSM interaction seems an unlikely estimate for their luminosity excess.

8.5.2. A Magnetar

A significant fraction, substantially more than 10%, of all neutron stars are born with magnetic fields $(0.3\text{–}1) \times 10^{15}$ G (Beniamini et al. 2019). This is roughly consistent with the fraction of core-collapse supernovae that are of Types Ib and Ic. It is thus possible that a substantial fraction of this class of supernovae makes magnetars. In one of the few studies of Type Ib progenitors that included rotation, Yoon et al. (2010) found periods of ~10–20 ms, rapid enough for rotational energy to affect the light curve of a supernova, though not its explosion energy. Loss of the hydrogen envelope diminishes the rotational braking the helium core would have experienced in a red giant, though angular momentum is still lost to winds. The explosion would still be neutrino-powered as calculated here, but the light curve would be dominated by the magnetar.

As an example, consider model He6.0. The unmodified version of this supernova, using the S19.8 central engine, exploded with a kinetic energy of 1.2×10^{51} erg and produced $0.083\, M_\odot$ of ^{56}Ni. Figure 29 shows the effect on the light curve of embedding a magnetar with field strength 5, 7, and 10×10^{14} G and initial rotational energy 2.5, 3.0, and 3.5×10^{49} erg. The prescription for energy deposition here was the same as that of Woosley (2010), which is very similar to that of Kasen & Bildsten (2010) but uses slightly different field strengths to achieve the same luminosity. Energy from radioactive decay was included in the three magnetar models.

The corresponding initial rotational periods are 28, 26, and 24 ms. Other parameters could be chosen to give different peak luminosities and slopes on the tail, but these three peaked near $10^{42.7}\,{\rm erg\,s^{-1}}$, similar to a brighter-than-average SN Ib or Ic (Prentice et al. 2016). This compares with $10^{42.21}\,{\rm erg\,s^{-1}}$ for the same model with no magnetar. The rise time from 50% to peak luminosity ($t_{-1/2}$) for the three models varied from 10.4 to 12.4 days, with the models with greater rotational energy but

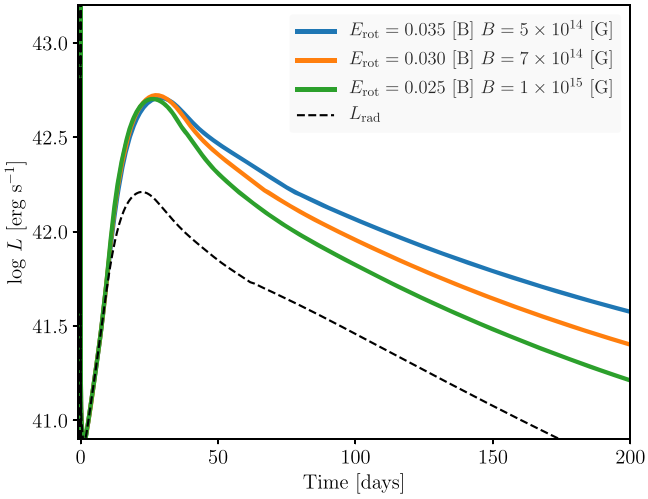

Figure 29. Light curve of model He6.0 with and without a contribution from an embedded magnetar. The dashed black line shows the light curve of the standard model powered only by ^{56}Ni decay. The orange, blue, and green curves show the modification caused by a magnetar with initial rotational energy and magnetic field strength of 2.5×10^{49} erg and 1×10^{15} G (green), 3.0×10^{49} erg and 7×10^{14} G (orange), and 3.5×10^{49} erg and 5×10^{14} G (blue).

weaker magnetic fields rising more slowly. The decline time from peak to 50% of peak luminosity ($t_{+1/2}$) was 19.0–28.5 days for the same models. For the model without the magnetar, the rise and decline timescales were 10.4 and 23.4 days. The ejected mass here was $2.816\, M_\odot$, and the neutron star remnant was $1.417\, M_\odot$ (gravitational). The radioactive contribution came from the decay of $0.084\, M_\odot$ of ^{56}Ni.

The idea that many "normal" SNe Ib and Ic might not be powered at peak by radioactive decay is novel and will have important implications for the role of magnetars in many diverse kinds of supernovae. Since they are much more common than superluminous supernovae and a more regular class of events, they might be a good laboratory for the study of magnetar birth. After 100 yr, the magnetars in Figure 29 would have periods of 1.26, 0.88, and 0.63 s and luminosities of 4×10^{36}, 8×10^{36}, and $1.6 \times 10^{37}\,{\rm erg\,s^{-1}}$, assuming the field strength remains constant.

The tails of the light curves of SNe Ib and Ic might be studied carefully to ascertain ^{56}Ni abundances, but this could be complicated by the fact that gamma rays are already escaping shortly after peak in the radioactive model. For some field strengths, the tail of the magnetar models also declines at a similar rate as the radioactive model (Figure 29). On the other hand, light curves declining slower than the 77.3 day half-life of ^{56}Co, i.e., full gamma-ray trapping, might be indicative of a magnetar energy source. If the iron abundance could be accurately inferred from late-time spectra, the magnetar model predicts a much smaller abundance than needed to explain the brightness of the supernova.

8.6. SNe Ic from More Massive Stars

Helium stars with presupernova masses greater than $6\, M_\odot$ require extraordinary explosion energies or gamma-ray escape to avoid producing light curves that are too faint and broad to be common SNe Ib and Ic (Ensman & Woosley 1988), yet our present formalism predicts many such explosions (Table 5; Figure 3). This is particularly true when the more energetic S19.8 central engine is employed. Figure 30 shows a

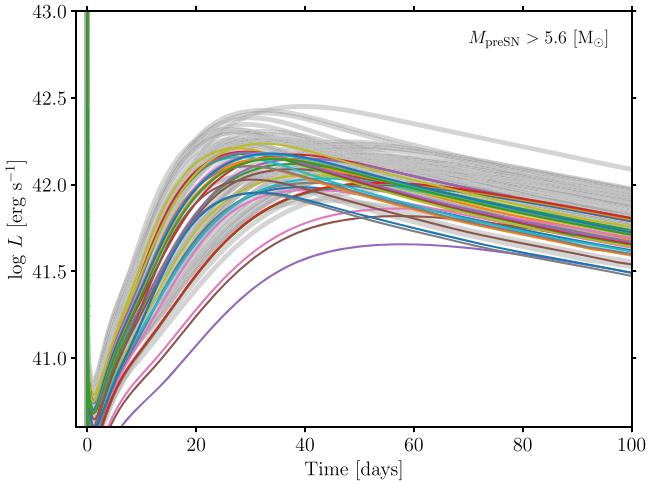

Figure 30. Light curves for the more massive models. The masses displayed have initial helium star masses greater than 8.0 $M_\odot$ and final presupernova masses greater 5.64 $M_\odot$. They correspond to stars with ZAMS masses greater than 30 $M_\odot$. These would be Type Ic, but, if powered only by neutrinos and illuminated only by radioactive decay, they have longer, fainter light curves than common SNe Ic. Colored lines indicate models powered by the W18 central engine, whereas gray lines come from the more energetic S19.8 set, which makes more ^{56}Ni.

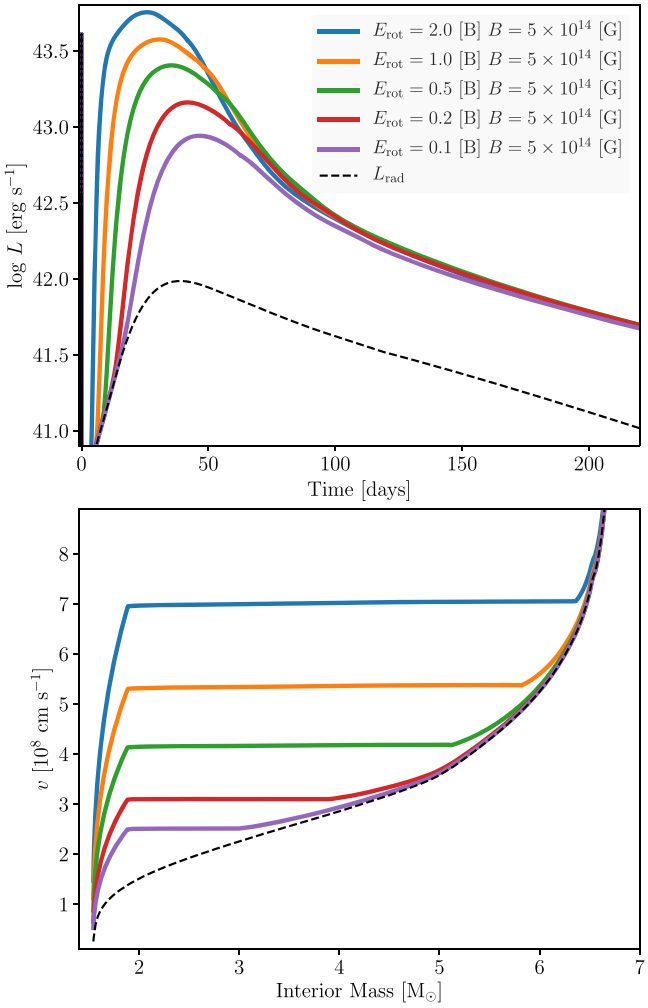

Figure 31. Top: light curves for model He10.00 with and without an embedded magnetar. Because all calculations used the same magnetic field, the light curves converge to similar values at late times. Bottom: terminal velocities for the models in the top panel. Regions of constant velocity reflect the presence of a dense, thin shell containing all that mass. In a multidimensional simulation, these shells would be spread over a larger radius, and some of the magnetar-energized matter would penetrate into the overlying, faster-moving material.

selection of light curves. Though some are as bright as their lower-mass counterparts in Figure 23, the curves all peak appreciably later and decline much more slowly. The decline time to 50% peak luminosity ($t_{+1/2}$) takes more than 40 days for the lightest models in this group and longer for the more massive ones (Table 5). The three broadest, faintest light curves in Figure 30 came from helium stars with initial masses of 19.25, 19.50, and 19.75 $M_\odot$ that had presupernova masses from 10.07 to 10.29 $M_\odot$. These supernovae took 2 months to decline to half their peak luminosity. Their effective temperatures at peak were near 3500 K, so they would be quite red. Since they lost most of their helium prior to dying, these supernovae would probably be Type Ic.

We are not aware of any observed supernovae with these characteristics. Perhaps they have been missed because they are faint, slow, and red, or these massive progenitors, essentially all of the stripped stars with presupernova masses greater than about 6 $M_\odot$, collapsed to black holes. This is an issue that gravitational radiation studies might some day address. Are there indications in the black hole birth function of cores with masses greater than 6 $M_\odot$ exploding and not leaving black hole remnants?

Or, our models may be deficient. It is hard to see how anything other than a major alteration of the neutrino-powered, radioactive-illuminated paradigm could greatly increase the luminosities or decrease the light curves' widths for such massive progenitors. The alterations again include circumstellar interaction or extra energy from a rotationally powered central engine.

In favor of a magnetar explanation is the fact that, faint or not, many of these massive models do explode (Table 5). A successful neutrino-powered explosion during the first second after the iron core collapses facilitates the subsequent formation and operation of a magnetar by evacuating a region around the PNS and allowing it time to cool, contract, and spin up. Since the initial explosion makes only $\lesssim$0.15 $M_\odot$ of ^{56}Ni and the magnetar would make none, the luminosity both at peak and, usually, on the tail would not be due to radioactivity (see, e.g., Woosley 2010), but the iron lines might be strong in the remnant. While the calculation of rotating presupernova models is deferred, we note the tendency of more massive stars, especially those that lose their envelopes early on, to produce rapidly rotating neutron stars (Heger et al. 2005). Most of the angular momentum loss in the core occurs, in single stars, during helium burning, when the star's hydrogen envelope expands to become a giant. The essentially stationary envelope saps angular momentum from the rapidly rotating core, so stars stripped of their envelopes, as these are, end up rotating more rapidly at death.

There are two sorts of magnetar models: those where the magnetar's initial rotational energy is small compared with the kinetic energy of the neutrino-powered explosion and those where it is not. In the former case, the magnetar just illuminates a coasting configuration whose dynamics were determined by the neutrinos. These are the magnetars that were studied in Section 8.5.2. In the latter case, energy input by the magnetar appreciably modifies the velocity profile of the supernova. These two cases are illustrated with models He10.00 (Figure 31) and He19.75 (Figure 32). Both used the W18 explosion model (Table 5) for their initial explosions. Model

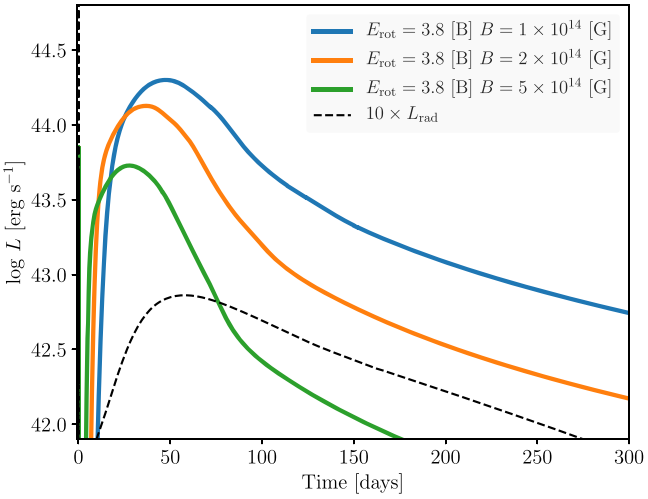

Figure 32. Light curves for model He19.75 with and without an embedded magnetar.

He10.00, which had a presupernova mass of 6.74 $M_\odot$, is a bit heavier than usually deemed responsible for common SNe Ibc. Model He19.75, with a presupernova mass of 10.3 $M_\odot$, was in the island of high-mass explodability in Figure 13 and one of the heaviest models to explode in the current study.

The five magnetars introduced in model He10.00 all had magnetic fields of 5×10^{14} G and rotational energies of 0.1, 0.2, 0.5, 1.0, and 2×10^{51} erg. These rotational energies were chosen to span a range where the rotational energy was either a small or major adjustment to the energy of the neutrino-powered supernova, 7.6×10^{50} erg. Given the single value of the magnetic field considered, the light curves are all very similar on their tails (Figure 31) but vary greatly in peak luminosity and rise time. All are substantially brighter than the purely radioactive case. For the smaller rotational energies, the light curves are similar to those for the lower-mass models (Figure 29) but broader due to the larger mass. They could potentially account for some of the brighter, broader SNe Ib and Ic in Figure 26. For larger magnetic fields, the light curve would decline more rapidly. The light curves in Figure 31 assume the full trapping of the magnetar-deposited energy. Depending on the spectrum of the magnetar and the pulsar wind interaction inside the supernova, a substantial fraction of the energy might escape at late times and not contribute to the optical light curve. The column depths at 200 days for the five magnetar energies shown are 28, 22, 14, 9, and 6 g cm^{-2}. If the opacity were like gamma rays from radioactivity, $\sim$0.05 cm^2 g^{-1}, then the light curve at 200 days for the most energetic case would be about three times fainter. The optical depth at earlier times would scale approximately as t^{-2}.

The light curves for the more energetic cases bear some similarity to SNe Ic-BL. A potential problem with such a scenario, though, is that, except for a small mass near the surface (Figure 31), the velocities are quite low, hence no "broad" lines. Typical SNe Ic-BL are estimated to have velocities characteristic of 4 $M_\odot$ exploding with 7×10^{51} erg with ^{56}Ni masses near 0.3 $M_\odot$ (Taddia et al. 2019), or over 10,000 km s^{-1}. Drout et al. (2011) adopted a velocity of 20,000 km s^{-1} at peak luminosity. Both this extreme energy and mass of ^{56}Ni are well out of reach of our standard models. There are three possible solutions to this difficulty. (1) The masses of SNe Ic-BL may be lighter or their explosion energies greater than considered here. A different explosion mechanism would need to be invoked to raise the energy. (2) The light at peak could come from circumstellar interaction. The outer 0.015 $M_\odot$ of model He10.00 moves faster than 12,000 km s^{-1} and has kinetic energy 3×10^{49} erg, more than enough to provide the entire light curve of most SNe Ic-BL, if the matter interacted with a comparable mass of CSM at a few $\times 10^{15}$ cm. The problems with this scenario are explaining why the necessary CSM is there with the right density distribution to give the observed light-curve shape (Section 8.5.1), and why narrow lines from the CSM are not usually seen in SNe Ic-BL. This may be a more promising model for SNe Ibn (Pastorello et al. 2016; though typical "broad-line" components are slower for this class). (3) The light curve and most of the explosion energy could come from a magnetar or accretion into a black hole. The explosion would then probably be asymmetric.

Also shown in Figure 31 are the velocity profiles resulting from the various magnetars. If plotted versus radius instead of mass, the regions of near-constant coasting speed would show up as thin, dense shells. For large magnetar energy and 1D simulations, most of the mass of the explosion is piled up in this thin shell. That the shell is thin and dense is an artifact. In a multidimensional simulation, the hot pulsar wind for the more energetic magnetars would break through the slower-moving denser material outside (Chen et al. 2016) and surround the supernova with an envelope of faster-moving material. The explosion would be asymmetric. The problem here is that a definitive calculation of the spectrum is difficult. At late times, the typical velocities would be slower, more like the broad flat spots in Figure 31. Velocities of 4000–5000 km s^{-1} are typical of some long duration Type Ic super luminous supernova (SLSN; Jerkstrand et al. 2017) and may be similar to what is seen in some SNe Ic-BL. Maurer et al. (2010) found that the velocities for SNe Ic-BL are highly variable and might depend on observing angle. They derived an average of about 6000 km s^{-1}.

As a second example, consider model 19.75. Without a magnetar, this model exploded, using the W18 central engine, with a terminal kinetic energy 8.4×10^{50} erg and ejected 0.088 $M_\odot$ of ^{56}Ni. The presupernova mass was 10.28 $M_\odot$, of which 8.5 $M_\odot$ was ejected. Only 0.25 $M_\odot$ of that was helium. This would have been a SN Ic. The original ZAMS mass of the star before it lost its envelope in the binary would have been 51 $M_\odot$. This explosion was recomputed with an embedded magnetar with an initial rotational energy of 3.8×10^{51} erg (rotational period 2.3 ms) and magnetic field strengths of 1, 2, and 5×10^{14} G. Energy deposition was calculated according to Woosley (2010), and full absorption was assumed. The case with the smallest field strength is similar to magnetar parameters used by Vreeswijk et al. (2017) to fit the Type I SLSN iPTF12dam and is rather typical of the large spread observed in SLSN (Nicholl et al. 2017; Villar et al. 2018). Figure 32 shows the light curves both with and without the magnetar. With the magnetar, the model essentially replicates the results of Vreeswijk et al. (2017) and observations of iPTF12dam. As noted by those authors, the magnetar model, even with some approximation for escape, is too bright at very late times compared with the observations, but magnetar energy transport and breakout are poorly understood. The improvement here over Vreeswijk et al. (2017) is that the explosion is derived from an actual stellar evolution and explosion calculation.

The light curve shown in Figure 32 might also rise more rapidly than would actually be observed in the optical because the magnetar pushes the ejected matter into a thin shell that has an unphysically short diffusion time. The bolometric light curve also peaks earlier than the optical light curve because of its high effective temperature (Nicholl et al. 2017).

9. Conclusions

Using an approach to the explosion physics similar to that previously used to study single massive stars (Sukhbold et al. 2016), we have modeled the explosion of mass-losing helium stars. Presupernova models are taken from Woosley (2019). It is assumed that the initial helium star is revealed in a close, mass-exchanging binary system when the star loses its entire envelope just prior to or shortly after central helium ignition. While simplistic, the models capture an essential aspect of stripped star evolution. The helium core and its central convection zone shrink during helium burning due to mass loss, while in single stars, the helium core grows due to hydrogen shell burning. Because the helium core shrinks rather than growing, the main-sequence masses producing supernovae in binary systems are typically greater, and their lives are shorter than for single stars.

As in Sukhbold et al. (2016), an explosion is not artificially forced but a consequence of presupernova structure and the choice of a "central engine." A realistic, albeit 1D and parameterized, calculation of neutrino transport is done for each explosion. Several central engines of various strengths were explored with parameters calibrated to SN 1987A or the Crab Supernova. The standard choice was a combination of the W18 engine for helium stars with final presupernova masses above about $3.5\,M_{\odot}$ and an engine interpolating between W18 and Z9.6 for stars with smaller final helium core masses. See Sukhbold et al. (2016) for a discussion of these engines. Here W18 was calibrated against SN 1987A and Z9.6, the Crab. The effects of varying the mass-loss rate for the presupernova stars were also explored. A more energetic central engine, S19.8, was also extensively explored to test the limits of ^{56}Ni production.

Despite being derived from main-sequence stars with larger masses, the compact remnant masses, ^{56}Ni yields, and explosion energies for simulated binaries are very similar to single stars with a helium core mass equal to the presupernova mass of the stripped star (compare Figures 5 and 7 with Figures 34 and 35 in Appendix A). This did not have to be so. The compositions, entropies, and compactness parameters are different in the two sets. The stripped stars in the present study explode a bit more frequently with a bit more energy, but for those that explode, the observable outcomes are robust. This implies that the iron core masses and gradients just outside those cores are set to first order by the final mass of the helium and heavy-element core and only to second order by how that core came to exist.

Except for a few cases with the weakest central engine, stars with presupernova masses from 2.1 to $6.5\,M_{\odot}$ explode robustly (Figures 4 and 5). For final masses between 6.5 and $12\,M_{\odot}$, the results are more nuanced, with a mixture of black holes and neutron stars sensitive to the explosion model. Presupernova masses up to $8\,M_{\odot}$ mostly explode, and there is also an island of explosions centered around $10.5\,M_{\odot}$ that grows with the relative strength of the central engine. Black holes are invariably produced for presupernova masses around 8–9 $M_{\odot}$ and above $12\,M_{\odot}$. These outcomes correlate strongly with both the compactness parameter and Ertl parameterization of the presupernova stars (Figure 12).

Similar systematics were seen for single stars (Sukhbold et al. 2016, 2018) but with a shift upward in the presupernova mass scale for the more massive helium star models of about $2\,M_{\odot}$ (Figure 12 here and Figure 10 of Woosley 2019). This shift is partly due to a higher mass fraction of carbon following helium burning in the mass-losing helium stars. The results will presumably also be sensitive to the rate for $^{12}\mathrm{C}(\alpha,\,\gamma)^{16}\mathrm{O}$, though we have not yet undertaken a sensitivity study. They are also a consequence of the different placement of interfering convective shells and a larger CO core for a given helium core in the mass-losing stars (e.g., Sukhbold & Adams 2020).

No final kinetic energy greater than 2.0×10^{51} erg was found in any model. Combined with our previous results in Sukhbold et al. (2016), we think this represents a fundamental upper limit to what can be obtained with neutrino-energy input alone, at least for the physics in our 1D models and assuming that SN 1987A was a neutrino-driven explosion. Other similar studies support this conclusion (Müller et al. 2016; Ebinger et al. 2019). Pejcha & Thompson (2015) used a parameterized prescription of a neutrino-driven wind and obtained explosions up to $\sim 6 \times 10^{51}$ erg. Though their estimated ^{56}Ni masses were similar to our results, our smaller limit may be more realistic because of a more physical treatment of neutrino transport. Multidimensional simulations with neutrino transport and parametric luminosities of the neutron star (Scheck et al. 2006), as well as self-consistent neutrino transport (e.g., Fryer & Kalogera 2001; Bruenn et al. 2016; Müller et al. 2017), have never produced neutrino-driven explosions with converged energies above $\sim 2 \times 10^{51}$ erg.

Remnant masses were determined for neutron stars produced in the successful explosions and black hole masses for the failures. These are particularly appropriate for binaries where most masses are measured and for gravitational radiation signals. For the standard W18 engine, black holes formed in 21% of collapses, and the median neutron star gravitational mass was $1.351\,M_{\odot}$ when the mass decrement due to neutrino losses was calculated self-consistently using P-HOTB (Table 3; Figure 16). The mean value was $1.371\,M_{\odot}$. Slightly larger values were obtained using the Lattimer & Prakash (2001) prescription for the gravitational mass correction. The values derived using the Lattimer–Prakash correction are very similar to what was obtained for equivalently modeled single stars by Sukhbold et al. (2016), $1.40\,M_{\odot}$. Other average values are given in Table 3, and the predicted distribution functions are given in Figures 16 and 17.

Since there is some disagreement in the literature (Belczynski et al. 2012; Kreidberg et al. 2012), we want to emphasize that we have no problem producing low-mass black holes right down to the maximum neutron star mass (Section 6.2). These low-mass black holes are made by fallback in a partially successful explosion. There is a deficiency of black holes below $6\,M_{\odot}$ (Figure 17) because that is the lowest-mass black hole produced by prompt implosion, but there is no empty "gap." On the other hand, our calculations do show the possibility of a gap at an unexpected location, around 10–11 $M_{\odot}$. The width and significance of this void is model-dependent (Figure 3). It is broader for central engines with greater power. Its presence would reveal some dependency of the explosion energy on the compactness of the presupernova star and hence its shell-burning

history. For presupernova masses above $12\,M_{\odot}$, all models produced black holes with masses nearly equal to their presupernova mass. This resulting distribution function is thus sensitive to the treatment of mass loss, and hence metallicity, and will be explored further in a future paper.

Because of its importance to the light curves of SNe I, particular attention was paid to ^{56}Ni synthesis. Using the same approach as in Sukhbold et al. (2016), similar average yields were found. The IMF-averaged ^{56}Ni production (Ni+Tr) per supernova for our standard W18 engine was $0.054\,M_{\odot}$. In 2016, it was $0.053\,M_{\odot}$. For the most energetic S19.8 engine, the value rises to $0.068\,M_{\odot}$. These values are all skewed toward low values by the large contribution of low-mass supernovae to the number statistics. The possibility of producing larger values was explored (Sections 3.3 and 8.5). Taking liberal estimates for ^{56}Ni production by α-recombination in the neutrino-powered wind and assuming that most of the iron-group isotopes, even in deep layers that experience neutrino interactions, are ^{56}Ni, these yields can be increased to 0.073 and $0.090\,M_{\odot}$ per supernova for the W18 and S19.8 engines. This liberal estimate corresponds to assuming that 75% of all material that achieves NSE in the neutrino-transport calculation using P-HOTB is ejected as ^{56}Ni. This is our upper bound. Still greater values exceed the reasonable error bar for neutrino-powered explosions but are possible if greater energies and deeper mass cuts are forced in the explosion. The greatest ^{56}Ni observed in any calculation, even with unrealistic, artificial variation of these parameters, especially the mass cut, was $0.33\,M_{\odot}$ (Section 8.5).

Placing the mass cut that close to the edge of the iron core seems to be ruled out, though, since it would imply a median gravitational mass for the neutron star of only $1.28\,M_{\odot}$ (Table 3). What is added to ^{56}Ni gets subtracted from the remnant mass. It is thus very difficult to reconcile ^{56}Ni yields of $0.2\,M_{\odot}$ (Drout et al. 2011; Taddia et al. 2019) and more with observations, even for models with additional (nonneutrino) energy sources. Doubling the iron yield of massive stars would also mean that they account for most of the iron seen in the Sun. This would be inconsistent with observations showing that the majority of iron has been created later in the history of the Galaxy by SNe Ia (Section 5). It would also grossly overproduce the ^{56}Ni observed in SN 1987A.

Ordinary SNe Ib and Ic are attributed here to models with final masses between 2.45 and $5.63\,M_{\odot}$, which, depending on uncertain mass-loss rates, correspond to initial helium star masses of 3.0–$8.0\,M_{\odot}$. This is for the (possibly conservative) estimates of mass-loss rate employed. These, in turn, correspond to main-sequence masses of 15–$29\,M_{\odot}$. These supernovae come from a population that, on average, is more massive than SNe IIp. They may thus be found more tightly correlated with star-forming regions (Maund 2018). The range of ages for 15–$29\,M_{\odot}$ stars is $10^{7.12}$–$10^{6.81}$ yr (Sukhbold et al. 2018). Maund gave typical ages of $10^{7.05}$ and $10^{6.57}$ yr for Types Ib and Ic, respectively. More massive, shorter-lived stars will also produce SNe Ic if the mass-loss rates are greater, but the presupernova mass should not exceed $12\,M_{\odot}$ (Section 6.2). For the standard mass-loss rates, the ZAMS mass corresponding to a $12\,M_{\odot}$ progenitor is $57\,M_{\odot}$. Such a star would have a lifetime of $10^{6.62}$ yr, though at a very high mass, the lifetime becomes insensitive to the mass. There should be a tendency, however, for the highest-mass models to produce faint, broad light curves (Ensman & Woosley 1988) unless the explosion energy is much greater than calculated here. The maximum luminosity of a Type Ib or Ic progenitor star is $10^{5.6}\,L_{\odot}$. Brighter progenitors are over $12\,M_{\odot}$ and collapse to black holes (Section 6.2) or explode using energy sources in addition to neutrinos from core collapse.

Using our most optimistic but plausible ^{56}Ni abundances, $0.75\times$ (Ni+Tr+α) (Section 3.3), reproducing the light curves of the brighter common SNe Ib and Ic is problematic. Using the standard W18 central engine, it is possible to reproduce the light-curve peak luminosity and rise and decline rates for events with peak luminosities below the averages quoted by the observers (Figure 23), but not for any with peak luminosities in excess of $10^{42.5}$ erg s^{-1} (Figure 26). Using our most energetic central engine, S19.8, only raises this limit to $10^{42.6}$ erg s^{-1}, and these upper limits are only achieved in a few cases (Table 5). For ^{56}Ni yields evaluated more conservatively, like in Sukhbold et al. (2016), the upper bound for the W18 central engine falls to $10^{42.1}$ erg s^{-1}, and most observed SN Ib and Ic luminosities cannot be achieved. Our medians are, of course, lower than these peak estimates with a value of $10^{42.0}$–$10^{42.3}$ erg s^{-1} typical for the full range of stars that make SNe Ib and Ic (3–$8\,M_{\odot}$; Table 8). The upper limit comes from using the energetic S19.8 central engine and evaluating the ^{56}Ni yield optimistically. The lower value is for the W18 central engine with ^{56}Ni yields evaluated conservatively.

Many supernovae classified by the observers as ordinary Type Ib and Ic are simply too bright to be made by our unassisted neutrino-driven models. There are several ways out of this dilemma, but we have argued that simply increasing, without bound, the mass of ^{56}Ni ejected in the explosion violates several basic constraints (Sections 5, 6.1, and 8.5). Maybe our simple calculation of light curves using single-temperature flux-limited diffusion in *KEPLER* is inadequate to capture the peak of the light curve. We expect that studies in the near future will address this issue. Maybe the observed brightness distribution for SNe Ib and Ic (e.g., Lyman et al. 2016; Prentice et al. 2016; Anderson 2019) will drift downward in the future (e.g., Prentice et al. 2019). A more careful treatment of, e.g., bolometric corrections or Malmquist bias might lead to a significant decrease in published mean values. Or, a significant fraction of what the observers have called SNe Ib and Ic, the brightest ones, have a nonradioactive power source at their peak. We explored the possibilities.

Circumstellar interaction is one way to boost the luminosity and must play a role in some rare forms of SNe I, e.g., Type Ibn (e.g., Pastorello et al. 2008), but it requires fine-tuning of the CSM distribution to mimic the light-curve shape of an ordinary SN Ic. If the light were produced by a small mass of high-velocity material with slow-moving presupernova mass loss, there would presumably be spectroscopic signatures that are not reported. There might be a superposition of high- and low-velocity lines.

If radioactivity and circumstellar interaction are ruled out, the remaining possibility is magnetars. Given the great diversity of SNe I in nature, including SLSN, SNe Ic-BL, and gamma-ray bursts, it is clear that some other source besides ^{56}Ni does, at least occasionally, provide the light of SNe I, and magnetars are frequently invoked. Might they also contribute, at a reduced level, to ordinary events? The energy and field requirements are modest, less than 10^{50} erg (corresponding to neutron star birth rotation periods longer than 14 ms) and greater than 5×10^{14} G. The explosion is still neutrino-

powered, but the light both at peak and on the tail comes, at least partly, from the magnetar. Distinguishing characteristics besides the presence of a magnetar in the remnants of known supernovae of Type Ib and Ic would be light curves that declined slower on the tail than ^{56}Co decay or evidence for a smaller abundance of ^{56}Fe and ^{56}Co in the late-time spectrum than necessary to explain the peak of the light curve. Energetic magnetars might be easier to make in binaries, since removing the envelope removes a large sink for the angular momentum of the rapidly rotating helium core. Most angular momentum in the evolution of a single star is lost between hydrogen depletion and helium ignition (Heger et al. 2005) as the star becomes a red supergiant. Removing the envelope would diminish this braking. If they were present in SNe IIp, magnetars of the sort proposed here would have little influence on the light curve except at very late times. The energy that they deposit would be adiabatically degraded during the expansion while on the plateau.

Outside of the mass range that we attribute to normal SNe Ib and Ic, unusual events are predicted. Lower-mass models with presupernova masses less than 2.59 $M_\odot$ coming from initial helium stars with masses 2.5–3.2 $M_\odot$ have distinctive properties. For helium star masses below 3.0 $M_\odot$, the presupernova star is a helium blue supergiant, not a WR star. Following explosion, the expansion and recombination of this envelope produce a broad bright blue initial peak before declining and, depending on the ^{56}Ni yield, rising again later to a second (radioactive) peak (Figure 21). Given their small ejecta masses, the models have high velocities even though their kinetic energies are low. Some subset might be fast blue optical transients (Kleiser et al. 2018; Woosley 2019), SN 2014ft–like objects (De et al. 2018), SNe Ibn, or even SNe Ic-BL. Supernovae in this mass range may also be complicated by the effects of a degenerate silicon flash weeks to months before iron core collapse. If the flash is strong and substantial material is ejected, depending on the time of the ejection, the supernova could be very bright (Figure 22), like some SNe Ibn (Pastorello et al. 2008). If the silicon flash is weak, though, they would look more like ordinary faint SNe Ib (3.0, 3.1, and 3.2 $M_\odot$; Figure 23) or supernovae with radius expansion (2.5 $M_\odot$; Figure 21). The specific masses and strengths of the flashes here are sensitive to uncertain flame physics during the silicon flash.

Presupernova models more massive than about 6 $M_\odot$ produce light curves that are too faint and broad to be common SNe Ib and Ic if neutrinos are the cause of their explosion and radioactivity is their only illuminating power. Perhaps most of these collapse to black holes. Others may simply have escaped detection, since their light curves are both red and faint. Ultimately, gravitational wave surveys will offer some constraints.

Some of them might harbor more energetic magnetars, though with similar field strengths to that needed for common events but faster initial rotation rates. Figures 31 and 32 show some possibilities. It is important that neutrinos alone can explain the initial explosion of such stars, if not their light curves. A successful explosion allows the necessary time for the PNS to contract, speed up, and develop a strong magnetic field. The magnetar energy input can either be a small fraction of the final kinetic energy of the supernova or the dominant contributor. In the latter case, pulsar wind breakout might lead to asymmetric ejecta and poking holes in the slower-moving ejecta, possibly contributing to the high-velocity material present in the spectra of SNe Ic-BL. Alternatively, SNe Ic-BL could be lower-mass stars in which circumstellar interaction is important. If a magnetar is powering both the explosion and the light curve, one might expect there to be a correlation between peak luminosity and velocity (Figure 31), though mass is clearly an important second parameter.

We thank the anonymous referee for useful suggestions. We also thank Simon Prentice for providing light-curve data and Bernhard Müller for feedback. T.E. and H.T.J. thank G. Stockinger for the improved treatment of energy transfer by neutrino–nucleon scattering in the neutrino-transport solver, A. Menon and A. Heger for providing the data of their SN 1987A binary progenitors, and R. Hix and F.-K. Thielemann for the NSE solver introduced into P-HOTB by K. Kifonidis. At UCSC, this work was supported by NASA (NNX14AH34G). At Garching, funding by the European Research Council through grant ERC-AdG No. 341157-COCO2CASA and the Deutsche Forschungsgemeinschaft through grants SFB-1258 "Neutrinos and Dark Matter in Astro- and Particle Physics (NDM)" and EXC 2094 "ORIGINS: From the Origin of the Universe to the First Building Blocks of Life" is acknowledged. T.S. was supported by NASA through NASA Hubble Fellowship grant No. 60065868 awarded by the Space Telescope Science Institute, which is operated by the Association of Universities for Research in Astronomy, Inc., for NASA, under contract NAS5-26555.

Appendix A
Improved Single-star Results

A number of improvements have been made to the P-HOTB code since its use in Sukhbold et al. (2016). They chiefly concern the treatment of neutrino–nucleon scattering in the transport solver, the inclusion of weak decays for ^{56}Ni and ^{56}Co, and some some refinements to the treatment of the radial grid (Section 3.1). In this appendix, we briefly explore the results of core-collapse and explosion simulations when the improved code is applied to the same single-star progenitors investigated by Sukhbold et al. (2016). Generally, the differences are small.

Table 9 gives some basic results for the supernova, neutrino, and remnant properties of the SN 1987A and Crab progenitors employed as calibration models in both papers. The results from the previous version of the P-HOTB code ("old") are taken from Sukhbold et al. (2016), and the simulations with the upgraded code version ("new") were performed with exactly the same values of the engine parameters as used in Sukhbold et al. (2016; see Table 3 there). The differences between old and new simulations are minor. The time the explosion sets in can be slightly different, both earlier or later by some 10 ms. The explosion energy with the new code is ∼3%, up to ∼15% (for W20 and Z9.6) greater, but can also be marginally smaller (W18). Interestingly, the ejected mass of ^{56}Ni is reduced, but the ejecta mass of the tracer nucleus ($M_{\rm Tr}$) is increased by roughly the same amount, so the sum remains nearly unchanged. Similar small differences are found in the masses of the neutrino wind and the final neutron star mass. The latter is slightly lower when the explosion with the new code starts earlier and slightly higher when the explosion sets in later. The small differences in these results are a consequence of opposite trends in different neutrino quantities. With the improved

Table 9
Results from Sukhbold et al. (2016; "Old") for All Neutrino Engines Applied to SN 1987A and Crab Calibration Models, Compared to Simulations with the Upgraded P-HOTB Code ("New")

Calibration Model	t_{exp}[a] (ms)	E_{exp}[b] (B)	E_{exp}/M_{ej}[c] (B/$M_\odot$)	$M_{^{56}Ni}$[d] ($M_\odot$)	M_{Tr}[e] ($M_\odot$)	M_{NS}[f] ($M_\odot$)	M_{wind}[g] ($M_\odot$)	M_{fb}[h] ($10^{-2}\,M_\odot$)	$t_{\nu,90}$[i] (s)	E_{ν}tot[j] (100 B)
S19.8[k] old	750	1.30	0.100	0.072	0.034	1.551	0.096	0.00298	3.78	3.58
S19.8[k] new	790	1.34	0.103	0.052	0.046	1.560	0.089	0.00409	3.61	3.64
W15 old	580	1.41	0.103	0.045	0.046	1.317	0.088	0.00018	3.53	2.67
W15 new	550	1.44	0.105	0.040	0.051	1.315	0.084	0.00060	3.19	2.60
W18 old	730	1.25	0.081	0.056	0.036	1.484	0.081	0.00310	3.57	3.22
W18 new	730	1.23	0.080	0.044	0.043	1.489	0.083	0.00444	3.54	3.21
W20 old	620	1.24	0.070	0.063	0.027	1.562	0.089	0.00168	4.15	3.50
W20 new	580	1.43	0.080	0.049	0.046	1.543	0.103	0.00259	3.94	3.49
N20 old	560	1.49	0.100	0.036	0.052	1.549	0.117	0.00243	3.47	3.38
N20 new	560	1.59	0.107	0.032	0.057	1.543	0.123	0.00290	3.27	3.34
Z9.6 old	155	0.165	0.020	0.006	0.006	1.338	0.019	0.00016	7.03	1.82
Z9.6 new	145	0.190	0.023	0.003	0.010	1.335	0.020	0.00008	7.03	1.83
SN 1987A–like explosions with upgraded P-HOTB and different engines for binary progenitors of Menon & Heger (2017)										
M16+7b (W20)	490	1.49	0.073	0.051	0.051	1.474	0.110	0.00250	3.88	3.23
M16+4a (W18)	923	1.22	0.070	0.068	0.030	1.751	0.067	0.00517	3.60	4.19
M16+4a (W15)	893	1.22	0.070	0.071	0.031	1.745	0.078	0.00523	3.53	4.04
M15+8b (W20)	481	1.38	0.065	0.038	0.049	1.378	0.087	0.00164	3.83	2.86
M15+7b (S19.8)	994	1.00	0.052	0.039	0.030	1.695	0.085	0.00212	3.71	4.09

Notes.
[a] Post-bounce time explosion sets in (i.e., when the shock expands beyond 500 km).
[b] Final explosion energy (with the binding energy of the progenitor star taken into account; 1 B = 1 bethe = 10^{51} erg).
[c] Explosion energy divided by the final ejecta mass (with fallback taken into account).
[d] Ejected ^{56}Ni mass (with fallback taken into account).
[e] Mass of neutron-rich tracer nucleus ejected in neutrino-heated matter with neutron excess (with fallback taken into account).
[f] Final baryonic neutron star mass (with late-time fallback included).
[g] Neutrino-driven wind mass measured by mass between gain radius at t_{exp} and preliminary mass cut before fallback.
[h] Fallback mass.
[i] Emission time of 90% of the total radiated neutrino energy.
[j] Total radiated neutrino energy (at 10 s after bounce, when typically ∼99% of the neutrino energy has been radiated).
[k] Red supergiant progenitor from Woosley et al. (2002).

neutrino treatment, the radiated ν_e luminosity decreases by ∼5%–10%, but the mean energy of the emitted $\bar{\nu}_e$ increases by roughly 1 MeV. The first effect decreases the postshock heating by electron neutrinos, whereas the second effect increases the heating by electron antineutrinos. Depending on which effect dominates, the explosion can commence slightly later or earlier.

The total energy radiated in neutrinos within 10 s of post-bounce evolution is nearly identical in the old and new runs, as is the time $t_{\nu,90}$ over which 90% of this energy is radiated. The reason for the near-equality of old and new results of these quantities is the fact that the luminosity of heavy-lepton neutrinos and antineutrinos increases by essentially the same amount as the ν_e luminosity drops. The only quantity in Table 9 that shows a significant difference is the fallback mass, M_{fb}, which is greater in the new simulation runs by several tens of percent up to a factor of 3 (for model W15), except for model Z9.6, where it is smaller by a factor of 2. However, these differences are only affecting small quantities. The fallback masses are only between about 10^{-4} and some $10^{-3}\,M_\odot$. The larger fallback masses seem to be connected to our tracking of the neutrino emission and neutrino-driven wind of the PNS for only 10 s after core bounce in the new simulations instead of 15 s in the old models. This reduces the push of the neutrino wind on the inner ejecta and leads to some increase of the fallback. However, both the neutrino emission and the wind were artificially enhanced in the old simulations at late times. The improved transport treatment and the new adaptive mesh refinement in the PNS surface layers allow for a higher accuracy with the upgraded P-HOTB code also at late times after bounce. The new models show that at times later than 10 s, the neutrino luminosities are very low and the neutrino-driven wind is correspondingly weak, so that a termination of the neutrino modeling is justified. We therefore consider the new results as more reliable.

In the bottom part of Table 9, we also present results obtained for some of the recent binary progenitor models of SN 1987A from Menon & Heger (2017). For all listed cases, we could find an engine calibration (named by the single-star progenitor of SN 1987A in parentheses after the name of the binary model) for which the explosion energy and nucleosynthesized mass of Ni+Tr/2 are roughly compatible with those of SN 1987A. Application of other engines to the binary models, in particular those of the single-star progenitors N20 and S19.8, leads to overestimated explosion energies and nickel masses compared to SN 1987A. Only binary model M15+7b is harder to explode, and even our strongest single-star engine, S19.8, is able to produce explosion results that are only marginally consistent with SN 1987A. Therefore, because the binary progenitors explode with SN 1987A–like properties for our single-star engines, we can consider them as variants of the already large range of SN 1987A engines applied in the present paper and in Sukhbold et al. (2016) and Ertl et al. (2016a).

Figure 33 gives an overview of the outcome of our simulations with the upgraded P-HOTB code compared to

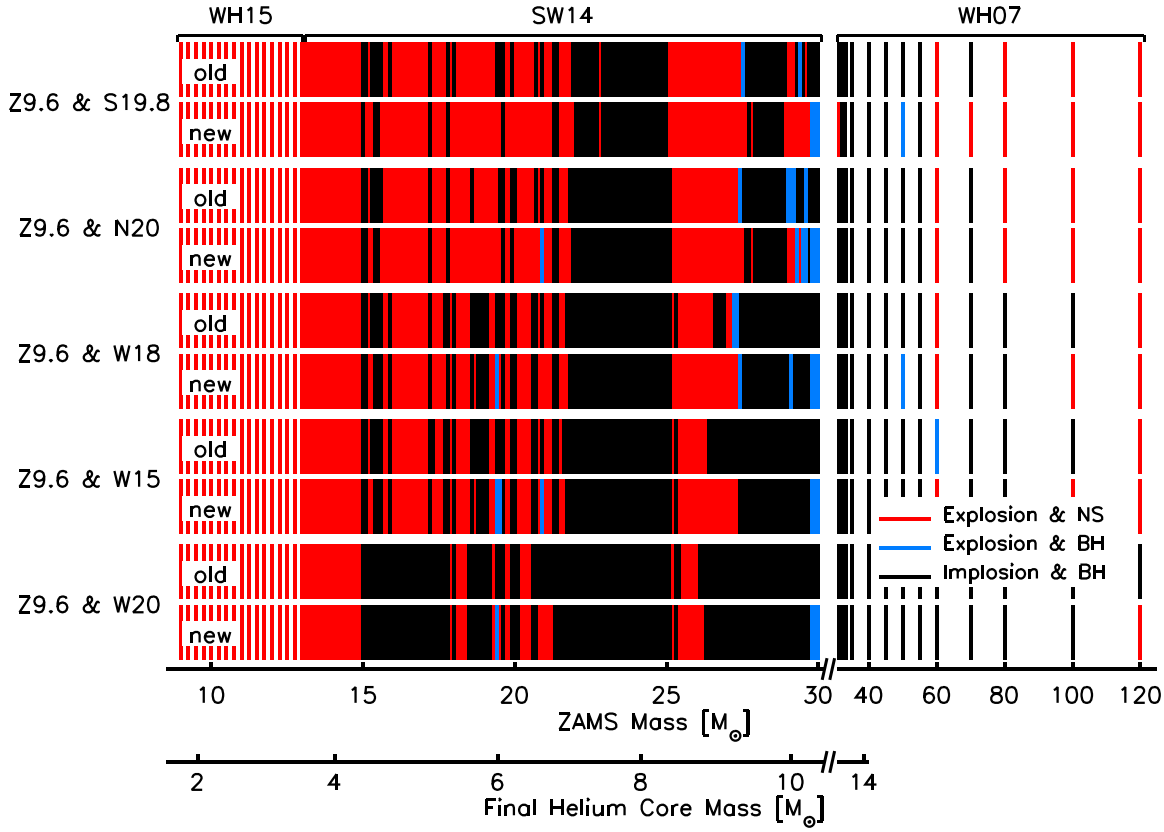

Figure 33. Outcomes of stellar core collapse for five different neutrino engines applied in 1D simulations of the whole set of single-star progenitors investigated by Sukhbold et al. (2016). The engines are sorted by strength (measured by the number of successful explosions) from top to bottom. The results with the P-HOTB code version used by Sukhbold et al. (2016) are labeled "old," and the models recomputed with the upgraded P-HOTB version used in the present work are labeled "new." The different engines are named by the combination of Crab- and SN 1987A–like progenitors used for calibrating the neutrino-engine parameters. Cases of supernova explosion and neutron star formation are marked in red, cases of black hole formation without explosion in black, and cases of supernova explosion and black hole formation by massive fallback ("fallback supernovae") in blue. We set the limit of black hole formation at a baryonic mass of 2.75 $M_\odot$, corresponding to a gravitational mass of about 2.18–2.30 $M_\odot$ (Lattimer & Prakash 2001). Compact remnants whose mass is pushed by fallback above this limit are considered black holes.

the previous results of Sukhbold et al. (2016) for the whole set of single-star progenitors considered there. Results for all five central engines are shown. Red means supernova explosions with neutron star formation, black marks black hole formation with no explosion, and blue indicates fallback supernovae where the outer part of the star is ejected while massive fallback of inner stellar shells lifts the newborn neutron star beyond the mass limit for black hole formation. The corresponding supernova is most of the time fairly weak, and, at least in 1D, no ejection of radioactive nickel is expected.

In the present paper, we assume that neutron stars collapse to black holes when their baryonic mass exceeds 2.75 $M_\odot$, which corresponds to a gravitational mass of ∼2.18–2.30 $M_\odot$ according to Equation (36) of Lattimer & Prakash (2001) for neutron star radii between 9 and 12 km. This limiting mass for cold neutron stars is roughly compatible with estimates derived from the gravitational wave and kilonova observations of the first detected binary neutron star merger, GW170817 (see, e.g., Margalit & Metzger 2017; Rezzolla et al. 2018). For the old simulations of Sukhbold et al. (2016), we did not have to assume any such mass limit for neutron stars, because the progenitors either exploded and formed neutron stars with baryonic (gravitational) masses below 2.15 $M_\odot$ (∼1.8 $M_\odot$) or either continuous or fallback accretion increased the baryonic mass of the compact remnant well beyond 3 $M_\odot$, clearly classifying it as a black hole. In the simulations with the upgraded P-HOTB code, we obtain, for all single-star simulations with all employed central neutrino engines, a few cases where fallback brings the baryonic remnant mass between 2.5 and 3 $M_\odot$, namely one near 2.5 $M_\odot$ (for the N20 engine), one just above 2.75 $M_\odot$ (for engine W15), and two close to 3.0 $M_\odot$ (one for W15 and one for N20). The first two cases may be disputable as being either a neutron star or a black hole; the last two cases are most likely black holes.

Comparing the "landscapes" of the old and new simulations in Figure 33, it is obvious that the patterns with mass intervals of explosions and neutron star formation alternating with mass intervals of failed explosions and black hole formation remain essentially unchanged when applying the upgraded version of P-HOTB. However, we see that some black hole–forming cases in the old simulations explode now with the new code, forming either neutron stars or fallback black holes. Similarly, some fallback supernovae in the old runs convert to explosions with neutron star formation in the new models. These changes occur mostly near the boundaries between mass intervals of exploding and nonexploding cases or for progenitors that formed islands of successful explosions or failures as single, isolated cases. This suggests that progenitors that marginally

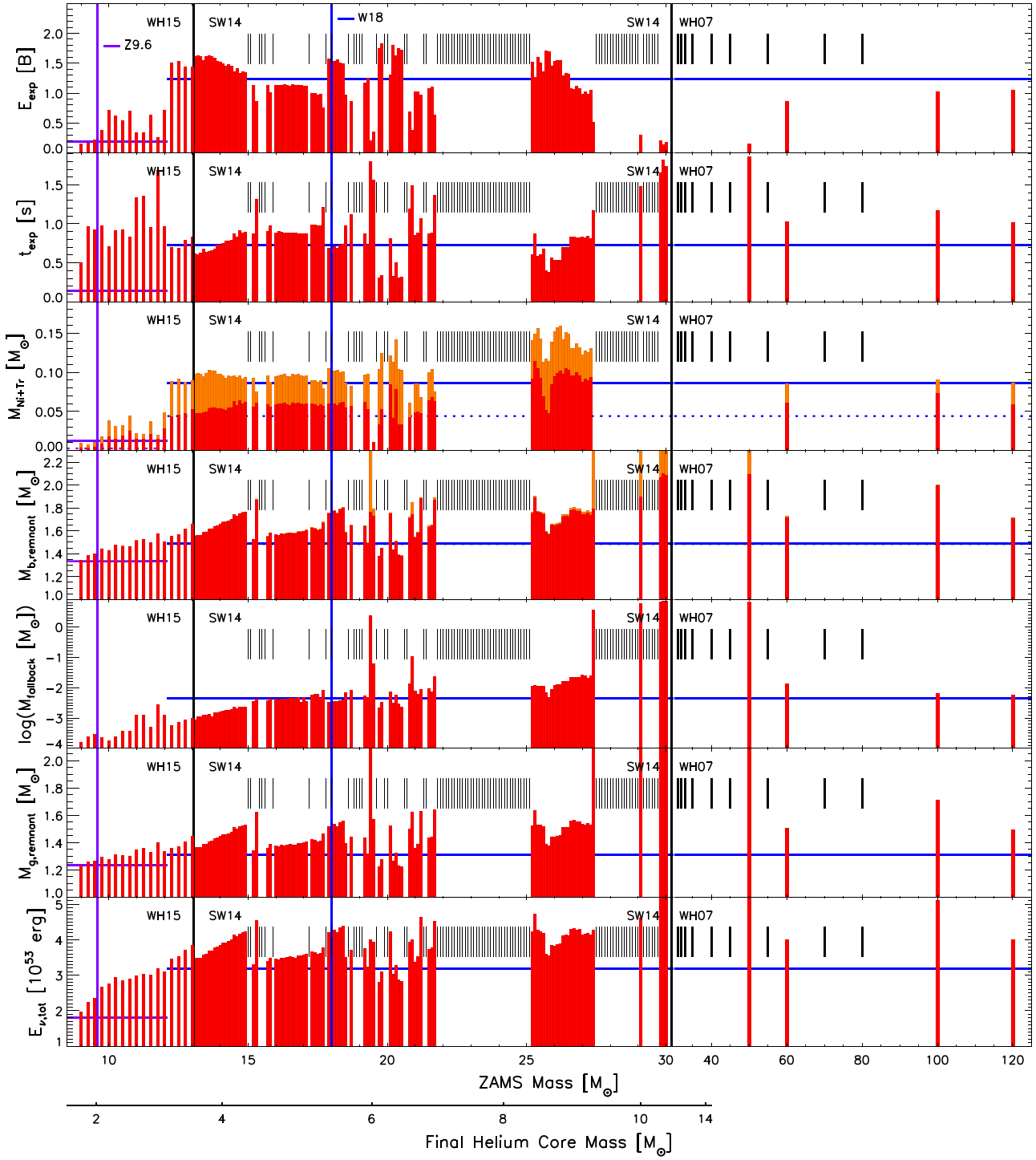

Figure 34. Explosion properties for all single-star, solar-metallicity progenitors of Sukhbold et al. (2016), computed with the upgraded P-HOTB code and the combined Z9.6 and W18 neutrino engine. The plot can be directly compared with Figure 8 of Sukhbold et al. (2016). From top to bottom the panels show the final explosion energy (1 B = 10^{51} erg); the time of onset of the explosion (when the supernova shock expands beyond 500 km); the summed mass of the finally ejected ^{56}Ni (red) plus tracer (orange); the baryonic mass of all neutron stars that exist at least transiently, with the fallback mass indicated by orange extensions on the histogram bars; the logarithm of the fallback mass; the gravitational mass of the compact remnants, most of which remain neutron stars, except the cases with more than 1 $M_\odot$ of fallback, which are expected to become black holes; and the total energy radiated in neutrinos, which we determine only from the PNS cooling phase without taking into account possible neutrino emission during fallback accretion (for better comparison with Sukhbold et al. 2016). In contrast to Figure 8 of Sukhbold et al. (2016), where the neutrino radiation loss was shown for a post-bounce evolution of 15 s, the current models have been simulated only for 10 s after bounce. The differences in the neutrino-energy loss would not be visible on the scale of the plot. Nonexploding cases are marked by thin, short vertical black dashes in the upper part of each panel. The thick vertical black lines separate the different sets of single-star progenitor models investigated by Sukhbold et al. (2016); the vertical purple and blue lines mark the masses of the engine models Z9.6 and W18, respectively; and the corresponding results of these engine models are indicated by solid and dashed horizontal purple and blue lines. The mass range spanned by the horizontal purple line of model Z9.6 indicates the region of Crab-like behavior, where the Crab and SN 1987A engines are interpolated.

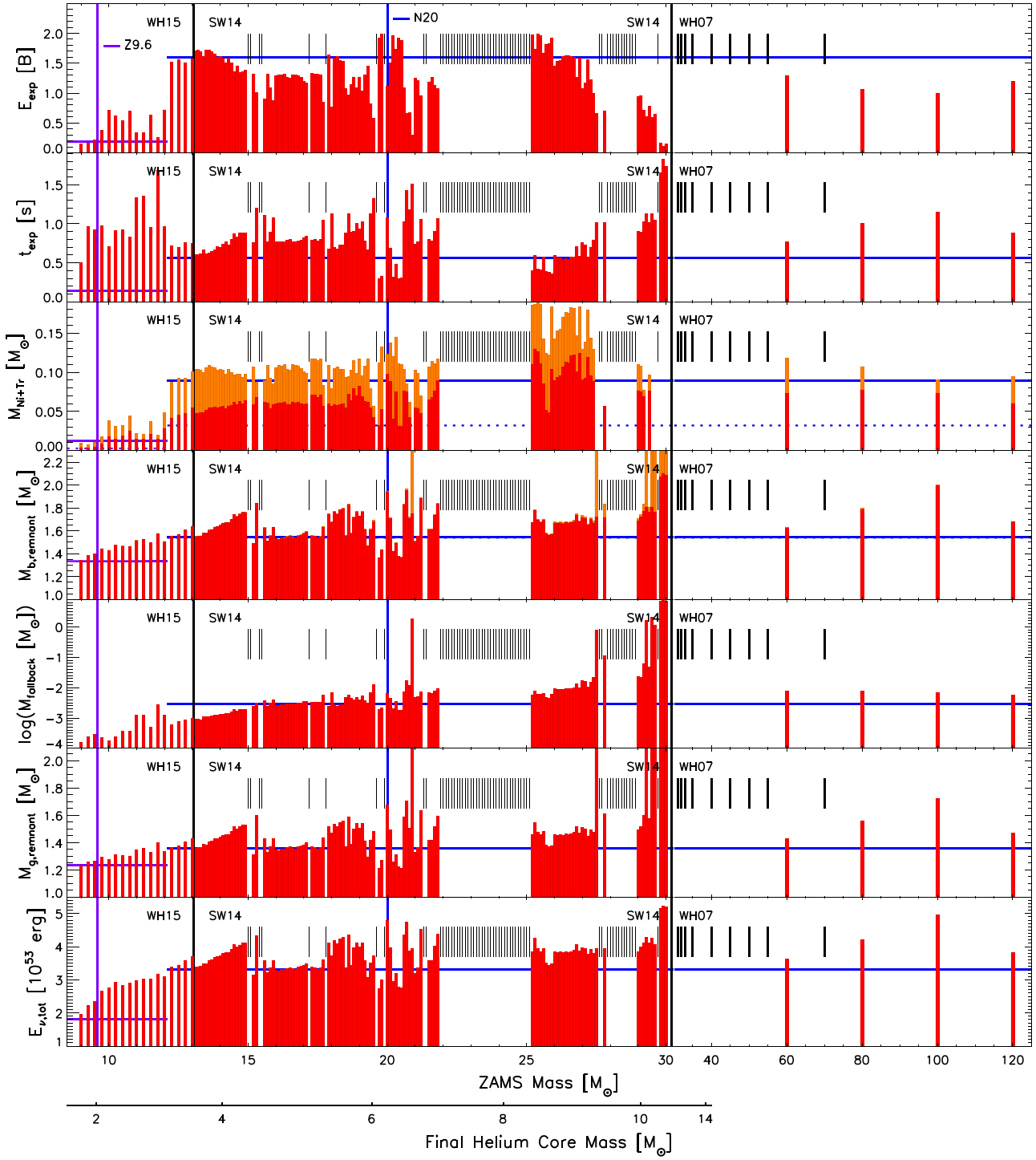

Figure 35. Same as Figure 34 but for simulations with the upgraded P-HOTB code and the combined Z9.6 and N20 neutrino engine. The plot can be directly compared with Figure 9 of Sukhbold et al. (2016). The exploding case at a ZAMS mass of 27.5 $M_\odot$ has a fallback mass of nearly 0.8 $M_\odot$, and the compact remnant is likely to survive as a neutron star, whereas in all other cases with massive fallback, the PNS accretes more than 1 $M_\odot$ of fallback matter and must be expected to collapse to a black hole.

evolved in one or the other direction could flip their behavior when applying the new version of P-HOTB. The slightly increased number of explosions with neutron star or fallback black hole formation in the new runs implies that the new code has a tendency to produce explosions a bit more readily. Such a trend can also be guessed from Table 9, where all calibration models except W18 blow up with slightly higher explosion energies in the new runs.

Figures 34 and 35 display the results of a number of characteristic quantities for our simulations of the solar-metallicity single-star progenitors of Sukhbold et al. (2016) with the upgraded version of P-HOTB. The two plots can be directly compared with Figures 8 and 9 in Sukhbold et al. (2016). The previous and new results look extremely similar; even the hills and valleys of the landscape pattern display great similarity, except for the slightly larger number of exploding

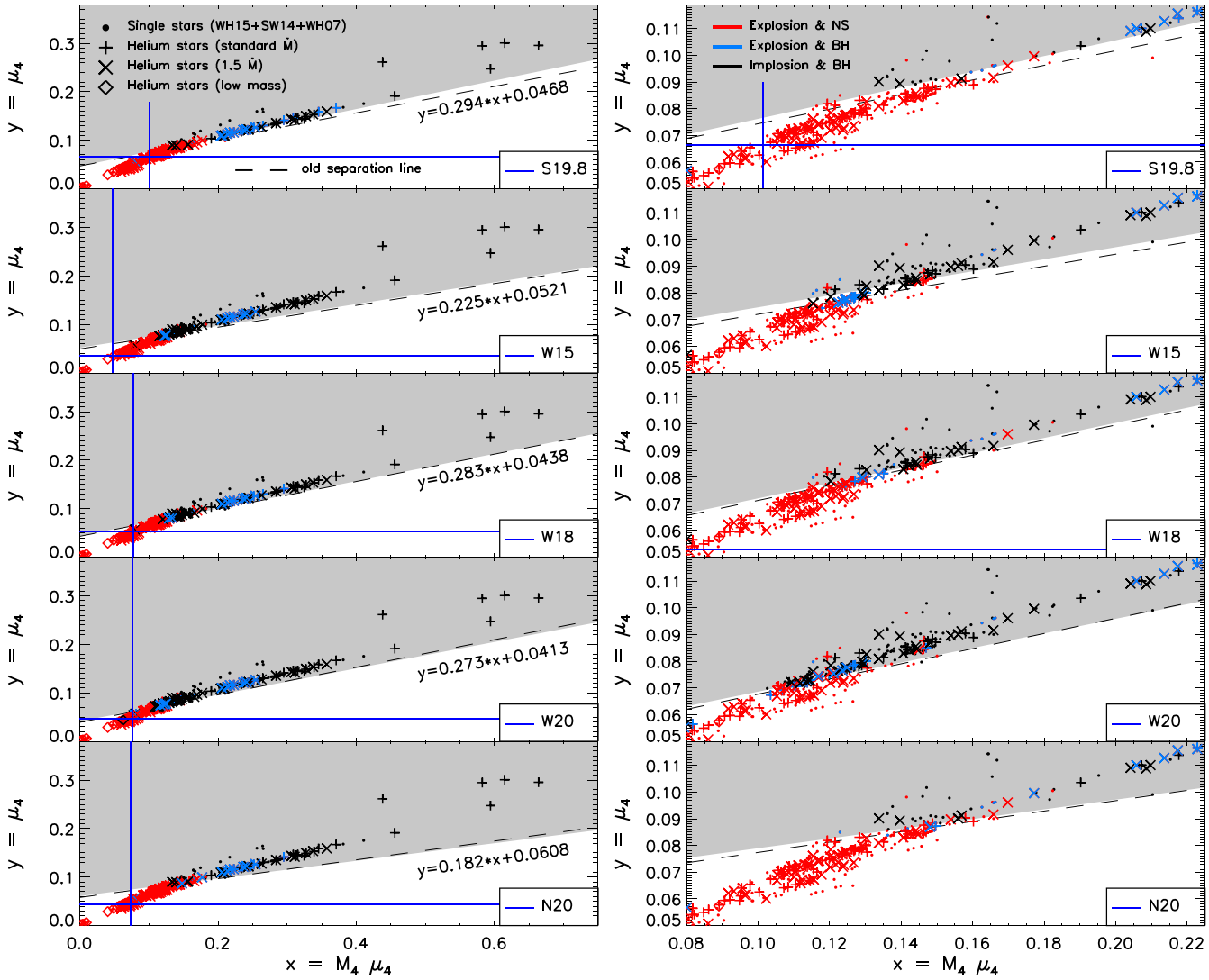

Figure 36. Separation curves between supernova explosions with neutron star formation (white region, red symbols) and black hole formation without supernova explosion (gray region, black symbols) or black hole formation in fallback supernovae (gray region, blue symbols) in the plane of parameters $x = M_4\mu_4$ and $y = \mu_4$. The different panels correspond to the different neutrino engines used for the 1D core-collapse modeling. The panels in the right column display zoom-ins to the region where the band of high model density crosses the separation line. Each simulated progenitor star corresponds to one symbol located at the (x, y) position computed from the stellar density profile. The different symbols indicate the different sets of progenitor stars, with dots marking the solar-metallicity single-star models investigated by Sukhbold et al. (2016) and all other symbols belonging to the helium stars studied in the present paper. All simulations were performed with the upgraded version of the P-HOTB code. The separation lines deduced by Ertl et al. (2016a) from simulations of a large set of single-star models with the old version of the P-HOTB code are displayed by dashed black lines. The crossing points of the blue solid horizontal and vertical lines correspond to the locations of the SN 1987A calibration models in the x–y plane.

cases in the new simulations already discussed in connection with Figure 33. There are two main differences in the new runs compared to the previous ones. First, a larger number of cases have massive fallback instead of failed explosions, narrowing some of the windows of direct black hole formation. Second, a dominant fraction of cases have slightly higher explosion energies (by about 0.1 B), marginally earlier explosions, and a somewhat lower ^{56}Ni mass and, at the same time, an increased tracer mass by roughly the same amount.

Our conclusion from this comparison is that we can safely compare the results of the helium star simulations in the present paper with the single-star models published by Sukhbold et al. (2016). Although the new version of P-HOTB improves the numerical performance and efficiency of the code, the physics results for the exact same choice of values of the neutrino-engine parameters have changed only in inessential details.

Appendix B
Update of the Two-parameter Criterion

Based on a large set of 1D explosion simulations for solar-metallicity, ultra-metal-poor, and zero-metallicity single-star progenitors, Ertl et al. (2016a) introduced a two-parameter criterion that separates cases of supernova explosions with neutron star formation from cases of black hole formation in a 2D plane that is spanned by the parameters

$$x = M_4\mu_4 \tag{18}$$

and

$$y = \mu_4. \tag{19}$$

Here

$$M_4 \equiv m(s = 4)/M_\odot \tag{20}$$

Table 10
Coefficients of Black Hole–Neutron Star Separation Curves for All Neutrino Engines from Ertl et al. (2016a; "Old") and Simulations with the Upgraded P-HOTB Code ("New")

Engine Model	k_1[a]	k_2[a]	M_4[b]	μ_4[b]	$M_4\mu_4$[b]
Z9.6 and S19.8[c] old	0.274	0.0470	1.529	0.0662	0.101
Z9.6 and S19.8[c] new	0.294	0.0468	1.529	0.0662	0.101
Z9.6 and W15[d] old	0.225	0.0495	1.318	0.0176	0.023
Z9.6 and W15[d] new	0.225	0.0521	1.318	0.0176	0.023
Z9.6 and W18 old	0.283	0.0430	1.472	0.0530	0.078
Z9.6 and W18 new	0.283	0.0438	1.472	0.0530	0.078
Z9.6 and W20 old	0.284	0.0393	1.616	0.0469	0.076
Z9.6 and W20 new	0.273	0.0413	1.616	0.0469	0.076
Z9.6 and N20 old	0.194	0.0580	1.679	0.0441	0.074
Z9.6 and N20 new	0.182	0.0608	1.679	0.0441	0.074

Notes.
[a] Best-fit values for the coefficients of the separation line (Equation (22)) when x and y are measured at a time when the central stellar density is 5×10^{10} g cm^{-3}.
[b] Measured for SN 1987A calibration models when the central stellar density is 5×10^{10} g cm^{-3}.
[c] Red supergiant progenitor from the model series of Woosley et al. (2002).
[d] The M_4 and μ_4 measured roughly at core bounce, because precollapse data are not available.

is the mass enclosed by the radius where the dimensionless entropy per nucleon has a value of $s = 4$, and

$$\mu_4 \equiv \left.\frac{\mathrm{d}m/M_\odot}{\mathrm{d}r/1000\ \mathrm{km}}\right|_{s=4} \tag{21}$$

is the derivative of the enclosed mass at this location. Both parameters are determined from the density profiles of the presupernova star and thus measure properties of the supernova progenitor, which means that each occupies one point on the x–y plane. Ertl et al. (2016a) found that the explosion behavior of the vast majority (over 97%) of their simulated models could be correctly predicted by the following criterion. For low values of y, i.e., below an inclined line

$$y_{\mathrm{sep}}(x) = k_1 \cdot x + k_2, \tag{22}$$

in the x–y plane, almost all stars explode and form neutron stars, whereas above this line, and therefore for high values of y, basically all stars collapse to black holes. Ertl et al. (2016a) explained this finding by demonstrating that the separation line can be interpreted as a correspondent of a generalized form of the critical luminosity condition for explosions introduced by Burrows & Goshy (1993). Ertl et al. (2016a) argued that $x = M_4\mu_4$ determines the neutrino luminosity, which has a strong accretion contribution, at the time the explosion sets in, and $y = \mu_4$ scales with the mass accretion rate $\dot{M}$ at this time. They supported this argument through very tight correlations between these quantities seen in their numerical models. Therefore, the separation line, $y_{\mathrm{sep}}(x)$, can be associated with the critical luminosity, $L_{\nu,\mathrm{crit}}(\dot{M})$, of Burrows & Goshy (1993). The line is inclined in the x–y plane with a positive slope k_1 because higher values of the mass accretion rate and thus y also lead to higher values of the neutrino luminosity and thus x, which leads to stronger neutrino heating and therefore an enlarged range of y-values where explosions are possible.

In Figure 36, we display the separation curves $y_{\mathrm{sep}}(x)$ for the five neutrino engines used in our study, applied to all solar-metallicity single-star models investigated by Sukhbold et al. (2016) and the two sets of helium star models considered in the present paper. All 1D simulations were conducted with the upgraded new version of P-HOTB. Figure 36 can be directly compared with Figure 8 of Ertl et al. (2016a). The white lower part of each panel is the region of supernova explosions with neutron star formation, and the gray shaded upper part of each panel highlights the region where black hole formation occurs. The "old" separation curves, indicated by a dashed black line in each panel of Figure 36, correspond to the gray–white boundaries in the panels of Figure 8 of Ertl et al. (2016a). In Table 10, the values for the slope coefficient k_1 and shift coefficient k_2 are listed for all of the employed neutrino engines, comparing the optimal values derived from the present simulations with the values provided by Ertl et al. (2016a) in their Table 2.

The best-fit values of k_1 and k_2 are nearly unchanged, and the old and new separation lines differ only very little. In the cases of the S19.8 and W15 engines the zoom-ins of the right panels in Figure 36 reveal the biggest differences, caused by a slight increase of k_1 for S19.8 and k_2 for W15. In the case of W18, the old and new values for both coefficients are effectively identical, and for W20 and N20, a minor change of one coefficient combined with the change of the other coefficient yields a hardly visible shift of the separation line in the region of interest.

The accuracy of predictions of explosion or nonexplosion of stellar progenitors with the revised separation lines is similarly good as with the old ones. For the S19.8 engine, the fraction of misclassifications is as low as 1.8%; for W15, it is 5% (but these cases lie de facto on the separation line). For W18, we find 3.3%; for W20, 4.8%; and for N20, 2.6%. Therefore, in total again, about 97% of all cases are correctly predicted in their explosion behavior by our $y_{\mathrm{sep}}(x)$ criterion.

It is worth noting that both the black hole formation cases without supernova explosions and the black hole formation cases due to massive fallback (defined as in the caption of Figure 33), which occur in fallback supernovae and are marked by blue symbols in Figure 36, are chosen to lie above the separation curves, i.e., in the black hole region. These cases barely explode, and their behavior is closer to failed explosions than to successful supernovae with neutron star formation.

ORCID iDs

T. Ertl https://orcid.org/0000-0002-5711-7969
S. E. Woosley https://orcid.org/0000-0002-3352-7437
Tuguldur Sukhbold https://orcid.org/0000-0002-1728-1561
H.-T. Janka https://orcid.org/0000-0002-0831-3330

References

Abbott, B. P., Abbott, R., Abbott, T. D., et al. 2018, PhRvL, 121, 161101
Amarsi, A. M., Nissen, P. E., & Skúladóttir, Á. 2019, A&A, 630, 104
Anderson, J. P. 2019, A&A, 628, A7
Antoniadis, J., Freire, P. C. C., Wex, N., et al. 2013, Sci, 340, 448
Antoniadis, J., Tauris, T. M., Ozel, F., et al. 2016, arXiv:1605.01665
Arcones, A., Janka, H.-T., & Scheck, L. 2007, A&A, 467, 1227
Barbuy, B., Chiappini, C., & Gerhard, O. 2018, ARA&A, 56, 223
Bauswein, A., Just, O., Janka, H.-T., et al. 2017, ApJL, 850, L34
Belczynski, K., Wiktorowicz, G., Fryer, C. L., et al. 2012, ApJ, 757, 91
Beniamini, P., Hotokezaka, K., van der Horst, A., et al. 2019, MNRAS, 1336, 1426

Branch, D., & Wheeler, J. C. 2017, Supernova Explosions (Berlin: Springer)
Bruenn, S. W., Lentz, E. J., Hix, W. R., et al. 2016, ApJ, 818, 123
Burrows, A., & Goshy, J. 1993, ApJL, 416, L75
Chatzopoulos, E., Wheeler, J. C., Vinko, J., et al. 2013, ApJ, 773, 76
Chen, K.-J., Woosley, S. E., & Sukhbold, T. 2016, ApJ, 832, 73
De, K., Kasliwal, M. M., Ofek, E. O., et al. 2018, Sci, 362, 201
De Marco, O., & Izzard, R. G. 2017, PASA, 34, e001
Dessart, L., Hillier, D. J., Li, C., & Woosley, S. 2012, MNRAS, 424, 2139
Dessart, L., Hillier, D. J., Woosley, S., et al. 2015, MNRAS, 453, 2189
Drout, M. R., Milisavljevic, D., Parrent, J., et al. 2016, ApJ, 821, 57
Drout, M. R., Soderberg, A. M., Gal-Yam, A., et al. 2011, ApJ, 741, 97
Ebinger, K., Curtis, S., Fröhlich, C., et al. 2019, ApJ, 870, 1
Ensman, L. M., & Woosley, S. E. 1988, ApJ, 333, 754
Ertl, T., Janka, H.-T., Woosley, S. E., et al. 2016a, ApJ, 818, 124
Ertl, T., Ugliano, M., Janka, H.-T., et al. 2016b, ApJ, 821, 69
Farr, W. M., Sravan, N., Cantrell, A., et al. 2011, ApJ, 741, 103
Fryer, C. L. 1999, ApJ, 522, 413
Fryer, C. L., Belczynski, K., Wiktorowicz, G., et al. 2012, ApJ, 749, 91
Fryer, C. L., & Kalogera, V. 2001, ApJ, 554, 548
Fryxell, B., Müller, E., & Arnett, D. 1989, in Proc. 5th Workshop on Nuclear Astrophysics, ed. W. Hillebrandt & E. Müller, 100
Fryxell, B., Müller, E., & Arnett, D. 1991, ApJ, 367, 619
Fulbright, J. P., McWilliam, A., & Rich, R. M. 2007, ApJ, 661, 1152
Gessner, A., & Janka, H.-T. 2018, ApJ, 865, 61
Griffith, E., Johnson, J. A., & Weinberg, D. H. 2019, ApJ, 886, 84
Hammer, N. J., Janka, H.-T., & Müller, E. 2010, ApJ, 714, 1371
Heger, A., Woosley, S. E., & Spruit, H. C. 2005, ApJ, 626, 350
Hillier, D. J., & Dessart, L. 2012, MNRAS, 424, 252
Janka, H.-T 2017, in Handbook of Supernovae, ed. A. Alsabti & P. Murdin (Cham: Springer International), 1095
Janka, H.-T., & Müller, E. 1996, A&A, 306, 167
Jerkstrand, A., Ertl, T., Janka, H.-T., et al. 2018, MNRAS, 475, 277
Jerkstrand, A., Smartt, S. J., Inserra, C., et al. 2017, ApJ, 835, 13
Kasen, D., & Bildsten, L. 2010, ApJ, 717, 245
Kifonidis, K., Plewa, T., Janka, H.-T., & Müller, E. 2003, A&A, 408, 621
Kleiser, I. K. W., Kasen, D., & Duffell, P. C. 2018, MNRAS, 475, 3152
Kreidberg, L., Bailyn, C. D., Farr, W. M., & Kalogera, V. 2012, ApJ, 757, 36
Langer, N. 2012, ARA&A, 50, 107
Lattimer, J. M. 2012, ARNPS, 62, 485
Lattimer, J. M., & Prakash, M. 2001, ApJ, 550, 426
Lattimer, J. M., & Swesty, F. D. 1991, NuPhA, 535, 331
Liebendörfer, M. 2005, ApJ, 633, 1042
Limongi, M., & Chieffi, A. 2006, ApJL, 647, L483
Lodders, K. 2003, ApJ, 591, 1220
Lyman, J. D., Bersier, D., James, P. A., et al. 2016, MNRAS, 457, 328
Marek, A., & Janka, H.-T. 2009, ApJ, 694, 664
Margalit, B., & Metzger, B. D. 2017, ApJL, 850, L19
Martínez-Pinedo, G., Fischer, T., Lohs, A., et al. 2012, PhRvL, 109, 251104
Maund, J. R. 2018, MNRAS, 476, 2629
Maurer, J. I., Mazzali, P. A., Deng, J., et al. 2010, MNRAS, 402, 161
Menon, A., & Heger, A. 2017, MNRAS, 469, 4649
Mirizzi, A., Tamborra, I., Janka, H.-T., et al. 2016, NCimR, 39, 1
Müller, B. 2015, MNRAS, 453, 287
Müller, B., Gay, D. W., Heger, A., et al. 2018, MNRAS, 479, 3675
Müller, B., Heger, A., Liptai, D., et al. 2016, MNRAS, 460, 742
Müller, B., Melson, T., Heger, A., et al. 2017, MNRAS, 472, 491
Müller, E. 1986, A&A, 162, 103
Müller, E., Fryxell, B., & Arnett, D. 1991, A&A, 251, 505
Nicholl, M., Guillochon, J., & Berger, E. 2017, ApJ, 850, 55
O'Connor, E., & Ott, C. D. 2011, ApJ, 730, 70
Özel, F., & Freire, P. 2016, ARA&A, 54, 401
Özel, F., Psaltis, D., Narayan, R., & McClintock, J. E. 2010, ApJ, 725, 1918
Pastorello, A., Mattila, S., Zampieri, L., et al. 2008, MNRAS, 389, 113
Pastorello, A., Wang, X.-F., Ciabattari, F., et al. 2016, MNRAS, 456, 853
Peebles, P. J. E. 1993, Principles of Physical Cosmology (Princeton, NJ: Princeton Univ. Press), 131
Pejcha, O., & Thompson, T. A. 2015, ApJ, 801, 90
Podsiadlowski, P. 1992, PASP, 104, 717
Prentice, S. J., Ashall, C., James, P. A., et al. 2019, MNRAS, 485, 1559
Prentice, S. J., Mazzali, P. A., Pian, E., et al. 2016, MNRAS, 458, 2973
Pruet, J., Hoffman, R. D., Woosley, S. E., et al. 2006, ApJ, 644, 1028
Raithel, C. A., Sukhbold, T., & Özel, F. 2018, ApJ, 856, 35
Rezzolla, L., Most, E. R., & Weih, L. R. 2018, ApJL, 852, L25
Roberts, L. F. 2012, ApJ, 755, 126
Salpeter, E. E. 1955, ApJ, 121, 161
Sana, H., de Mink, S. E., de Koter, A., et al. 2012, Sci, 337, 444
Sana, H., & Evans, C. J. 2011, IAU Symp, Active OB Stars: Structure, Evolution, Mass Loss, and Critical Limits 272 (Cambridge: Cambridge Univ. Press), 474
Scheck, L., Kifonidis, K., Janka, H.-T., & Müller, E. 2006, A&A, 457, 963
Schneider, A. S., Roberts, L. F., Ott, C. D., et al. 2019, arXiv:1906.02009
Schwab, J., Podsiadlowski, P., & Rappaport, S. 2010, ApJ, 719, 722
Shiode, J. H., & Quataert, E. 2014, ApJ, 780, 96
Smartt, S. J. 2009, ARA&A, 47, 63
Smartt, S. J. 2015, PASA, 32, e016
Steiner, A. W., Hempel, M., & Fischer, T. 2013, ApJ, 774, 17
Sukhbold, T., & Adams, S. 2020, MNRAS, 492, 2578
Sukhbold, T., Ertl, T., Woosley, S. E., et al. 2016, ApJ, 821, 38
Sukhbold, T., & Woosley, S. E. 2014, ApJ, 783, 10
Sukhbold, T., Woosley, S. E., & Heger, A. 2018, ApJ, 860, 93
Suntzeff, N. B., Phillips, M. M., Elias, J. H., Walker, A. R., & Depoy, D. L. 1992, ApJL, 384, L33
Taddia, F., Sollerman, J., Fremling, C., et al. 2019, A&A, 621, A71
Ugliano, M., Janka, H.-T., Marek, A., & Arcones, A. 2012, ApJ, 757, 69
Utrobin, V. P., Wongwathanarat, A., Janka, H.-T., et al. 2019, A&A, 624, A116
Utrobin, V. P., Wongwathanarat, A., Janka, H.-T., & Müller, E. 2015, A&A, 581, A40
Valentim, R., Rangel, E., & Horvath, J. E. 2011, MNRAS, 414, 1427
Villar, V. A., Nicholl, M., & Berger, E. 2018, ApJ, 869, 166
Vreeswijk, P. M., Leloudas, G., Gal-Yam, A., et al. 2017, ApJ, 835, 58
Weaver, T. A., Zimmerman, G. B., & Woosley, S. E. 1978, ApJ, 225, 1021
Weinberg, D. H., Holtzman, J. A., Hasselquist, S., et al. 2019, ApJ, 874, 102
Wellstein, S., & Langer, N. 1999, A&A, 350, 148
Wongwathanarat, A., Hammer, N. J., & Müller, E. 2010a, A&A, 514, A48
Wongwathanarat, A., Janka, H.-T., & Müller, E. 2010b, ApJL, 725, L106
Wongwathanarat, A., Janka, H.-T., & Müller, E. 2013, A&A, 552, A126
Wongwathanarat, A., Janka, H.-T., Müller, E., Pllumbi, E., & Wanajo, S. 2017, ApJ, 842, 13
Wongwathanarat, A., Müller, E., & Janka, H.-T. 2015, A&A, 577, A48
Woosley, S. E. 2010, ApJL, 719, L204
Woosley, S. E. 2017, ApJ, 836, 244
Woosley, S. E. 2019, ApJ, 878, 49
Woosley, S. E., & Heger, A. 2007, PhR, 442, 269
Woosley, S. E., & Heger, A. 2015, ApJ, 810, 34
Woosley, S. E., Heger, A., & Weaver, T. A. 2002, RvMP, 74, 1015
Woosley, S. E., Pinto, P. A., & Ensman, L. 1988, ApJ, 324, 466
Yoon, S.-C. 2017, MNRAS, 470, 3970
Yoon, S.-C., Woosley, S. E., & Langer, N. 2010, ApJ, 725, 940